Advanced Condition Monitoring for Organic Rankine Cycle Systems

Ozichukwu Precious Osakwe

January 2018

Delft University of Technology

TRIOGEN

Advanced Condition Monitoring for Organic Rankine Cycle Systems

Thesis submitted in partial fulfilment of the regulations for the degree of Master of Science
At the Delft University of Technology,
Faculty of Aerospace Engineering,
Flight Performance and Propulsion,
Propulsion and Power group.

Student:
Ozichukwu Precious Osakwe (4480341)

Graduation Committee:
Prof. Dr. Ir. P. Colonna di Paliano (TUDelft)
Dr. Ir. W.P.J. Visser (TUDelft)
Dr. Ir. H.G. Visser (TUDelft)
Ir. Q. Eppinga (Triogen)

Examination Date:

29th January 2018

TU Delft
Delft
University of
Technology

TRIOGEN

Acknowledgement

My interest in condition monitoring was aroused when I took the course on Gas Turbine Simulation and application of which my academic supervisor, Dr. Ir. Visser, was the responsible instructor. I found the course very interesting and thus decided to pursue a thesis in this field.

First, I would like to thank my academic supervisor for offering me the opportunity to carry out this thesis. In addition, I would like to express my appreciation for the discussions, many suggestions and the unreserved patience to guide me during the course of completing this work.

Furthermore, I would like to express my sincere gratitude to my daily supervisor, Quirijn Eppinga, for his guidance, constructive feedback and thoroughness every step of the way. Also, many thanks to Erik Jan Beld and Bas van Laar who put up with all my questions. In addition, my appreciation goes to everyone at Triogen who helped in one way or the other: Prof. van Buijtenen for his invaluable feedback and time, Gerwin Schimmel who assisted immensely in the basic understanding required for this work, Roy Curre, Eric Klaasen for the discussions about everything and anything, Wim Reuling, Wouter Bisschop, Henning von Barsewisch, Thijs aan de Stegge, Nigel Sloot and Kees Brouwer.

Finally, I would like to thank God, my family and friends for being there every step of the way. Without the support of my family all through the years, I would not be where I am today. Also, many thanks to Dos and Julien for weathering the storm with me and Alexandra for the immense academic and emotional support.

Ozichukwu Precious Osakwe

Enschede, January 2018

This work is dedicated to my father;

I can only hope to one day become half the man you are.

Summary

Global warming is a result of certain human activities for which measures, such as transitioning to cleaner sources of energy and improving the efficiency of power generators, are crucial in combating it. An Organic Rankine Cycle (ORC) is a power cycle which when coupled to heat emitting power generators allows for waste heat recovery; thus increasing the engine overall efficiency and reducing atmospheric pollution. Additionally, implementing engine life cycle management is another way to improve the overall efficiency of power systems by ensuring that unnecessary downtime is avoided. This research is centred on developing an effective condition monitoring tool for ORC systems. The result of this research includes a complete adaptation of a condition monitoring tool, GTPtracker, originally developed for gas turbines to ORC systems.

The condition monitoring tool that has been developed as a result of this research comprises a true model derived from data obtained from sensors placed in an active ORC and an ideal model which is a zero dimensional surrogate model. The true model describes the real state of the ORC by using the sensor data whereas the surrogate model utilizes key thermophysical and system properties obtained from the sensor data and certain component design specifications to describe the ideal state of that ORC system.

According to the state postulate, the knowledge of two intensive properties is sufficient to specify the complete state of a compressible system. Thus, in this research, mathematical equations were specifically derived, as a function of two intensive properties, to compute the thermophysical properties (e.g. enthalpy, density) that define the health indices of each component. Temperatures and pressures at the inlet and outlet of each component are utilised in the mathematical equations to estimate thermophysical properties and subsequently true health indices for each component. However, the surrogate model utilizes the evaporating and condensing temperatures and pressures and the rotational speeds obtained from the sensor data as initial inputs and then builds up an ideal version of the ORC with the mathematical relations and other standard thermodynamic relations. A comparison of the ideal version with the true state of the ORC reveals the health status of each component in form of an index deviation chart and a consideration of the deviation pattern and magnitude gives the necessary information on the health status of the ORC.

The main contribution of this research lies in developing a condition monitoring tool that is capable of providing accurate diagnostic results in the shortest possible time. At the onset of the research, the limitations were largely due to the unavailability of certain component maps; thus, it was necessary to scale and adapt performance maps of dynamically similar components from literature. Furthermore, standard thermodynamic property relations are not available for the working fluid and it was not feasible to establish a connection between the GTPtracker software and a thermodynamic property library; hence, unique thermodynamic relations for the model has to be developed. The method to develop the thermodynamic relations is novel and a very important element of this research because of the condition monitoring technique adopted for this research. Gas Path Analysis (GPA) was adopted for this research because of its wider scope; however, it relies on fluid thermodynamic behaviour to determine the health status of a system. Prior to this research, implementing GPA for any process that involves fluid phase change would have required the inclusion of a third party thermodynamic property library software but the development of this novel method to characterise the thermodynamic properties of fluids that undergo phase change completely eliminates this need and is thus a welcome development. Moreover, coupling several subsystems would have a negative effect on the speed of the overall process; thus, the adoption of an equation based approach greatly improves the computational speed of the condition monitoring tool.

The condition monitoring tool was validated by applying it to two Triogen ORC systems currently in operation for a duration of one and six weeks. In both cases, the ORC was running in normal mode and all the faults present were successfully detected and isolated. Furthermore, component level fault detection was demonstrated in both cases and the root cause of the fault inferred from fault patterns. In addition, unlike known adaptive modelling techniques where the conservation equations for the entire system would need to be solved iteratively to tune the surrogate model, necessary adjustments were made easily and directly to the thermophysical relations for the components of interest without any effect on other components.

In future, more advanced condition monitoring techniques for ORC systems will be developed. However, knowledge of the working fluid thermophysical properties will always be a requirement and the fastest methods to derive it will be favoured especially for online condition monitoring; thus, the equation based modelling approach developed in this research will remain relevant.

Table of Contents

List of Figures

List of Tables

Nomenclature

Acronyms and abbreviations

LCM	Life Cycle Management
ORC	Organic Rankine Cycle
GTPtracker	Gas Turbine Performance Tracker
GPA	Gas Path Analysis
FCM	Fault Coefficient Matrix
ICM	Influence Coefficient Matrix
AM	Adaptive Modelling
MF	Modification Factor
ANN	Artificial Neural Network
PNN	Probabilistic Neural Network
SOM	Self-Organizing Map
LVQ	Learning Vector Quantization
CPN	Counter Propagation Network
ART	Adaptive Resonance Theory
RAN	Resource Allocation Network
RCC	Recurrent Cascade Correlation
CFD	Computational Fluid Dynamics
SSE	Sum of Squares due to Errors
RMSE	Root Mean Square Error
SSR	Sum of Squares of the Regression
SST	Total Sum of Squares
MSE	Mean Squared Errors
SV	Storage Vessel
PFP	Pre-feed Pump

PR	Pressure Ratio
Rcs	Recuperator cold side
Rhs	Recuperator hot side
PtG	Power to grid

Variables

δ	deviation
$\overline{m}$	Measured parameter vector
F	Fault matrix
$\overline{h}$	Health parameter vector
∂	Partial derivative
J	Objective function
e	Error
a, b, c, d	Polynomial coefficients
P	Pressure
T	Temperature
h	Enthalpy
s	Entropy
ρ	Density
$\dot{P}$	Power
N	Rotational speed
Ψ	Pump head coefficient
g	Acceleration due to gravity
ε	Heat exchanger effectiveness
∇	Decrement
Δ	Increment
D, d	Diameter

A	Area
$\dot{Q}$	Heat available
η	Efficiency
f	Function
γ	Specific heat ratio
$\dot{m}$	Mass flow rate
c_p	Specific heat capacity
$\dot{W}$	Work done
$a, b, c, d, e, f, k, w, \omega$	Polynomial coefficients

Subscripts and superscripts

c, i, j, k, l, m, n, o	Number of parameters in a set
$1,3,5,6,7,8,9,10$	Control points
s	Isentropic parameter
in, i	Inlet
out, o	Outlet
max	Maximum
min	Minimum
mp	Main pump
pfp	Pre-feed pump
aux	Auxiliaries
t	Turbine
c	Condenser

1 Introduction

Engine condition monitoring is an area of life cycle management (LCM) that has been explored over the years. The ability to accurately detect faults and schedule maintenance, based on engine state, is a very attractive prospect because of the possibility to reduce downtime, reduce operating costs and improve engine lifespan. An engine type that has been around for quite some time now is the gas turbine engine. The diversity in its applications has made it a very attractive option for applications requiring a very high power-to-weight ratio. As a result of these favourable characteristics, a large majority of the investigations and advancements have been focused on gas turbines.

As the world has begun to shift to cleaner sources of energy to reduce CO_2 emissions and prevent climate change, more effort has been put into improving the efficiency of power generators. A method of improving the overall efficiency of an engine is by converting its waste heat into useful energy and the Organic Rankine Cycle (ORC) is a very effective cycle that can be used to achieve this aim. ORC technology is relatively young and as a result, little has been done with regards to improvements in its life cycle management. The available methods for ORC condition monitoring that have been postulated in the past are component specific and thus do not consider the system as a whole. To fill this gap, a proposal, which necessitates the preliminary research contained in this document, is made. This proposal seeks to develop a comprehensive method for ORC condition monitoring, with condition assessment on the component level.

To improve the life cycle of their ORC system, Triogen (an ORC manufacturer in Goor, Netherlands) is looking to fit all of its ORC systems in operation with GTPtracker (Gas Turbine Performance tracker, developed by B&B-AGEMA in Aachen, Germany), an on-line condition monitoring tool. The GTPtracker software is flexible, with respect to its applications, and capable of providing accurate real-time performance, vibration and oil/lubrication system monitoring of energy systems, which can aid in the detection, isolation and prediction of machine component faults. However, the GTPtracker would have to be adapted for ORC systems. Rulesets, condition parameters, correlation analysis and trending algorithms would need to be developed.

First, a description of the system under consideration is presented in section 1.1, and then the on-line monitoring tool to be used is briefly described in section 1.2.

1.1 The Triogen ORC system

The Triogen ORC is a dual pressure system and comprises eight main components: a storage vessel, pre-feed pump, main pump, recuperator, evaporator, turbine, generator and condenser. Figure 1-1 shows a schematic of the Triogen ORC system, based on which the cycle is described. Along the cycle, all equipment and processes from the main pump to the turbine inlet (control points 3-5 in Figure 1-1) are at a higher pressure while all equipment and processes in the other parts of the system are at a lower pressure [1].

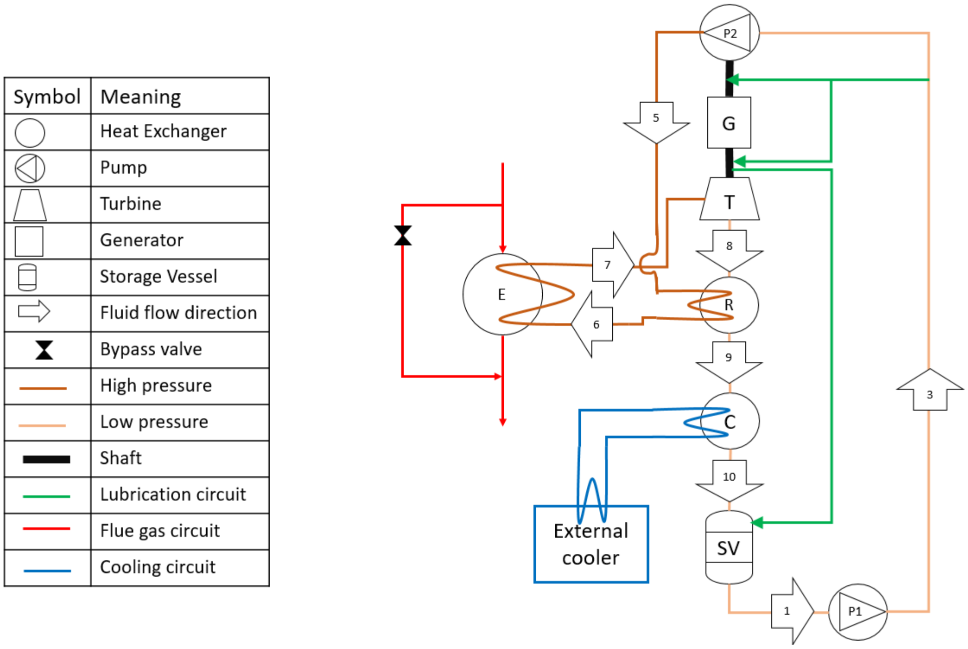

Figure 1-1: Schematic representation of the Triogen ORC system [1].

The storage vessel serves as the start and end point for one cycle and the heat input into the system (flue gas) us supplied by the customer. The pre-feed pump provides suction head, moving the working fluid from the storage vessel up to the main pump (control point 1-2) where the pressure of the working fluid is raised to the maximum cycle pressure, and the fluid needed for cooling the generator and lubricating the bearings. Subsequently, the working fluid is pre-heated on passing through the recuperator (control point 3-4), using the heat from the fluid exiting the turbine. The working fluid then flows through the evaporator (control point 4-5) where heat from the flue gas causes it to superheat. The superheated working fluid is at a high pressure and temperature at this stage and is used to drive the turbine (control point 5-6). In the turbine, the pressure and temperature of the working fluid drops. Upon exiting the turbine, the working fluid passes over the recuperator (control point 6-7) where some of its heat is given off. The working fluid is then passed through the condenser (control point 7-8) where it is returned to its saturated state and then channelled to the storage vessel for the next cycle. The main pump, the generator and the turbine are mounted on a single shaft; thus, the main pump is mechanically driven while the pre-feed pump is operated with power extracted from the gross power output of the generator.

The Triogen ORC system has two control systems. The first control system is programmed to ensure that the working fluid is at the set temperature before entering the turbine. As an example, when the heat available from the flue gas is low, the turbine inlet temperature and pressure are low. To ensure the working fluid is at this set temperature, a frequency converter, which links the generator to the grid, causes the shaft speed to decrease and thus the pressure decreases. The consequence of this adjustment is a reduction in the mass flow rate of the working fluid, which then causes the temperature to revert to the set temperature. The second control system is coupled to the condenser. This control system ensures that the condenser outlet temperature remains at the design value. If the condenser exit temperature increases or decreases, the control system causes the external air cooler to increase or decrease the airflow thus adjusting the temperature to the design value.

Like any thermodynamic system, the complex component interrelationships of the Triogen ORC system makes it difficult to isolate faults without the use of advanced condition monitoring techniques. For example, if the amount of heat transfer (from the flue gas to the working fluid) in the evaporator is less than the design value, the temperature and the pressure at the turbine inlet will reduce. This reduction in temperature and pressure also affects the thermophysical properties across the recuperator, the external cooler power requirement, the gross power output and the overall efficiency of the system. Observation of the system externally would reveal only a reduction in power output and this information is insufficient to isolate the root cause; thus the need for condition monitoring. This need, especially for industrial machinery, cannot be overemphasized. Asides the advantage of reducing maintenance costs and improving the life cycle of a machine, condition monitoring can improve safety on-site. When faults are detected and isolated in time, the severity can be determined and a safe decision can be made concerning its operation.

1.2 GTPtracker

In the performance monitoring module of the GTPtracker, system gas path thermophysical properties (e.g. pressure, temperature) are monitored, using sensors placed at strategic locations in the system cycle. Subsequently, these sensors are employed in estimating component parameter trends (e.g. efficiency, power coefficient) so as to determine the health status of the system [2].

To adopt the GTPtracker software for the condition monitoring of any power cycle, a baseline first has to be defined using an ideal model of that power cycle. Selection of gas path thermophysical (or dependent) parameters, derivation and correction of component (or independent) parameters and definition of the tolerance limits for these parameters are then specified in the GTPtracker software. In order to ensure accurate results whilst using this powerful tool, it is imperative that the system is properly and thoroughly defined. Baseline definition, selection of dependent and independent parameters, correction of independent parameters, and definition of rulesets must be done methodically [2]. When the cycle being monitored is in operation, a deviation in the trend of a dependent parameter (or a combination of dependent parameters) will result in a deviation in the trend of an independent parameter (or a combination of independent parameters). This will aid in fault detection and isolation and also assist in the proposal of an ideal maintenance schedule. The workflow process of the GTPtracker software is depicted in Figure 1-2.

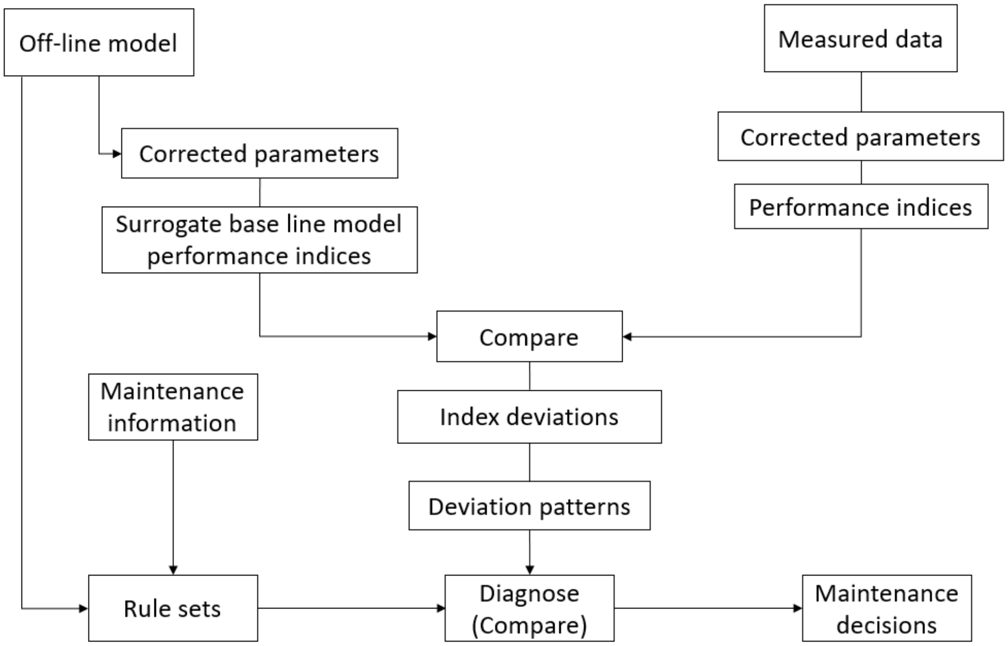

Figure 1-2: Work flow process of the GTPtracker software [2].

This software requires definition of the component condition parameters, the thresholds for these parameters, rulesets and predefined maintenance actions if available. Engine prognosis is also possible using this tool. Based on parameter trends, this tool can predict, to an extent, the performance characteristics of the engine under consideration and this characteristics is very valuable especially in on-line condition monitoring applications [2].

For this research, the goal is to configure this tool for the Triogen ORC system. However, the workflow process would have to be adapted to suit the present need since the tool was originally developed for gas turbines.

1.3 Research scope

The purpose of this research is to develop and demonstrate the GTPtracker software, configured for the Triogen ORC system, to provide an effective condition monitoring system. Thus the objective of this research is:

"To create a robust condition monitoring tool for the Triogen ORC system which is capable of detecting, isolating and predicting component faults, based on fluid thermophysical property trends, and capable of guiding and assisting the user in proposing short and long term recommendations and/or solutions to mitigate these faults."

In order to achieve the research objective, certain requirements must be satisfied. First, a condition monitoring method must be selected, component condition parameters must be derived and corrected for fault identification, rulesets need to be defined and grouped for fault qualification, and correlation analysis and trending algorithms must be developed for fault prognostics.

The condition monitoring technique to be used in this research must be able to provide sufficient diagnostics results. In chapter 2, the various condition monitoring methods that have been developed and implemented over the years will be explored and the most suitable method will be selected. Also, to ensure a robust diagnostic tool, each component must be represented by at least two independent parameters [3]. Component health parameters must be defined appropriately to ensure that they are independent of the engine operating condition. Additionally, the rulesets to be developed must be defined and grouped such that fault diagnosis and sensor error identification are effective. Rulesets are a combination of component parameters, which upon violation (deviation in component condition parameters beyond set tolerance limits) help in narrowing down fault root cause. Each ruleset comprises component condition parameters with their set tolerance limits and if any component health parameter (or a combination of component condition parameter limits) exceeds its set limit, the ruleset group(s) violated gives the information needed to identify the faulty component(s).

Finally, the obvious advantage of running diagnostics is the added effectiveness to maintenance scheduling. After a fault is detected and isolated, relevant maintenance action(s) has to be performed to ensure that the fault is properly addressed. To ensure that necessary maintenance actions are carried out, it is imperative that the root cause is specific enough to allow the maintenance engineer focus on the exact component that needs to be addressed. In addition, in this research, the condition monitoring tool must be validated to avoid false positives because it is important that the limits of the condition monitoring tool are known to avoid diagnostic errors.

To successfully meet the set objective, and ensure that the standard requirements for a condition monitoring tool are satisfied, certain questions can be formulated alongside sub-questions, and the answers to the sub-questions provide answers to the questions, which then provide the necessary knowledge to satisfy the research objective. Thus, the formulated research questions and sub-questions are:

1. Which condition monitoring technique should be selected for the Triogen ORC system?
    a. Based on literature findings, is any of the condition monitoring methods applied to gas turbines suitable for implementation?
    b. Are modifications necessary for the condition monitoring technique selected from literature?
        i. What part of the condition monitoring technique needs modification?
        ii. How should the proposed modifications be implemented such that robustness is not compromised?

   c. If there is a need to develop a new condition monitoring technique, unique to the system under consideration, what are the steps to needed to achieve this?

2. How should component health parameters be derived and corrected for ORC condition monitoring?
   a. What technique should be employed in deriving component condition parameters?
   b. Which of the system thermophysical parameters are critical?
   c. How can the key thermophysical parameters be used for component performance parameter correction?
   d. How should component parameters be selected for diagnosis to ensure linear independence?
3. How can engine component faults be identified and isolated for the Triogen ORC system?
   a. How should the rulesets be defined?
   b. How should the tolerance limits for each component health parameter be determined?
   c. How can sensor error be differentiated from actual engine fault?
4. How can the condition monitoring tool be checked for robustness?
   a. Can validation methods applied to gas turbines, as in literature, be adopted?
   b. Are there any other means that can be applied in validating the model?

1.4 Thesis structure

The aim of this section is to provide insight into the content of this report and give a summary of what succeeding chapters contain. For this research, the methodology comprises four stages, which are presented in the coming chapters. The first stage is the literature study (chapter 2) where existing condition monitoring techniques are explored and the most suitable to the current research is selected. Next is the surrogate modelling stage (chapter 3) where the condition monitoring tool is developed. Subsequently, the component health evaluation stage (chapter 0) where the effects of component health deterioration are analysed follows and finally the validation stage (chapter 5) where the model is tested with real data.

2 Literature review

Existing condition monitoring techniques for gas turbines can be grouped into four categories: mechanical integrity analysis, wear debris analysis, vibration analysis and performance analysis [4]. Mechanical integrity analysis involves physical inspection of engine components while wear debris analysis involves the assessment of oil samples from the engine. These condition monitoring techniques, amongst other limitations, require the specification of a maintenance schedule based on manufacturer specifications and hence they contribute to engine downtime. Vibration analysis, whilst possible to monitor remotely, is only applicable to rotating machinery and thus would need to be supplemented by other monitoring techniques upon application. Performance analysis, unlike the other monitoring techniques, offers a wider scope. A well-developed performance analysis technique does not necessitate physical inspection nor require supplementation.

Performance analysis, also referred to as Gas Path Analysis (GPA), is a method of engine condition monitoring that relies on the gas properties, at different locations within an engine, as a basis in deducing the health status of an engine in operation. The idea behind the concept is that there exist a relationship between physical engine faults, deteriorated engine components and deviations in engine thermophysical parameters. The occurrence of physical engine faults, such as corrosion and fouling, on engine components will affect component performance; the resulting effect will then be obvious from deviations in the thermophysical parameters that define the engine cycle. The GPA concept is shown in Figure 2-1.

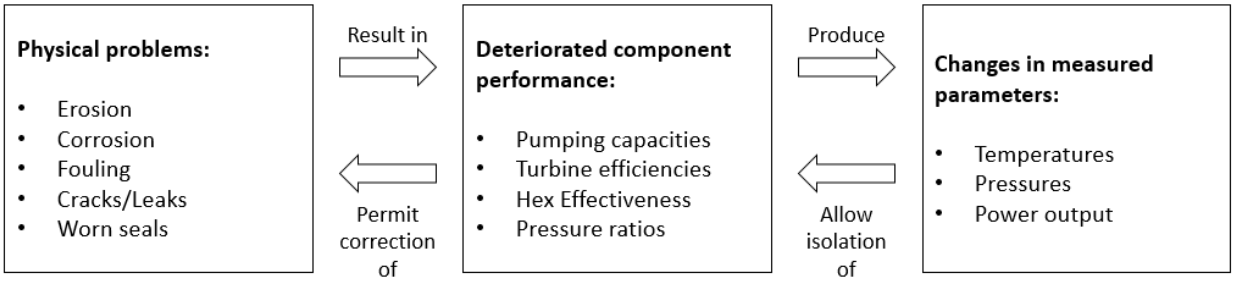

Figure 2-1: The GPA concept [5].

Sections 2.1 to 2.5 give an overview of the various GPA methods that have been developed and used for engine condition monitoring over the years.

In applying the GPA techniques to the ORC system, one would first need to determine and correct the component condition parameters. Dimensional analysis of turbomachines as described by Dixon [6] and techniques for assessing heat exchanger performance as in the book by Thulukkanam [7] can be employed to derive the condition parameters while the method proposed by Volponi [8] can be used to correct the condition parameters. Dimensional analysis is a concept employed to aid adequate comparison of similar components while the purpose of parameter correction is to account for variations in engine operating conditions. Once the condition parameters are known and corrected, the chosen technique can be applied.

2.1 Linear GPA

Linear Gas Path Analysis was first introduced by Urban [5]. Its purpose was to provide a means for identifying multiple faults in gas turbine engines, which was a major disadvantage of the Fault Coefficient Matrix (FCM) method used at the time. The principle behind Urban's method is that there exists a linear relationship between engine components condition indicators (health or independent parameters) and gas properties (measured or dependent parameters) and that by manipulating these linear relationships simultaneously, multiple fault detection and isolation is possible. This principle can best be described by the following equation:

$$\delta\overline{m} = F\delta\overline{h} \qquad \textbf{Equation 2-1}$$

Where $\delta\overline{m}$ is the measured (or dependent) parameter deviation vector, $\delta\overline{h}$ is the health (or independent) parameter deviation vector and F is referred to as the influence coefficient matrix (ICM).

The derivation from Equation 2-2 to Equation 2-4 describes how the ICM is defined. Assume a change in a component parameter η is brought about by a change in thermophysical parameters P and T. An analytic representation of the ICM is thus expressed as;

$$\eta = f(P,T) \qquad \textbf{Equation 2-2}$$

Taking the partial derivatives of the relationship in Equation 2-2, we arrive at the expression:

$$d\eta = \left(\frac{\partial\eta}{\partial P}\right)_{T=const} dP + \left(\frac{\partial\eta}{\partial T}\right)_{P=const} dT \qquad \textbf{Equation 2-3}$$

Expressing the parameters as percentages, we obtain:

$$\frac{d\eta}{\eta} = \left(\frac{\frac{\partial\eta}{\eta}}{\frac{\partial P}{P}}\right)_{T=const} \frac{dP}{P} + \left(\frac{\frac{\partial\eta}{\eta}}{\frac{\partial T}{T}}\right)_{P=const} \frac{dT}{T} \qquad \textbf{Equation 2-4}$$

Where the expressions $\left(\frac{\frac{\partial\eta}{\eta}}{\frac{\partial P}{P}}\right)_{T=const}$ and $\left(\frac{\frac{\partial\eta}{\eta}}{\frac{\partial T}{T}}\right)_{P=const}$ are elements in the ICM.

In this method, each engine component is defined by a dimensionless parameter (e.g. component efficiency, pressure ratio) which makes up the health parameter deviation vector; these dimensionless parameters are then related to the measured parameters (e.g. pressure, temperature) in a simplified manner with the ICM for a certain engine operating point.

In Equation 2-1, $\overline{\delta m}$ and F are obtained from sensor measurements and by solving predefined thermodynamic relationships between the dependent and independent parameters respectively; thus, in order to solve for the unknown health parameter deviation, the equation has to be rewritten as:

$$\delta\bar{h} = F'\delta\overline{m} \qquad \textbf{Equation 2-5}$$

Where F' is the inverse of the ICM and is called the fault coefficient matrix (FCM).

However, determining the optimum number of sensors to be placed in the system, selecting an appropriate combination of measured and health parameters and obtaining an accurate ICM are some of the limitations to this technique [3]. Several methods [9-11] have been proposed to address these limitations, and upon application, they were found to be deficient and accompanied by a smearing effect, fault distribution amongst components leading to identification of non-existent faults and underestimating of real faults, in some cases [3].

In applying linear GPA, one would first need to devise a means for obtaining the ICM. According to Urban [12], the ICM is the gradient of the curve that describes the relationship between a thermophysical property and a condition parameter while other thermophysical properties along the cycle remain constant (as expressed in Equation 2-4). For the Triogen system, the gradients can be extracted from trend curves obtained through rig testing or through simulations. Using simulations requires a very robust and thoroughly defined model to ensure that the ICM is accurate enough. In practice, it is impossible to make a robust model for the Triogen system because there are no suitable tools available. In addition, rig testing would require thorough analysis of the system by planting known faults in the components and observing the thermophysical parameter trends using sensors. Accounting for all possible faults takes a lot of time and is not realistic because of system complexity and only small faults can be detected using this method thus, it is unwise to test for large deviations in component parameters. The gradient of the parameter trends determines the ICM and if the entire design range is not accounted for, the ICM cannot be said to be accurate.

2.2 Non-linear GPA

The relationship between engine components condition indicators and gas properties is in practice non-linear. A change in any performance characteristic of a power cycle results in both first and second order effects. For instance, for a gas turbine, a change in the turbine efficiency would result in a change in work output and turbine exit temperature as first order effects, which will then result in a change in the spool speed and fluid inlet mass flow as second order effects. This non-linearity, coupled with altitude effects and a variation in engine operating points for gas turbines when in operation, makes it very difficult to obtain an accurate ICM, especially for large deviations in component health parameters.

Non-linear approaches are a form of Adaptive Modelling (AM). Summarily, AM is a modelling technique that aims to mimic the state of a system through data manipulation. To mimic a system, an adaptive model first starts from an ideal base model and then tunes its defining parameters to arrive at the same state as that system. The deviations that results from tuning the parameters are then used to define and quantify the fault present in that system. Adaptive Modelling necessitates either an extension of the base model equations (which is the best option in terms of stability, flexibility and speed), to ensure that the effects of adaptation are distinguishable from the base model or the addition of an external loop [13].

Non-linear GPA was introduced by Stamatis *et. al.* [14] to eliminate the limitation to condition monitoring, due to linear approximation, present in the linear GPA technique. Non-linear GPA employs surrogate models in estimating engine health status and its fundamental principle is that any system, when properly modelled, can be diagnosed by comparing the estimated model performance data to measured engine performance data. Equation 2-6 depicts the general expression of the objective function and Figure 2-2 demonstrates the principle behind non-linear GPA.

$$\boldsymbol{J} = \sum_{\boldsymbol{i}} \boldsymbol{f}\left(\left|\left|\boldsymbol{z_i} - \boldsymbol{\hat{z}_i}\right|\right|\right) \qquad \textbf{Equation 2-6}$$

Where $\boldsymbol{J}$ is the objective (or cost) function, $\boldsymbol{z_i}$ and $\boldsymbol{\hat{z}_i}$ are the measured and estimated thermophysical property of a parameter $\boldsymbol{z}$ respectively while in Figure 2-2, $\boldsymbol{x_i}$ and $\boldsymbol{\hat{x}_i}$ are the real and predicted component condition parameters respectively, at an operating point $\boldsymbol{i}$ [10].

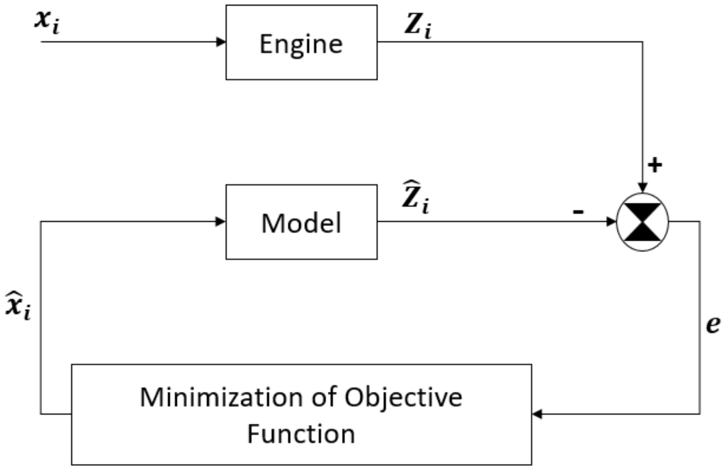

Figure 2-2: Non-linear GPA [10].

In order to define an engine cycle, component condition parameters and fluid properties must be known. Gas turbine engine turbomachinery components possess performance maps, which are used to determine the components performance. Typically, the map is a function of non-dimensional (or independent) parameters, and if these parameters are known, engine cycle (or dependent) parameters can be inferred. In the method by Stamatis *et. al.* [15], an iterative adaptive modelling approach was used. A base map (usually obtained from a similar engine or from rig testing) is scaled, in relation to engine deterioration, using modification factors (MF). The MF is defined as:

$$\boldsymbol{MF_X = \frac{X_{mod}}{X_{ref}}} \qquad \text{Equation 2-7}$$

Where $\boldsymbol{MF_X}$, $\boldsymbol{X_{mod}}$ and $\boldsymbol{X_{ref}}$ are the modification factor, modelled independent parameter value, and referenced independent parameter value of a parameter $\boldsymbol{X}$ respectively [14].

In this approach, component maps of a similar engine are first selected and random values are selected for the modification factors. The modification factors are then used to determine the model independent parameters. Subsequently, the independent parameters are used in estimating the dependent parameters along the gas path using thermodynamic relations. To determine the true value of the modification factors, a minimization problem is introduced, using the method of least squares. For any system, conservation laws must be satisfied; thus, more than one equation (thermodynamic relations and conservation equations) is used in calculating each dependent parameter, and the errors between calculated values for the conservation balance are also included in the minimization problem. The objective function of the problem is shown in Equation 2-8.

$$\boldsymbol{FC = \sum_{i=1}^{m} a_i e_i^2 + \sum_{i=1}^{n} b_i (X_{c_i} - X_{m_i})^2} \qquad \text{Equation 2-8}$$

Where $\boldsymbol{FC}$ is the cost function, $\boldsymbol{X_{c_i}}$ and $\boldsymbol{X_{m_i}}$ are the calculated and measured values respectively, $\boldsymbol{a_i}$ and $\boldsymbol{b_i}$ are weight coefficients depending on measurement and model accuracy and $\boldsymbol{e_i}$ an error term defined as the difference between the calculated values of a dependent parameter $\boldsymbol{X}$ which ensures that conservation laws are satisfied.

The optimization objective is to obtain values of the independent variables that ensures the conservation laws are satisfied and give the minimum error between the calculated and measured dependent parameter values. Repeating this procedure for the full range of operating points for the engine gives the detailed component maps and hence component condition.

Another approach [4] which was developed into a computer program, *PYTHIA*, is based on a combination of Urban's linear method [5] and an iterative Newton Raphson approximation technique to obtain an exact solution. First, a baseline is defined using a healthy engine; a linear approximation of the incremental change in condition parameter is then solved for and added to the initial baseline to create a new baseline. This procedure is continued until the difference between measured and calculated values is minimum. Figure 2-3 describes this approach.

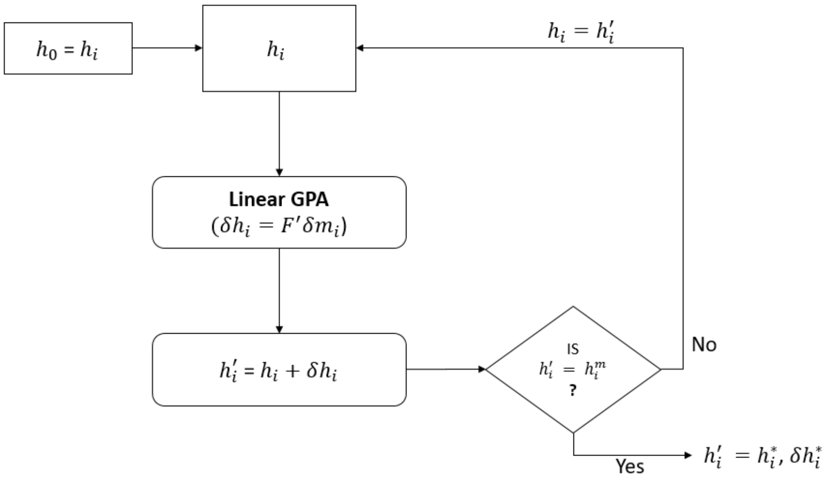

Figure 2-3: The underlying principle of PYTHIA [4].

Other approaches [16-25] also define the diagnostic problem as an optimization problem, similar to the method by Stamatis *et. al.* [15], and employ heuristic methods to minimize the difference between measured and calculated parameters.

Diagnostic results obtained from using non-linear GPA, regardless of the selected approach, are more accurate than results obtained from the linear GPA technique. A visualization of this improvement in accuracy is illustrated in Figure 2-4.

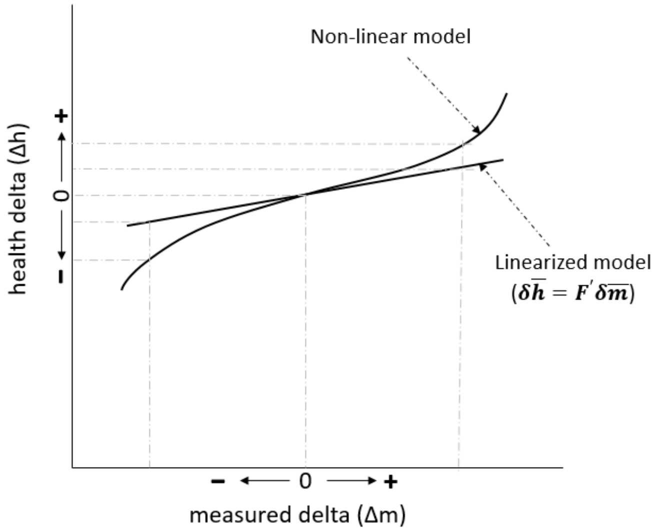

Figure 2-4: Comparison between Linear and Non-linear GPA [3].

Non-linear methods suffer from certain limitations. Extending the base model equations, can lead to a high number of iterations and model complexity; and the addition of an external loop can result in non-convergence in cases where the equations are not properly defined [13]. In the approach by Stamatis *et. al.*, obtaining component maps is a daunting task due to non-homogeneity in engines and sometimes confidentiality. Also, in the method proposed by Escher [4], obtaining an accurate ICM for base calculations is usually very challenging. Furthermore, there is the problem of the iteration stopping at a local minimum, if the optimization method is not robust enough, which could lead to wrong estimation of engine fault magnitude or even failure to identify the fault.

Any of the non-linear GPA approach can be applied to the Triogen ORC system with the right tools and proper adaptation where necessary. Using the method by Stamatis *et. al.* [15] requires component performance maps but only the performance maps for the pumps in the Triogen system are readily available. These maps are not sufficient to infer other parameters except through thermodynamic relations thus the use of modification factors is not possible. However, it is possible to set up an optimization, and determine system faults, by manipulating the thermodynamic relations between components. The method developed by Escher [4] would require a linear approximation for the base calculations and this in turn requires the definition of an ICM for the system. As discussed in the concluding paragraph of section 2.1, this requirement is unrealistic due to the difficulties in obtaining the ICM.

2.3 Genetic Algorithms

Genetic algorithms are optimization techniques, comparable to non-linear GPA methods, which take the non-linearity of engine performance into account. As with non-linear GPA, genetic algorithms aim to minimize the absolute deviation between measured and simulated engine performance parameters. The main difference between the two is that unlike non-linear GPA, genetic algorithms do not include the underlying thermodynamic equations in the optimization when carrying out fault analysis. Equation 2-9 describes a genetic algorithm technique proposed by Zedda and Singh [26], for engine fault diagnostics, which accounts for sensor bias and noise interference.

$$\boldsymbol{J}(\boldsymbol{x},\boldsymbol{w}) = \sum_{\boldsymbol{j=1}}^{\boldsymbol{M}} \frac{(\boldsymbol{z_j} - \boldsymbol{h_j}(\boldsymbol{x},\boldsymbol{w}))^{\boldsymbol{2}}}{(\boldsymbol{z_{od_j}}(\boldsymbol{w})\ .\,\boldsymbol{\sigma_j})^{\boldsymbol{2}}} \qquad \textbf{Equation 2-9}$$

Here, $\boldsymbol{z} \in \boldsymbol{R^M}$ is the measured parameter vector and $\boldsymbol{M}$ is the number of measurements, $\boldsymbol{h} \in \boldsymbol{R^M}$ is the simulated parameter vector, $\boldsymbol{z_{od_j}}$ is the value of the $\boldsymbol{j^{th}}$ measurement in the off-design un-deteriorated condition, $\boldsymbol{\sigma_j}$ is the standard deviation of the $\boldsymbol{j^{th}}$ measurement, $\boldsymbol{x} \in \boldsymbol{R^M}$ is the performance parameter vector and $\boldsymbol{w} \in \boldsymbol{R^M}$ is the vector of the environment and power setting parameters [26].

The measurement noise is taken into account by the standard deviation $\boldsymbol{\sigma_j}$ and is usually assumed to be Gaussian. However, when a Gaussian distribution is deemed inaccurate for the analysis in question, a more robust estimation of the objective function, Equation 2-10, is used.

$$\boldsymbol{J(x,w) = \sum_{j=1}^{M} \frac{|z_j - h_j(x,w)|}{z_{od_j}(w)\,.\,\sigma_j}}$$ **Equation 2-10**

Genetic algorithms are a robust technique based on the mechanics of natural selection. Initially, a set of possible solutions (referred to as a population) is generated randomly, based on predefined deviation limits. Subsequently, each solution set is inputted in the optimization equation and an objective function obtained; the goal is to minimize these objective functions and select the best from the population. To obtain the true minimum objective function, the objective functions are first mapped onto a fitness function; a large fitness translates to a large chance of survival [27]. The genetic algorithm encompasses three fundamental operators: selection, crossover and mutation. The selection operator chooses the best solution sets in the population that yields the minimum objective functions. The crossover operator compares solution sets, identifies the most sensitive parameters in each solution set and tries to improve each solution set, based on other sets within the current population, by exchanging information. The mutation operator then perturbs each solution set, within the defined deviation limits, to ensure that the objective function is not greater than it was before the crossover operator. This optimization process is repeated until the best solution is obtained.

Despite the robustness of this technique, the computation time required is a major drawback. Also, this method is inappropriate for transient analysis due to smearing effects, where fault is propagated over multiple system components [27]. Additionally, as with linear GPA, when the number of measurements is less than the health parameters to be deduced, it is difficult to obtain accurate results. Gulati *et al*. [28] employed the Multiple Operating Point Analysis (MOPS) method proposed by Stamatis and Papailou [11], where data available from multiple operating points are employed to ensure that the measured parameters are more than the health parameters. Using this method, the overall objective function was redefined by summing up the objective functions of the different operating points considered as shown in Equation 2-11.

$$\boldsymbol{J(x,w) = \sum_{m=1}^{OP} \sum_{j=1}^{M} \frac{|z_{jm} - h_j(x,w_m)|}{z_{od_j}(w_m)\,.\,\sigma_j}}$$ **Equation 2-11**

Where $\boldsymbol{OP}$ is the number of operating points.

The simplicity of this multi-objective optimization, which is derived from the summation of the objective functions of the operating points considered, is its disadvantage. Due to the way the objective function is defined, adequate Pareto optimal solutions (a true solution obtained without the devaluation of other solutions) cannot be obtained. This means that simultaneous improvement of corresponding objective vectors is not possible. Several methods [29-31] were proposed to tackle this limitation but they were found to be inadequate. Thus, the general consensus is that standard genetic algorithm techniques are not appropriate for gas turbine engine fault diagnosis due to the intricate relationships that exist between gas turbine components [28].

In this research, the goal is to develop an on-line condition monitoring model. However, Genetic Algorithms, although very promising, cannot be applied to the Triogen ORC system because of the tendency for it to exhibit a smearing effect in transient analysis.

2.4 Artificial Neural Networks

Neural networks are pattern classification algorithms, inspired by the biological central nervous system, which produces a predefined output response for a given input signal [3].

Basically, a neural network is trained by determining the interrelationships between input signals and output response. A neural network may consist of several layers, depending on the desired problem complexity, and training it can either be supervised or unsupervised. In a supervised training, the network is provided with an input vector and the desired output vector; the system goes through an optimization process where the error between the calculated and desired output vector is minimized and then the weights, relating the output to the input vectors, are adjusted accordingly until convergence is achieved. In an unsupervised training, no output is specified; operational experience is exploited to obtain consistent results for a given input vector [32].

Artificial Neural Networks (ANN), when properly developed, can be very effective for fault diagnosis. The benefits of this method, applied to engine fault diagnosis, include easy and quick detection of failure root cause without the need for computation and fault detection irrespective of the availability, quality or complexity of the engine model.

The most common type of neural network, applied to gas turbine fault analysis, is the Feed-Forward Back-Propagation. This technique is made up of three layers: an input, hidden and output layer. In the neural network training process, the input layer receives the observable (or measurable) parameters and sends this information to the hidden layer where the information is processed and a functional relationship is developed and passed to the output layer where the performance (or health) parameters are revealed. A robust neural network depends on rigorous training of the networks, as this determines the accuracy of the functional relationship formed in the hidden layer. In practice, robustness can be ensured by simulating all possible input signal and recording the corresponding output response. However, a large number of networks, long training time and diagnostic accuracy are some of the disadvantages of this neural network method when applied to large scale problems [33, 34].

Another type, classified as competitive learning neural networks, is a statistics based method comprising of several approaches. The first is the Probabilistic Neural Network (PNN) [35-39]. It is considered an application of Bayesian statistics because fault estimates are based on probability inferences from prior case studies, which are stored in the network as mathematical coefficients [10]. Gas turbine fault root cause is identified by the fault pattern that yields the highest probability. The probabilities are determined from the

Euclidean distance between input pattern and patterns stored from case studies via a probability density function.

The second approach of competitive learning neural networks is the Self-Organizing Map (SOM) [40, 41]. SOM is similar to pattern recognition. The input neurons are first tuned to obtain possible input signal patterns, the patterns are then mapped on a lattice in order to extract statistical correlation with the output response based on the position of the neurons in the lattice. To diagnose a faulty engine, the input signal from the engine is assessed on the lattice by comparing it to the patterns stored in the system and the root cause is then inferred.

Another competitive learning neural network approach is a Learning Vector Quantization (LVQ) [42, 43]. The LVQ approach is based on the principle behind the Voronoi diagram. Training of the neural network is done in a similar manner as the other approaches, by tuning a random input pattern and recording the output response. The input space is partitioned into Voronoi cells whose boundaries are determined by the Voronoi Vector points and cell boundaries around a Voronoi point are defined by all the points whose distances are less than or equal to their distances to another Voronoi point. In diagnosing the root cause of a faulty engine, the input signal of that engine is entered in form of a vector; the engine input vectors fall in these cells and any point within a cell is approximated to be equal to the Voronoi point in that cell. The output response corresponding to the Voronoi vector formed from this approximation reveals the root cause.

Other competitive learning neural network approaches include a Counter Propagation Network (CPN) [44, 45], an Adaptive Resonance Theory (ART) [45, 46], a Resource Allocation Network (RAN) [47-51] and a Recurrent Cascade Correlation (RCC) which is a type of RAN [52]. These approaches depend on communication between the input and hidden layers while adapting a given input signal to stored patterns in order to produce an appropriate output response. Unlike the other approaches, RAN has a flexible architecture. It possesses the ability to add new neurons, depending on the pattern inputted into the system, which sufficiently reduces the number of iterations needed, thus making its convergence rate faster than the other competitive learning neural networks approaches [10].

Competitive learning neural networks have been applied to many cases and it has been proven that sufficient results can be obtained when they are employed for fault analysis. However, unlike back-propagation neural networks, competitive learning neural networks have the disadvantage of not having any indication of diagnostic result confidence level. Last but not least, compared to the back propagation neural network, competitive learning neural networks are not as reliable [10].

Applying an ANN technique to the Triogen ORC system would require a comprehensive input signal and output response data in order to train the networks. Presently, the data available at Triogen are raw and it would require a lot of time to process them. For this reason, this method will not be considered.

2.5 Expert Systems

Expert systems were developed for condition monitoring in order to capture expert knowledge and imitate the decision making process of a human expert [53] and to make fault diagnosis and maintenance effective and more convenient [54]. The expert system is a shell consisting of an inference engine and a knowledge base. In the shell, the inference engine is coupled to the knowledge base. The user interacts with the inference engine and the inference engine in turn uses the knowledge stored in the knowledge base to diagnose the engine [10].

Expert systems developed over the years can be classified as rule-based, model-based or case-based. In a rule-based expert system, system reactions to input signals are predefined by the developer; it consists of IF-THEN rules and a translator that accepts the input and returns an action corresponding to that input. Model-based expert systems rely on diagnosis based on comparisons between the active engine and a baseline; statistical methods like the six sigma [55], Bayesian belief network [56-61] and static pattern analysis [38, 47] are then used to make fault inferences based on the active engine deviation from the baseline. Case-based expert systems rely on previous fault diagnosis; this type of expert system recalls previous fault patterns and the corresponding output, compares them to the input fault pattern, adjusts parameters without compromising the fault signature and then makes inferences based on similarities between the input fault pattern and previous diagnostic fault patterns.

Usually, the knowledge engineer has insufficient knowledge about the process being diagnosed and the process engineer has insufficient knowledge about knowledge engineering. A problem that could arise in the developmental stage of expert systems because of this is a situation where there is inadequate or no communication, between the knowledge and process engineer, and this results in a shallow knowledge based expert system. This problem is referred to as a Knowledge engineering bottleneck [62, 63] and it further highlights the need for robustness. However, knowledge acquisition and knowledge accuracy are necessary but difficult to attain in developing a robust expert system hence the adoption of probabilistic and fuzzy logic techniques [3]. Nonetheless, probabilistic and statistical methods are estimated solutions and the estimation of fault magnitudes reduces the reliability of expert system diagnosis. Also, a more robust expert system would require continuous update, as more experience is gained, but this requires a lot of time because after every update, the system has to be validated to ensure that its response to known faults is not altered [3].

The effectiveness of expert systems depends on the wealth and accuracy of recorded cases. In addition, developing an expert system model for the Triogen system will take a considerable amount of time. In addition, a detailed event tree analysis would have to be drawn in order to ascertain fault root cause. Therefore, this method will not be considered.

2.6 Summary

The ideal condition monitoring tool for the Triogen ORC system has to be sufficient and be able to detect, isolate and predict faults within the system as fast as possible. The GTPtracker software is a tool that is primarily designed for gas turbine online condition monitoring, but can be adapted for other energy systems. To adapt the GTPtracker software for the Triogen ORC system, it is essential that an adequate fault detection technique is employed and that has been the focus of this report.

In sections 2.1 to 2.5, the various Gas Path Analysis techniques that have been developed over the years have been described. Ideally, all the methods discussed can be applied to the Triogen ORC system barring the performance requirements of the condition monitoring tool. The basic requirements for an on-line condition monitoring tool are that it must be robust and be able to carry out diagnosis fast enough, so as to ensure that the diagnostic results are sufficient and available early enough to be acted upon. Table 2-1 gives a visual comparison of the methods.

While linear GPA has the advantage of very fast computation time due to linear approximation, it is not robust and was found to be useful only for detecting minor faults (small deviations in condition parameters). Non-linear GPA was developed as an improvement of the linear GPA technique and it has proven to be effective when applied properly; however, setting up the optimization framework is critical and could be the difference between timely intervention and catastrophic damage to a faulty engine. A Genetic Algorithm is a complex non-linear GPA method relying on statistical methods for fault diagnosis; even though it has been tested and proven to be sufficient in fault diagnosis, a true optimum is not always guaranteed because it fails to consider the complex interrelationships between engine components in its optimisation algorithm. Artificial neural networks and expert systems are advanced GPA techniques that links fault signatures to diagnostic results through machine learning. Artificial neural networks possess a hidden layer that communicates with the input signal and produces a diagnosis based on that input signal while expert systems relies on amassing knowledge from a known human expert and using the available knowledge to determine fault root cause. As a result of the uncertainty in the principles behind artificial neural networks and expert systems, a lot of time is needed to predict and completely account for all the possible faults that an engine can encounter, statistical and fuzzy logic methods has to be included in the methodology thus the large computation time needed for these techniques. In addition, statistical inclusion in a model's methodology also reduces its accuracy.

Table 2-1: Relative comparison of the various GPA techniques.

	Linear GPA	Non-linear GPA	Genetic Algorithms	Neural Networks	Expert Systems
Model derivation	Simulations and rig tests	Thermodynamic relations	Statistical inference	Statistical inference	Historical data
Non-linear	No	Yes	Yes	Yes	Yes
Universality	Limited	Unlimited	Limited	Limited	Limited
Complexity	Low	Medium[1]	High	High	High
Computation time	Low	Medium[2]	High	High	High
Accuracy	Low	Medium[3]	High[4]	High[4]	High[4]

1. Can be high depending on desired accuracy.
2. Can be high depending on optimization complexity.
3. Can be high depending on optimization setup.
4. Only if the case being considered was accounted for in the model development. Otherwise low.

Unfortunately, an accurate model must be intricately designed and a model with a high computation time must be as simple as possible. A lot of effort has been put into improving the accuracy and computation time of condition monitoring techniques, as discussed in previous sections. As can be seen in Table 2-1, a high computation time is a consequence of high accuracy and a low computation time translates to low accuracy. The GPA technique to be selected for any project will therefore depend on the degree of accuracy required and the consequence of time. For the Triogen ORC system, the most desirable approach is to employ the use of a surrogate model, which will be developed from a predefined performance model, as in the non-linear GPA approach.

3 Surrogate modelling

As discussed in section 1.2, the GTPtracker has to be configured such that the surrogate baseline model and the active engine can be compared judiciously to derive the necessary index deviations for fault diagnosis. In the original GTPtracker flow process (Figure 1-2), the offline model is utilised in defining the surrogate baseline model for gas turbines by correcting system parameters to account for external effects (e.g. ambient temperature, ambient pressure). However, this research is focused on ORC condition monitoring and differs significantly from gas turbine condition monitoring. In addition, the Triogen ORC system thermophysical parameters are not directly influenced by ambient conditions; thus, they cannot be inferred from it. Furthermore, it is usually the system dynamic properties that dictate the operating condition of an ORC; hence, the surrogate model must be developed such that it can account for different operating conditions.

Methods that have been employed in developing off-design models for ORC systems range from complex methods (e.g. CFD, advanced deterministic methods) to convenient system-level methods (e.g. constant-efficiency method, polynomial-regression method, semi-empirical method) [64].

For this research, the goal is to construct an off-design model, which will give a good indication of the health condition of the Triogen system in real time. However, the main requirement of real time condition monitoring is to be able to run an inexpensive health analysis of the system under consideration within the shortest possible time and still obtain acceptable results; therefore, a system-level method is most suitable for developing the off-design model.

The constant-efficiency method operates under the assumption that the ORC component performance indices remain constant irrespective of its operating point. While this method results in lower computation time, off-design effects on turbomachinery components are not accounted for in the overall model; hence its low accuracy. The polynomial-regression method utilizes polynomial functions to account for varying operating point of ORC system; performance indices are directly defined as a second order quadratic function of the operating point. Although this method also allows for a lower computation time, defining a direct relationship between performance indices and operating condition could result in overfitting effects or Runge's phenomenon especially since the degree of the polynomial is a limiting factor. In addition, extensive information about the ORC system performance must be known (through rig testing or detailed simulation) before this method can be implemented. Semi-empirical methods utilize approximate physics based models to characterize the components in the ORC. Whilst this method yields acceptable accuracy, its complexity results in a higher computation time than the other system-level ORC modelling methods. In summary, constant-efficiency methods are less accurate due to its unrealistic assumptions; polynomial-regression methods could result in extrapolation errors while semi-empirical methods are complex and require a high simulation time.

Nonetheless, the most relevant method to this research is the polynomial-regression method because the objective of this research focuses on identifying the Triogen ORC performance degradation and not necessarily on developing a generic ORC model. However, because extensive performance data (e.g. component performance maps) are not readily available for the Triogen system, a modified polynomial-regression method has been developed for application. The proposed technique employs an equation based modelling approach where the aim is to identify key drivers (control variables) of the Triogen ORC system and use these drivers, together with component design specifications (e.g. allowable pressure drops, geometric dimensions), to define the surrogate baseline model. The reason for this is to develop an exact dynamic model, which eliminates the need for system parameter corrections. Additionally, the control systems present in the Triogen ORC system greatly influences the system cycle thermophysical properties thus making it tricky to implement parameter correction techniques, which further strengthens the suitability of this approach. Figure 3-1 shows a schematic representation of the proposed methodology, which is a modification of the original GTPtracker working principle.

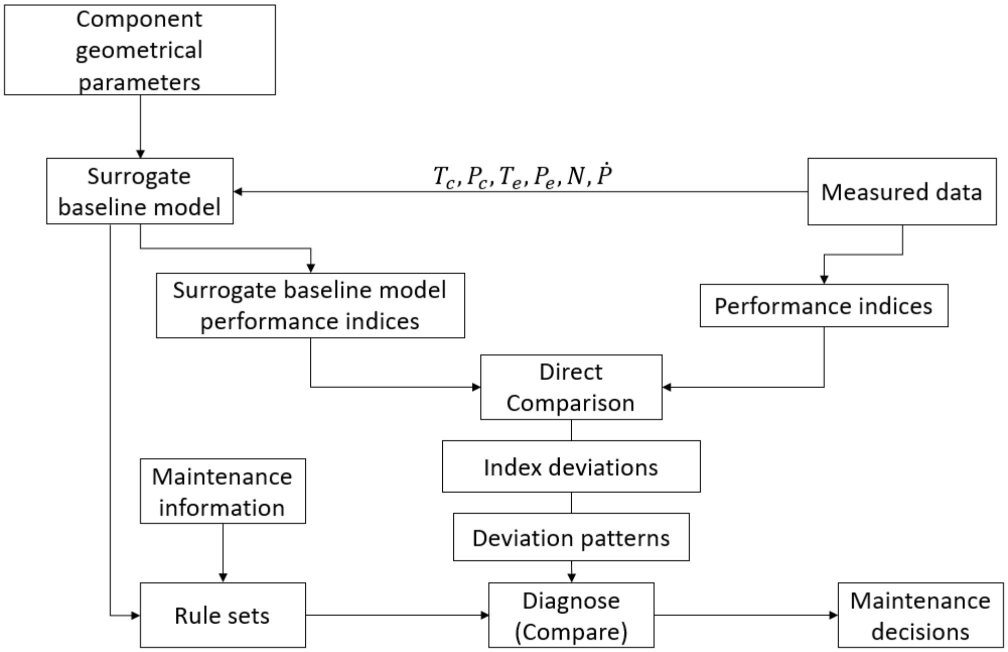

Figure 3-1: Modified GTP flow process.

Furthermore, elements of the surrogate model must be developed and appropriately coupled to satisfy the research objective. Key elements of the surrogate model are a fluid property model and a computation algorithm. The fluid property model is necessary to determine the thermophysical properties while the computation algorithm enables the characterisation of the fluid state across each component with the aid of the fluid property model. With these elements, different models can be developed for the Triogen system. In section 3.1, the method used in deriving the fluid property model is presented while the different models derived for the Triogen ORC system are discussed in section 3.2.

3.1 Fluid property modelling

For both the surrogate model and the active engine, component performance indices (e.g. efficiencies, pressure ratios) need to be determined to compute deviations for fault diagnosis. The GTPtracker software is capable of calculating component performance indices either using predefined functions or component performance maps. Predefined functions are mathematical relations of component performance indices expressed as a function of known or measurable system parameters while component maps are charts, describing component performance range, created from extensive rig testing. However, the option to use predefined functions is the most ideal because component maps for the Triogen system components are not readily available. For thermodynamic systems, performance indices are usually a function of the fluid properties and the working fluid of the Triogen system is toluene; thus, the performance indices for each component is defined as a function of the thermophysical property of toluene for the operating range of the component under consideration.

To define the performance indices for any component, it is imperative to first identify all possible failure mechanisms pertaining to that component. Subsequently, the performance indices that can adequately identify the failure mechanisms can then be derived. However, performance indices are functions of the working fluid thermophysical properties; thus, for a component performance index to be calculated, the working fluid thermophysical properties that define the desired performance index for that component must first be determined.

3.1.1 Method to derive state equations

To compute the working fluid thermophysical properties, a technique has been developed so that any desired thermophysical property can be expressed as a function of two known thermophysical properties at a control point. The working fluid of the Triogen ORC is toluene and its thermophysical properties are well known and readily available from documented results of extensive experiments. A curve-fitting algorithm, written using Matlab and presented in the Appendix, has been developed to aid generate these equations. This method is essentially the translation of curves, describing the relationship between toluene thermophysical properties, into mathematical equations. A generic explanation of how this technique works is presented using Equation 3-1 to Equation 3-8 for better understanding.

Assuming that for a particular component $\boldsymbol{c}$, a set of performance indices $\boldsymbol{P_i^c}$ exist and is a function of a set of thermophysical properties $\boldsymbol{T_j}$; then this statement can be expressed as:

$$P_i^c = f(T_1, T_2 \dots T_n) \quad j = 1,2, \dots, n$$ **Equation 3-1**

Where n is the number of thermophysical parameters needed to compute the set of performance indices P_i^c.

This technique obeys the state postulate, which says that the state of a simple compressible system is completely specified by two independent intensive properties. Thus, to derive a function for computing any unknown thermophysical property, the proposed function must be expressed as an n^{th}order equation such that two of the known thermophysical properties are the only unknowns within the equation. For example, maintaining the conventions used in Equation 3-1, if a particular performance index P_1^c is a function of a thermophysical property T_1 but T_1 is unknown and is a function of two known thermophysical properties T_2 and T_3, then:

$$P_1^c = f(T_1 = f(T_2, T_3)) \qquad \textbf{Equation 3-2}$$

In order to obtain T_1 to be able to compute P_1^c , the desired function to calculate T_1 must be of the form:

$$T_1 = f(T_2, T_3) \qquad \textbf{Equation 3-3}$$

Using the same technique, one can derive functions to compute any desired thermophysical property easily. Furthermore, because of the non-linear behaviour of thermodynamic cycle working fluids, it is important to derive component specific functions such that it is most accurate within the operating range of the component under consideration i.e. Equation 3-3 should be derived considering the operating range of the component $\boldsymbol{c}$ with respect to T_2 and T_3. Consequently, the accuracy of T_1 will depend on the bounds of T_2 and T_3.

$$T_1 = f(T_2, T_3) \in \ P_1^c \qquad \textbf{Equation 3-4}$$

Subject to:

$$a \leq T_1 \leq b$$

$$c \leq T_2 \leq d$$

$$e \leq T_3 \leq f$$

Where a, c and e are lower bounds and b, $d$and f are the upper bounds of the thermophysical properties T_1, T_2 and T_3.

Usually, it is quite challenging to perform a direct derivation of a function with two variables especially in cases where the variables are dependent on each other. In this research, such a situation is inevitable because a desired thermophysical property of the working fluid can only be determined with the knowledge of two other thermophysical property. As a result, it is imperative to develop a methodical mathematical technique that is easy to implement and one that will yield accurate results. For a more explicit description of this technique, in deriving Equation 3-4, one would first express T_1 as a function of T_2 then subsequently express the constants of the resulting equation as a function of T_3 or vice versa. i.e.

$$T_1 = \sum_{i=0}^{n} k_i T_2^i \qquad \textbf{Equation 3-5}$$

Where k_i is a set of constants of the function relating T_1 to T_2 and n is the degree of the function.

Expressing k_i as a function of T_3 and substituting the resulting expression into Equation 3-5 yields:

$$k_i = f(T_3) = \sum_{j=0}^{m} w_j T_3^j$$

Equation 3-6

$$T_1 = \sum_{i=0}^{n} \sum_{j=0}^{m} w_j T_3^j \, T_2^i$$

Where w_j is a set of constants of the function relating k_i to T_3 and m is the degree of the function derived for k_i. The value of n and m are independent of each other and only influence the accuracy of the function.

Hence, the general expression for the performance index P_1^c is:

$$P_1^c = f\left(\sum_{i=0}^{n} \sum_{j=0}^{m} w_j T_3^j \, T_2^i \right)$$

Equation 3-7

However, the irregular nature of the relationship between toluene thermophysical properties makes it necessary to employ equations of higher orders. The consequence of this is that the equations become more prone to overfitting effects and Runge's phenomenon; thus, one has to reach a compromise between maintaining overall accuracy and generating data specific equations. Through rigorous testing and observations, it has been determined that the best way to solve this inevitable problem is to first derive the general function analytically, and then empirically generate an extra fit equation to increase the accuracy. The general equation in this case will then take the form:

$$P_1^c = f\left(\sum_{i=0}^{n} \sum_{j=0}^{m} w_j T_3^j \, T_2^i \right) + \sum_{k=0}^{o} \omega_k T_2^k$$

Equation 3-8

Where ω_k is a set of constants of the function relating the empirical fit to T_2 and k is the degree of the function derived for the empirical fit. In addition, the value of k only influences the accuracy of the extra fitting.

3.1.2 State equations

In this section, the state equations, for the different components of the Triogen ORC, based on the technique described in the previous sub-section are presented. To ensure that the equations are a true representation of toluene thermophysical properties, the Sum of Squares due to Error (SSE), R-square, adjusted R-square and Root Mean Square Error (RMSE) were selected for evaluation of goodness of fit.

The Sum of Squares due to Error is a measure of the total deviation of a set of response values from the fit. It essentially quantifies the difference between the data being analysed and the predicted estimate and is a good indication of the accuracy of the estimated model equation. Intuitively, a smaller value of the SSE indicates good accuracy whereas a larger value indicates poor accuracy. It is expressed as:

$$SSE = \sum_{i=1}^{n} w_i (y_i - \hat{y}_i)^2$$ **Equation 3-9**

Where y_i is the i^{th} value of a data point to be predicted and $\hat{y}_i$ is the predicted value of y_i.

The R-square value essentially provides an indication of the magnitude of variation in a dependent variable that is predictable from an independent variable. Its value ranges from 0 to 1 and a value closer to 1 signifies that a model involving the dependent and independent variables accounts for a greater amount of variation.

$$R - square = \frac{SSR}{SST}$$ **Equation 3-10**

$$SSR = \sum_{i=1}^{n} w_i (\hat{y}_i - \bar{y})^2$$

$$SST = \sum_{i=1}^{n} w_i (y_i - \bar{y})^2$$

Where SSR is the Sum of Squares of the Regression, SST is the total sum of squares, y_i is the ith value of a data point to be predicted, $\bar{y}$ is the mean of the observed data and $\hat{y}_i$ is the predicted value of y_i.

The adjusted R-square is in general a statistic that measures the accuracy or quality of fit when two models are nested. Its values could be negative when some of the data points in the model equation do not help in the prediction and a value closer 1 indicates a good fit for the model.

$$adjusted\ R - square = 1 - \frac{SSE(n-1)}{SST(v)}$$ **Equation 3-11**

$$v = n - m$$

Where SSE is the Sum of Squares due to Error, SST is the total sum of squares, n is the number of response values, m is the number of fitted coefficients and v indicates the number of independent information involving the n data points.

The Root Mean Squared Error also known as the standard error of regression is essentially an estimation of the standard deviation of the randomness in the data. It represents the standard deviation of the difference between predicted and observed values. A close to 0 indicates a better fit and is more desirable.

$$RMSE = s = \sqrt{MSE}$$ **Equation 3-12**

$$MSE = \frac{SSE}{v}$$

Where MSE is the Mean Squared Error and v indicates the number of independent information involving the data points.

For this research, the general allowable tolerance for the selected goodness of fit statistics are shown in Table 3-1.

Table 3-1: Goodness of fit tolerance for state equations

Statistic	**Tolerance**
Sum of Squares due to Error (SSE)	< 0.1
R-square	> 0.85
Adjusted R-square	> 0.85
Root Mean Square Error	< 0.1

Detailed state equations that have been developed and validated for estimating the desired thermophysical properties at each control point are as follows.

3.1.2.1 Storage vessel and compressor exit (Control points 1 and 10)

The Triogen ORC storage vessel, as the name implies, houses the working fluid (toluene) whereas the condenser is utilised to return the fluid to its initial state after the thermodynamic process. For these control points, the assumption of thermodynamic equilibrium holds; therefore, the properties at both control points are the same. In addition, the known thermophysical parameters are the condensing pressure and temperature of the working fluid and these two parameters are utilised to determine the other necessary thermophysical properties within the design operating range. These components operate between a temperature range of 50°C to 80°C and a pressure range from 0.01 bar to 1 bar for the Triogen system; thus, these values are selected as the design limits for the proposed functions. A systematic implementation of the technique described in sub-section 3.1.1 yields the expressions needed to calculate the entropy, enthalpy and density.

The expression for calculating the enthalpy is the second order polynomial equation of the form:

$$\begin{aligned} h_1(P_1, T_1) &= h_{10}(P_{10}, T_{10}) \\ &= (2.719e^{-9}T_1^2 - 8.269e^{-8}T_1 + 9.318e^{-6})P_1^2 \\ &+ (-4.444e^{-9}T_1^3 - 1.714e^{-7}T_1^2 - 8.703e^{-5}T_1 \\ &+ 0.08099)P_1 \\ &+ (1.111e^{-5}T_1^3 - 4.048e^{-4}T_1^2 + 1.746T_1 \\ &- 202.4)\ (KJKg^{-1}) \end{aligned}$$

Equation 3-13

Subject to:

$$0.01 \leq P_1 \leq 1 \ \ (bar)$$

$$50 \leq T_1 \leq 80 \ \ (°C)$$

In addition, the entropy derived here is an input to estimate the isentropic enthalpy of the pre-feed pump to be able to determine the actual enthalpy hence the need for the first order polynomial expression:

$$s_1(P_1, T_1) = (-4.9e^{-7}T_1 - 1.1e^{-4})P_1 + (-2.952e^{-6}T_1^2 + 5.814e^{-3}T_1 - 0.6077)\ (KJKg^{-1}K^{-1})$$ **Equation 3-14**

Subject to:

$$0.01 \leq P_1 \leq 1\ \ (bar)$$

$$50 \leq T_1 \leq 80\ \ (°C)$$

Finally, the density is needed to compute the total properties at the control points, which is needed to calculate the total-to-total pressure ratio. The function to calculate the density is a second order polynomial expressed as:

$$\rho_1(P_1, T_1) = (-1.017e^{-8}T_1^2 + 3.735e^{-7}T_1 - 4.348e^{-5})P_1^2 + (3.105e^{-6}T_1^2 + 2.845e^{-4}T_1 + 7.088e^{-2})P_1 + (-4.762e^{-4}T_1^2 - 0.9038T_1 + 885.1)(Kgm^{-3})$$ **Equation 3-15**

Subject to:

$$0.01 \leq P_1 \leq 1\ \ (bar)$$

$$50 \leq T_1 \leq 80\ \ (°C)$$

In summary, the condensing pressure and temperature are control variables of the ORC design point. These variables are utilised in determining the enthalpy, entropy and density at control points 1 and 10. The enthalpy is an input to define the isentropic efficiency of the main pump while the density is utilised to estimate the total properties, and thus the total-to-total pressure ratio.

3.1.2.2 Pre-feed pump (Control point 3)

The primary function of the pre-feed pump is to provide suction head for the main pump due to its orientation. Additionally, the pressure energy provided by the pre-feed pump is important for lubricating the bearings and for cooling the turbo-generator. The lubrication pressure is very important for the life cycle of the turbo-generator as a drop in pressure supplied could cause severe damage. As discussed in sub-section 3.2.2, the pre-feed pump requires several inputs from the storage vessel and the main pump to compute thermophysical properties for the surrogate baseline model. Amongst the turbomachinery components in the Triogen system, it is the only one not manufactured in-house. The entropy from the storage vessel exit is utilised together with the pre-feed pump isentropic efficiency to compute the actual enthalpy and together with the pressure calculated from the main pump, the other true thermophysical properties at the exit of the pre-feed pump are estimated.

The desired thermophysical properties for this component are the pressure, temperature, enthalpy and entropy; but, in computing the actual enthalpy, the isentropic efficiency must be known. However, the pre-feed pump isentropic efficiency is unknown and must be derived from the power curve provided by the manufacturer. The known thermophysical parameters at this control point are the entropy, from the fluid exiting the storage vessel, and the pressure which is obtained from the expression:

$$P_3 = P_5 - \left(\frac{\rho_1(\pi D_5 N_5)^2 \Psi_5}{100{,}000}\right)\ (bar)$$

Equation 3-16

As mentioned previously, the main pump shaft diameter and head coefficient are design parameters while the shaft rotational speed is a control variable. Using the pressure and entropy, the isentropic enthalpy can be calculated using the fourth order polynomial:

$$\begin{aligned} h_{3s}(P_3, s_1) = {} & (-3.106e^{-4}P_3^2 + 6.695e^{-3}P_3 - 1.735)s_1^4 \\ & + (-3.447e^{-4}P_3^2 + 1.245e^{-2}P_3 + 4.172)s_1^3 \\ & + (-2.273e^{-4}P_3^2 + 1.789e^{-2}P_3 + 95.73)s_1^2 \\ & + (-1.136e^{-3}P_3^2 + 4.523e^{-2}P_3 + 383.7)s_1 \\ & + (-2.108e^{-5}P_3^2 + 0.1285P_3 \\ & - 0.1304)(KJKg^{-1}) \end{aligned}$$

Equation 3-17

Subject to:

$$1 \leq P_3 \leq 10\ \ (bar)$$

$$-0.4 \leq s_1 \leq -0.2\ \ (KJKg^{-1}K^{-1})$$

Since the isentropic efficiency of the pre-feed pump is unknown, it must be estimated alternatively. The manufacturer has provided performance curves for power and head as a function of the volume flow rate thus either property can be estimated when the other is known. The pre-feed pump is a constant speed machine and the performance curves provided for the manufacturer is for a single speed. Nonetheless, the affinity laws were utilised at this stage to obtain the performance curves of the main-pump for a wider range of operating speeds before deriving the equations. Hence, the equations are still valid for different operating speeds of the pre-feed pump. In this research, the pressures at control point 3 and 1 are easily deducible; therefore, the head generated by the pre-feed pump can be estimated using the expression:

$$\Delta H = \frac{\Delta P}{\rho g} = \frac{(P_3 - P_1)1e^5}{\rho_1 g}\ (m)$$

Equation 3-18

Then, the corresponding volume flow rate can be estimated from the expression:

$$\begin{aligned}\dot{V}_3(N_3, \Delta H) = {} & (-9.36e^{-3}\exp(-6.9e^{-3}N_3) \\ & - 1.897e^{-4}\exp(-2.966e^{-3}N_3))\Delta H^3 \\ & + (1.58e^{-2}\exp(-4.869e^{-3}N_3) \\ & + 1.029e^{-3}\exp(-1.683e^{-3}N_3))\Delta H^2 \\ & + (-0.55\exp(-2.38e^{-3}N_3) \\ & - 0.178\exp(-3.959e^{-4}N_3))\Delta H \\ & + (9.919e^{-3}N_3 - 1.277e^{-3})\ (m^3s^{-1})\end{aligned}$$

Equation 3-19

In addition, the corresponding power consumed by the main pump can be estimated from the expression:

$$\begin{aligned}\dot{P}_3(\dot{V}_3, N_3) = {} & 1.884e^{-3}\dot{V}_3^3 + (-2.45e^{-5}N_3 + 1.17e^{-6})\dot{V}_3^2 \\ & + (-5.918e^{-8}N\,{}_3^2 - 9.25e^{-9}N_3 + 7.336e^{-7})\dot{V}_3 \\ & + 7.846e^{-6}N_3^2 - 1.139e^{-2}N_3 + 5.333\ (KW)\end{aligned}$$

Equation 3-20

And the total mass flow in the system can be calculated from:

$$\dot{m}_1 = \rho_1\dot{V}_3\ (Kgs^{-1})$$

Equation 3-21

The isentropic efficiency of compressors and pumps is defined as the ratio of the isentropic work to the actual work and can be expressed as:

$$\eta_{3s} = \frac{h_{3s} - h_1}{h_3 - h_1} = \frac{\dot{m}_1(h_{3s} - h_1)}{\dot{P}_3}\ (-)$$

Equation 3-22

Subsequently, the actual enthalpy at the pre-feed pump exit can be estimated using the expression:

$$h_3 = h_1 + \frac{\dot{P}_3}{\dot{m}_1}\ (KJKg^{-1})$$

Equation 3-23

The actual temperature can then be computed from the pressure and enthalpy by using the second order polynomial:

$$\begin{aligned}T_3(P_3, h_3) = {} & (-1.515e^{-9}P_3^2 + 1.021e^{-7}P_3 - 2.849e^{-4})h_3^2 \\ & + (2.652e^{-6}P_3^2 + 8.356e^{-5}P_3 + 0.4949)h_3 \\ & + (-7.576e^{-4}P_3^2 - 2.197e^{-2}P_3 + 110.5)\ (°C)\end{aligned}$$

Equation 3-24

Subject to:

$$1 \leq P_3 \leq 10\ \ (bar)$$

$$-115 \leq h_3 \leq -55\ \ (KJKg^{-1})$$

And the entropy, which is needed to calculate the properties at the main pump, is expressed as:

$$\begin{aligned} s_3(P_3,T_3) = {} & (6.09e^{-12}T_3^2 - 5.262e^{-12}T_3 + 4.163e^{-8})P_3^2 \\ & + (-2.476e^{-9}T_3^2 - 1.681e^{-7}T_3 \\ & - 1.203e^{-4})P_3 + (-2.952e^{-6}T_3^2 \\ & + 5.814e^{-3}T_3 - 0.6077)\ (KJKg^{-1}K^{-1}) \end{aligned}$$

Equation 3-25

Subject to:

$$1 \le P_3 \le 10\ \ (bar)$$

$$50 \le T_3 \le 80\ \ (°\text{C})$$

In addition, it is equally important to calculate performance indices of the pre-feed pump for the active engine. However, a different expression for the enthalpy must be derived as a function of the measured pressure and temperature. This expression is a second order polynomial and is as follows:

$$\begin{aligned} h_3(P_3,T_3) = {} & (2.325e^{-9}T_3^2 - 3.455e^{-8}T_3 + 7.634e^{-6})P_3^2 \\ & + (-3.333e^{-9}T_3^2 - 4e^{-7}T_3^2 - 7.167e^{-5}T_3 \\ & + 8.065e^{-2})P_3 \\ & + (3.333e^{-6}T_3^3 + 1.1e^{-3}T_3^2 + 1.651T_3 \\ & - 200.4)\ (KJKg^{-1}) \end{aligned}$$

Equation 3-26

Subject to:

$$1 \le P_3 \le 10\ \ (bar)$$

$$50 \le T_3 \le 80\ \ (°\text{C})$$

In summary, to calculate the thermophysical properties at the pre-feed pump exit, first, the pressure is obtained by subtracting the head delivered by the main pump from the pressure at the main pump exit; the actual enthalpy is then obtained from the power and mass flow rate, which are obtained from performance curves provided by the manufacturer. The pressure and enthalpy are then utilised in calculating the entropy.

3.1.2.3 Main pump (Control point 5)

The function of the main pump is to raise the pressure of the working fluid to the maximum cycle pressure. It operates at the same rotational speed as the turbine and generator. Triogen developed this component in-house but it has not been tested extensively and so performance maps are not readily available. Although the pressure at the main pump exit is easily determined, knowledge of one extra thermophysical property is necessary to compute the others. The entropy calculated for the pre-feed pump exit is thus an input and can be used to determine the isentropic enthalpy. In turn, the isentropic enthalpy coupled with the isentropic efficiency can be used to estimate the actual enthalpy, which can then be used in calculating the other thermophysical properties. The pressure is calculated as:

$$P_5 = P_6 + \nabla P_6 \ (bar) \tag{Equation 3-27}$$

And the isentropic enthalpy is derived using the entropy at the pre-feed pump exit and the pressure suing the fourth order polynomial:

$$\begin{aligned} h_{5s}(P_5, s_3) = {} & (4.392 \sin(5.246e^{-2}P_5 + 3.43) \\ & + 2.754 \sin(6.772e^{-2}P_5 + 6.18))s_3^4 \\ & + (-5.762e^{-5}P_5^2 + 1.099e^{-2}P_5 + 4.157)s_3^3 \\ & + (-5.714e^{-5}P_5^2 + 1.786e^{-2}P_5 + 95.72)s_3^2 \\ & + (2.222e^{-5}P_5^3 - 1.81e^{-3}P_5^2 + 7.706e^{-2}P_5 \\ & + 383.4)s_3 \\ & + (-9.524e^{-6}P_5^2 + 0.1284P_5 \\ & - 0.1313) \ (KJKg^{-1}) \end{aligned} \tag{Equation 3-28}$$

Subject to:

$$10 \leq P_5 \leq 40 \ \ (bar)$$

$$-0.4 \leq s_3 \leq -0.1 \ \ (KJKg^{-1}K^{-1})$$

The isentropic efficiency of the main pump is unknown for this research but the efficiency curve for a dynamically similar pump is selected and scaled for application. However, the efficiency curve is a function of the flow coefficient and thus the flow coefficient must first be determined. Recall from the assumptions that the main mass flow rate is the mass flow rate through the main pump up until the condenser exit; thus, the mass flow rate through the main pump is the same as that through the turbine. In fact, the nozzle (turbine stator), which has been designed to be chocked during operation, dictates this so-called main mass flow rate; therefore, the main mass flow rate can be determined from the nozzle. In this research, another assumption made is that the working fluid behaves like a perfect gas in the nozzle and thus the ideal gas relations to calculate the critical thermophysical properties are valid. The main mass flow rate is thus expressed as:

$$\dot{m}_2 = \rho_{crt} A c_{crt} \ (Kgs^{-1}) \tag{Equation 3-29}$$

Where the critical density and speed of sound are calculated as a function of the critical pressure and temperature.

$$\begin{aligned}\rho_{crt}(P_{crt}, T_{crt}) = {} & (-1.288e^{-9}P_{crt}^{4} + 5.937e^{-8}P_{crt}^{3} \\ & - 1.012e^{-6}P_{crt}^{2} + 6.994e^{-6}P_{crt} \\ & - 1.659e^{-5})T_{crt}^{3} \\ & + (1.28e^{-6}P_{crt}^{4} - 5.887e^{-5}P_{crt}^{3} \\ & + 1.003e^{-3}P_{crt}^{2} - 6.93e^{-3}P_{crt} \\ & + 1.644e^{-2})T_{crt}^{2} \\ & + (-4.242e^{-4}P_{crt}^{4} + 0.01945P_{cre}^{3} \\ & - 0.3316P_{crt}^{2} + 2.285P_{crt} - 5.43)T_{crt} \\ & + (0.04682P_{crt}^{4} - 2.138P_{crt}^{3} + 36.49P_{crt}^{2} \\ & - 248.4P_{crt} + 596.6) \\ & + (1.067e^{-3}P_{crt}^{3} + 0.01P_{crt}^{2} + 0.1033P_{crt} \\ & - 0.52)\ (Kgm^{-3})\end{aligned}$$

Equation 3-30

Subject to:

$$5 \leq P_{crt} \leq 25\ \ (bar)$$

$$150 \leq T_{crt} \leq 350\ \ (°\mathrm{C})$$

For the equation to calculate the critical density, an extra fit is necessary because of the peculiar nature of the density at higher pressures and temperatures. The density at low pressures and temperatures possess very favourable relations to the pressure and temperature unlike that at higher temperatures and pressures.

$$\begin{aligned}c_{crt}(P_{crt}, T_{crt}) = {} & (-5.59e^{-8}P_{crt}^{4} + 2.435e^{-6}P_{crt}^{3} \\ & - 4.237e^{-5}P_{crt}^{2} + 2.169e^{-4}P_{crt} \\ & - 7.415e^{-4})T_{crt}^{2} \\ & + (3.699e^{-5}P_{crt}^{4} - 1.604e^{-3}P_{crt}^{3} \\ & + 0.02826P_{crt}^{2} - 0.1372P_{crt} + 0.678)T_{crt} \\ & + (-6.168e^{-3}P_{crt}^{4} + 0.2671P_{crt}^{3} - 4.786P_{crt}^{2} \\ & + 20.4P_{crt} + 93.9)\ (ms^{-1})\end{aligned}$$

Equation 3-31

Subject to:

$$5 \leq P_{crt} \leq 25\ \ (bar)$$

$$150 \leq T_{crt} \leq 350\ \ (°\mathrm{C})$$

Since the temperature and pressure at the evaporator exit (control point 7) have been selected as control variables for the model, the critical pressure and temperature can be easily derived using the standard formulas:

$$P_{crt} = P_7 \left(\frac{2}{\gamma + 1}\right)^{\left(\frac{\gamma}{\gamma-1}\right)}$$ **Equation 3-32**

$$T_{crt} = T_7 \left(\frac{2}{\gamma + 1}\right)$$

The flow coefficient for the main pump is defined as the ratio of the discharge throat velocity to the impeller tip speed and can then be calculated using the expression:

$$\varphi_5 = \frac{\frac{\dot{m}_2}{\rho_1 \left(\frac{2\pi d_5^2}{4}\right)}}{\pi D_5 N} = \frac{2\dot{m}_2}{\rho_1 \pi d_5^2 \pi D_5 N}$$ **Equation 3-33**

The factor 2 in the numerator of the final expression is present because the main pump has two discharge areas.

The efficiency relation as a function of the flow coefficient, obtained from the scaled performance curve, is:

$$\eta_{5s} = \frac{-0.4827\varphi_5^2 + 0.5111\varphi_5 - 3.077e^{-3}}{\varphi_5^4 - 2.328\varphi_5^3 + 1.914\varphi_5^2 - 1.199\varphi_5 + 0.7444}$$ **Equation 3-34**

Then the actual enthalpy at the main pump exit can be calculated using:

$$h_5 = \left[\frac{h_{5s} - h_3}{\eta_{5s}}\right] + h_3 \ (KJKg^{-1})$$ **Equation 3-35**

When the pressure and enthalpy are known, the other thermophysical properties can be determined. The temperature is computed using the third order polynomial:

$$\begin{aligned} T_5(P_5, h_5) = {} & (1.193e^{-10}P_5 + 1.982e^{-7})h_5^3 \\ & + (6.28e^{-8}P_5 - 2.328e^{-4})h_5^2 \\ & + (9.452e^{-5}P_5 + 0.4994)h_5 \\ & + (-3.357e^{-2}P_5 + 110.7) \ (°\text{C}) \end{aligned}$$ **Equation 3-36**

Subject to:

$$10 \leq P_5 \leq 40 \ \ (bar)$$

$$-115 \leq h_5 \leq -50 \ \ (KJKg^{-1})$$

And the specific heat capacity is computed from the expression:

$$c_{p_5}(P_5,T_5) = (3.524e^{-13}P_5^2 - 8.562e^{-11}P_5 - 1.095e^{-8})T_5^3 + (-2.476e^{-11}P_5^2 + 2.681e^{-9}P_5 + 5.564e^{-6})T_5^2 + (2.381e^{-9}P_5^2 - 1.298e^{-6}P_5 + 2.944e^{-3})T_5 + 1.623\ (KJKg^{-1}K^{-1})$$

Equation 3-37

Subject to:

$$10 \le P_5 \le 40\ \ (bar)$$

$$50 \le T_5 \le 80\ \ (°\mathrm{C})$$

The specific heat capacity is needed to calculate the temperatures at the recuperator hot and cold side exits using the formula for effectiveness.

Finally, the expression for the enthalpy as a function of pressure and temperature, which is needed for the active engine is expressed as:

$$h_5(P_5,T_5) = (-3.729e^{-9}P_5 + 1.128e^{-6})T_5^3 + (-1.714e^{-7}P_5 + 1.542e^{-3})T_5^2 + (-8.33e^{-5}P_5 + 1.621)T_5 + (0.08P_5 - 199.7)\ (KJKg^{-1})$$

Equation 3-38

Subject to:

$$10 \le P_5 \le 40\ \ (bar)$$

$$50 \le T_5 \le 80\ \ (°\mathrm{C})$$

The reason for deriving this function is to be able to compute the isentropic efficiency for the active engine, which is a performance index for this component.

3.1.2.4 Recuperator hot and cold side (Control points 6 and 9)

The recuperator essentially improves the thermal efficiency by reducing the condenser work and the overall efficiency by reducing the heat needed in the evaporator of the ORC cycle. The hot fluid exiting the recuperator passes through the hot side and is used to pre-heat the cold fluid going through the cold side before it goes through the evaporator. The pressure at the recuperator cold side exit is easily determined since the evaporating pressure is a control variable and the pressure at the recuperator hot side exit can be determined since the condensing pressure is also a control variable. Nonetheless, to calculate other thermophysical properties at each of the control points, one must have knowledge of one more thermophysical property. However, the recuperator is not a turbomachinery component; therefore, instead of using the isentropic efficiency approach as in the turbomachinery components, the effectiveness of the recuperator has been selected as a control variable and employed to compute the temperatures at the hot and cold side exit.

The pressure at the recuperator cold side exit is calculated as:

$$P_6 = P_7 + \nabla P_7 \ (bar)$$ **Equation 3-39**

And the pressure of the recuperator hot side exit is:

$$P_9 = P_{10} + \nabla P_{10} \ (bar)$$ **Equation 3-40**

Subsequently, the maximum heat available for transfer in the recuperator is computed from the expression:

$$\dot{Q}_{max} = \ c_{p_8}\dot{m}_2\big((T_8 - T_5) + 273\big) \ (KW)$$ **Equation 3-41**

Then the actual transferable heat in the recuperator is:

$$\dot{Q} = \ \varepsilon\dot{Q}_{max} \ (KW)$$ **Equation 3-42**

Then the temperature at the recuperator cold side exit is calculated from:

$$T_6 = \left[(T_5 + 273) + \left(\frac{\dot{Q}}{\dot{m}_2 c_{p_5}}\right)\right] - 273 \ (°\mathrm{C})$$ **Equation 3-43**

And the temperature of the recuperator hot side exit is:

$$T_9 = \left[(T_8 + 273) - \left(\frac{\dot{Q}}{\dot{m}_2 c_{p_8}}\right)\right] - 273 \ (°\mathrm{C})$$ **Equation 3-44**

The pressures and temperatures at the recuperator hot and cold side exit are known and can then be used to determine the enthalpy. The enthalpy at the recuperator cold side exit can be computed from the third order polynomial:

$$\begin{aligned} h_6(P_6, T_6) = {} & (1.678e^{-10}P_6^2 - 3.219e^{-8}P_6 + 2.029e^{-6})T_6^3 \\ & + (-5.452e^{-8}P_6^2 + 9.451e^{-6}P_6 \\ & + 1.189e^{-3})T_6^2 \\ & + (7.619e^{-6}P_6^2 - 1.267e^{-3}P_6 + 1.666)T_6 \\ & + (-3.571e^{-4}P_6^2 + 0.1315P_6 \\ & - 201.7) \ (KJKg^{-1}) \end{aligned}$$ **Equation 3-45**

Subject to:

$$15 \leq P_6 \leq 50 \ \ (bar)$$

$$90 \leq T_6 \leq 200 \ \ (°\mathrm{C})$$

And the enthalpy at the recuperator hot side exit is estimated from the third order polynomial:

$$
\begin{aligned}
h_9(P_9, T_9) = {} & (7.919e^{-7}P_9 - 8.451e^{-7})T_9^3 \\
& + (-4.771e^{-4}P_9 + 2.133e^{-3})T_9^2 \\
& + (3.472P_9^3 - 1.518P_9^2 + 0.3325P_9 \\
& + 1.005)T_9 \\
& + (463P_9^3 - 208.3P_9^2 + 18.03P_9 \\
& + 226.9)\ (KJKg^{-1})
\end{aligned}
$$

Equation 3-46

Subject to:

$$0.1 \le P_9 \le 0.2 \ \ (bar)$$

$$60 \le T_9 \le 200 \ \ (°C)$$

In addition, the density at the recuperator cold side exit can be determined from the third order polynomial equation:

$$
\begin{aligned}
\rho_6(P_6, T_6) = {} & (1.502e^{-7}P_6 - 1.381e^{-5})T_6^3 \\
& + (-7.677e^{-9}P_6^3 + 1.454e^{-6}P_6^2 - 1.234e^{-4}P_6 \\
& + 5.212e^{-3})T_6^2 \\
& + (1.071e^{-6}P_6^3 - 2.013e^{-4}P_6^2 + 1.719e^{-2}P_6 \\
& - 1.614)T_6 \\
& + (-3.636e^{-5}P_6^3 + 7.784e^{-3}P_6^2 - 0.6337P_6 \\
& + 914.7)\ (Kgm^{-3})
\end{aligned}
$$

Equation 3-47

Subject to:

$$15 \le P_6 \le 50 \ \ (bar)$$

$$90 \le T_6 \le 200 \ \ (°C)$$

And the density at the recuperator hot side exit is calculated from the expression:

$$\begin{aligned}\rho_9(P_9, T_9) = {} & (-5.774e^{-8}P_9 + 1.067e^{-9})T_9^3 \\ & + (4.246e^{-5}P_9 - 6.001e^{-7})T_9^2 \\ & + (-6.027e^{-3}P_9^2 - 1.342e^{-2}P_9 \\ & - 5.571e^{-6})T_9 \\ & + (0.5P_9^2 + 4.015P_9 + 5e^{-4})\ (Kgm^{-3})\end{aligned}$$

Equation 3-48

Subject to:

$$0.1 \le P_9 \le 0.2\ \ (bar)$$

$$60 \le T_9 \le 200\ \ (°\mathrm{C})$$

As stated earlier, the density is needed to calculate the total properties that are used in estimating the pressure ratio, which is a health parameter.

3.1.2.5 Evaporator (Control point 7)

In the evaporator, heat is added to the working fluid. The performance of this component influences the other components in the ORC cycle. As an example, a drop in evaporating pressure translates to a reduction in the main mass flow rate because more heat is needed to superheat the fluid. In addition, the overall efficiency of the working fluid reduces. Computing the thermophysical properties for the model at this control point is quite straightforward because the pressure and temperature have been selected as control variables.

Thus, the enthalpy is calculated from the expression:

$$\begin{aligned}h_7(P_7, T_7) = {} & (-2.845e^{-7}P_7^4 + 2.715e^{-5}P_7^3 - 9.716e^{-4}P_z^2 \\ & + 1.498e^{-2}P_7 - 8.302e^{-2})T_7^2 \\ & + (1.952e^{-4}P_7^4 - 1.857e^{-2}P_7^3 + 0.6636P_7^2 \\ & - 10.21P_7 + 58.72)T_7 \\ & + (-3.354e^{-2}P_7^4 + 3.183P_7^3 - 113.5P_7^2 \\ & + 1742P_7 - 9601) \\ & + (2.593e^{-3}P_7^3 + 0.01825P_7^2 - 0.2989P_7 \\ & + 6.905)\ (KJKg^{-1})\end{aligned}$$

Equation 3-49

Subject to:

$$15 \le P_1 \le 40\ \ (bar)$$

$$200 \le T_1 \le 350\ \ (°\mathrm{C})$$

Upon careful observation of the expression for the enthalpy, one can see that an extra fitting is required. The initial equation without the fit greatly overestimated the enthalpy values. The need for the extra fit is imperative because the accuracy of the thermophysical properties at this control point greatly influences the accuracy of the results obtained for the cycle.

In addition, the density at control point 7 is needed to compute the total-to-total pressure ratio across the turbine and is expressed as:

$$\begin{aligned}\rho_7(P_7,T_7) = {} & (8.366e^{-5}\exp(0.1511P_7) \\ & + 1.164e^{-10}\exp(0.4674P_7))T_7^2 \\ & + (-0.0539\exp(0.1561P_7) \\ & - 4.009e^{-17}\exp(0.9954P_7))T_7 \\ & + (13.8\exp(0.1468P_7) \\ & + 1.032e^{-14}\exp(0.9877P_7)) \\ & + (7.702\sin(0.4607P_7 + 0.3832) \\ & + 4.895\sin(0.2124P_7 + 2.78))\ (Kgm^{-3})\end{aligned}$$

Equation 3-50

Subject to:

$$15 \leq P_1 \leq 40 \ \ (bar)$$

$$200 \leq T_1 \leq 350 \ \ (°\mathrm{C})$$

The extra fitting technique was implemented for this function derived to estimate the density at the evaporator exit; this extra fit can be observed by the extra parameter added at the end of the state equation. The initial equation showed some variation in its prediction for different pressures and the reason for this is the unusual behaviour of toluene at higher pressures. At lower pressures, the specific heat capacity was underestimated whereas it was overestimated at higher pressures.

Finally, the entropy at this control point is calculated using Equation 3-51. The need for the entropy is to be able to estimate the isentropic enthalpy at the turbine exit (control point 8), which in turn is needed to calculate the actual enthalpy.

$$\begin{aligned} s_7(P_7, T_7) = (&-1.928e^{-10}P_7^4 + 1.846e^{-8}P_7^3 - 6.729e^{-7}P_z^2 \\ &+ 1.045e^{-5}P_7 - 6.069e^{-5})T_7^2 \\ &+ (1.315e^{-7}P_7^4 - 1.253e^{-5}P_7^3 + 4.555e^{-4}P_7^2 \\ &- 7.05e^{-3}P_7 + 4.441e^{-2})T_7 \\ &+ (-2.249e^{-5}P_7^4 + 2.129e^{-3}P_7^3 - 7.706e^{-2}P_7^2 \\ &+ 1.179P_7 - 6.411) \\ &+ (1.852e^{-6}P_7^3 - 7.063e^{-5}P_7^2 + 1.593e^{-3}P_7 \\ &- 9.048e^{-3})\ (KJKg^{-1}K^{-1}) \end{aligned}$$ **Equation 3-51**

Subject to:

$$15 \leq P_7 \leq 40\ \ (bar)$$

$$200 \leq T_7 \leq 350\ \ (°\mathrm{C})$$

Also, the equation to calculate the entropy (Equation 3-51) needed to be extra fitted. The initial equation grossly underestimated the entropy.

3.1.2.6 Turbine (Control point 8)

In the turbine, the superheated fluid from the evaporator expands and the result in the generation of useful work. The turbine for the Triogen ORC was designed in-house and performance curves are not available. Thermophysical properties at the turbine exit are deduced from input from low pressure side of the ORC and the power balance of the system. The pressure at the turbine exit is estimated by summing up the condensing pressure and all pressure drops in the heat exchangers between the turbine and storage vessel while the power balance is used to calculate the actual enthalpy.

The pressure at the turbine exit is derived from the expression:

$$P_8 = P_9 + \nabla P_9\ (bar)$$ **Equation 3-52**

Although not used in the computation for the actual enthalpy, the isentropic enthalpy still needs to be calculated in order to estimate the turbine efficiency at every instant that the ORC is in operation. The isentropic enthalpy is easily obtained from the expression:

$$h_{8s}(P_8, s_7) = (1.571P_8 + 2.692)s_7^3 + (-3.571P_8^2 - 2.214P_8 + 121.3)s_7^2 + (275P_8^3 - 419.6P_8^2 + 266.4P_8 + 69.62)s_7 + (89.63P_8^3 - 140.1P_8^2 + 87.81P_8 + 84.51)\ (KJKg^{-1})$$ **Equation 3-53**

Subject to:

$$0.1 \leq P_8 \leq 0.6\ \ (bar)$$

$$0.9 \leq s_7 \leq 1.7\ \ (KJKg^{-1}K^{-1})$$

The power balance of the ORC system is expressed as:

$$\dot{W}_t = PtG + \dot{W}_{mp} + \dot{W}_{pfp} + \dot{W}_{aux} + \underbrace{0.2\dot{W}_t}_{losses}$$ **Equation 3-54**

and

$$\dot{W}_{pfp} + \dot{W}_{aux} \approx 5KW$$

Therefore

$$0.8\dot{W}_t = PtG + \dot{W}_{mp} + 5$$

And finally

$$\dot{W}_t = \frac{PtG + \dot{W}_{mp} + 5}{0.8}$$

Or

$$\dot{m}_2(h_7 - h_8) = \frac{PtG + \dot{m}_2(h_5 - h_3) + 5}{0.8}\ (KW)$$

The actual enthalpy can then be calculated from the expression:

$$h_8 = h_7 - \left[\frac{PtG + \dot{m}_2(h_5 - h_3) + 5}{0.8\dot{m}_2}\right]\ (KJKg^{-1})$$ **Equation 3-55**

Subsequently, the pressure and actual enthalpy can be utilised in defining the corresponding temperature with the rational equation:

$$T_8(P_8, h_8) = \frac{ah_8^2 + bh_8 + c}{h_8 + d} \; (°\text{C})$$ **Equation 3-56**

Where

$$a = -1e^{-2}P_8^2 - 1.7e^{-2}P_8 + 0.3628$$

$$b = -583.3P_8^5 + 1e^3P_8^4 - 620.8P_8^3 + 200P_8^2 + 47.27P_8 + 223.5$$

$$c = 6.667e^4P_8^5 - 1.125e^5P_8^4 + 6.75e^4P_8^3 - 2.238e^4P_8^2 - 8532P_8 - 6.919e^4$$

$$d = 333.3P_8^5 - 541.7P_8^4 + 341.7P_8^3 - 64.58P_8^2 + 105.5P_8 + 183.8$$

Subject to:

$$0.1 \le P_8 \le 0.6 \;\; (bar)$$

$$345 \le h_8 \le 605 \;\; (KJKg^{-1})$$

In addition, the specific heat capacity, which is used in evaluating the thermophysical properties of the recuperator, is calculated from the third order polynomial:

$$\begin{aligned} c_{p_8}(P_8, T_8) = {} & (-2.527e^{-9}P_8^2 - 5.138e^{-9}P_8 - 1.169e^{-9})T_8^3 \\ & + (1.61e^{-6}P_8^2 + 3.8e^{-6}P_8 - 2.184e^{-6})T_8^2 \\ & + (-3.589e^{-4}P_8^2 - 1.018e^{-3}P_8 \\ & + 4.238e^{-3})T_8 \\ & + (1.852e^{-2}P_8^3 + 5.556e^{-3}P_8^2 + 0.1161P_8 \\ & + 1.015) \; (KJKg^{-1}K^{-1}) \end{aligned}$$ **Equation 3-57**

Subject to:

$$0.1 \le P_8 \le 0.6 \;\; (bar)$$

$$100 \le T_8 \le 250 \;\; (°\text{C})$$

Finally, the density of the working fluid at the turbine exit can be calculated from the expression:

$$\begin{aligned}\rho_8(P_8,T_8) = {} & (-2.495e^{-8}P_8^2 - 2.669e^{-8}P_8 - 1.438e^{-10})T_8^3 \\ & + (1.755e^{-5}P_8^2 + 2.649e^{-5}P_8 + 8.82e^{-8})T_8^2 \\ & + (-4.443e^{-3}P_8^2 - 1.232e^{-2}P_8 - 1.9e^{-5})T_8 \\ & + (0.4377P_8^2 + 3.956P_8 + 1.87e^{-3})\ (Kgm^{-3})\end{aligned}$$ **Equation 3-58**

Subject to:

$$0.1 \leq P_8 \leq 0.6 \ \ (bar)$$

$$100 \leq T_8 \leq 250 \ \ (°\mathrm{C})$$

The density is needed to calculate the total-to-total pressure ratio across the turbine and also across the hot side of the recuperator.

In addition, it is equally important to calculate performance indices of the turbine for the active engine. However, a different expression for the enthalpy must be derived as a function of the measured pressure and temperature. This expression is a third order polynomial and is as follows:

$$\begin{aligned}h_8(P_8,T_8) = {} & (4.225e^{-7}P_8 - 9.441e^{-7})T_8^3 \\ & + (-5e^{-5}P_8^2 - 2.85e^{-4}P_8 + 2.174e^{-3})T_8^2 \\ & + (2.5e^{-2}P_8^2 + 7.479e^{-2}P_8 + 1.011)T_8 \\ & + (-1.852P_8^3 + 1.23P_8^2 - 11.86P_8 \\ & + 228.8)\ (KJKg^{-1})\end{aligned}$$ **Equation 3-59**

Subject to:

$$0.1 \leq P_8 \leq 0.6 \ \ (bar)$$

$$100 \leq T_8 \leq 250 \ \ (°\mathrm{C})$$

Validation of these equations are presented in the Appendix and the models derived by coupling these equations are discussed in section 3.2.

3.2 Model development

The primary drivers of the Triogen ORC system are the heat supplied to working fluid in the evaporator and the heat extracted from the condenser. The heat supplied to the working fluid in the evaporator directly influences the behaviour of the working fluid, which dictates the turbine speed and thus the available power while the heat extracted from the working fluid in the condenser influences the cycle minimum pressure, which limits the extractable heat from the evaporator and thus influences the available power. Thus, for a sufficient representation of the active engine ideal state, thermophysical parameters defined by these drivers (or control variables) must match for both the surrogate baseline model and the active engine. Furthermore, the turbine speed is indicative of its operating efficiency and because a single shaft connects the turbine, generator and main pump, the main pump efficiency is also dictated by the shaft speed. Therefore, the condensing and evaporating temperatures, pressures and the shaft speed are the control variables; and these control variables coupled with components design specifications can be utilised in defining the surrogate baseline model for any operating condition. The control variables that must match for both the surrogate baseline model and the active engine and the components design specifications and geometrical parameters utilised in defining the surrogate model are presented in Table 3-2 and Table 3-3 respectively.

Table 3-2: Surrogate model control variables.

Control variables	
Parameter name	**Symbol**
Evaporator outlet (or Turbine inlet) Temperature	T_7
Evaporator outlet Pressure	P_7
Condenser exit Temperature	T_{10}
Condenser exit Pressure	P_{10}
Pre-feed pump rotational speed	N_3
Main pump/Turbine shaft rotational speed	N_5
Available power to grid	PtG

Where the numbers in the subscript represent the control point location along the system cycle.

The purpose of making these parameters match is to ensure that the system cycle analysis, for both the surrogate baseline model and the active engine, is defined at the same operating point. The temperatures and pressures at the evaporator and condenser exit ensures that the exact state of the working fluid is the same as that in the active engine while the pumps speed account for the working fluid mass flow in the system.

Table 3-3: Component design specifications for the surrogate model.

Component design specifications	
Flow parameters	
Parameter name	**Symbol**
Acceleration due to gravity	g
Main pump head coefficient	Ψ_5
Recuperator effectiveness	ε
Recuperator pressure drop (cold side)	∇P_6
Evaporator pressure drop	∇P_7
Recuperator pressure drop (hot side)	∇P_9
Condenser pressure drop	∇P_{10}
Geometry parameters	
Nozzle throat area	A_{71}
Main pump impeller diameter	D_5
Main pump discharge area	d_5

Where the numbers in the subscript represent the control point location along the system cycle and the symbol ∇ represents a decrement.

The component design specifications listed in Table 3-3 must be defined according to manufacturer's specification (or from experience) to ensure for accurate condition parameter deviation for fault detection. Where parameters are unknown, data could be adopted from a dynamically similar component as in literature. The value of acceleration due to gravity does not vary much and is readily available for any geographical location while the manufacturer provides the standard pressure drops in the heat exchangers and the geometrical parameters. The main pump head coefficient however has to be selected by the user based on the ORC design. The main pump head coefficient is essentially a measure of the effectiveness of the pump converting its impeller kinetic energy to pressure head. For this research, analysis of recorded data was done and several values for the head coefficient were tested for the optimum design point before a value was selected.

The primary goal of this research is to develop a method to monitor the Triogen ORC component health parameters like pressure ratios, efficiencies and heat exchanger effectiveness to be able to deduce faults that may arise during operations; therefore, only certain fluid thermophysical properties are necessary. The selected fluid thermophysical properties are the pressure, temperature, enthalpy, density and entropy. At each control point, prior knowledge of two thermophysical properties is available; thus, based on the state postulate, it is possible to define other necessary properties for that control point using the two known properties. As an example of how the properties are calculated at each control point, referring to Figure 3-2 and starting from the storage vessel exit (control point 1), the thermophysical properties known for the working fluid are pressure and temperature (control variables) and the other thermophysical parameters (e.g. enthalpy, entropy) can be determined from these two properties. Even though not used further, calculation of the entropy at the storage vessel exit is necessary to compute the isentropic enthalpy and subsequently the actual enthalpy at the pre-feed pump exit (control point 2). Summarily, two initially known properties at a control point are utilised in deriving the other necessary thermophysical properties at that control point, which in turn are then utilised in determining the desired performance index for that control point; also, some of the thermophysical properties calculated for a control point are necessary in defining the state of its succeeding control point.

3.2.1 Model Assumptions

As with standard models, some assumptions have been made to enable the development of this model with the resources available. It is important to mention at this point that because of the nature of this research, the model is based on a zero-dimensional approach; thus, only the thermophysical properties at the inlet and outlet of each component can be estimated. The assumptions utilised in designing the off-design model are as follows:

1. One-dimensional steady flow in the ORC system. I.e. fluid thermophysical properties are constant across the control points.
2. The total mass flow is a summation of the main mass flow and the lubrication mass flow. The total mass flow goes through the storage vessel and pre-feed pump while the main mass flow goes through the main pump and other components. The main mass flow and lubrication mass flow mixes in the storage vessel.
3. Gravitational terms in the energy balance are negligible.
4. The heat losses from the heat exchangers, turbomachinery components and connecting pipes to the environment are negligible.
5. Friction losses in the pipes connecting components are negligible.
6. The density of the working fluid is constant from the storage vessel up to the main pump exit.
7. The working fluid is in thermodynamic equilibrium across the storage vessel.

8. In the turbine stator (nozzle), the working fluid behaves like an ideal gas and so the ideal gas relations is valid for calculating the critical thermophysical properties.
9. The usable gross work done by the turbine is only 80% of the actual gross work done. I.e. generator, bearing and drive losses account for 20% of the gross work generated by the turbine.

To arrive at the conclusion that the losses amount to 20%, several engine in operation were analysed and an average loss value was determined for application.

3.2.2 Computation algorithm

In this section, the computation algorithm used in describing the ORC cycle for any operating condition is presented. After the matching parameters are determined and the components design specifications are known, the surrogate model can be fully described by calculating desired thermophysical parameters at each of the control points in the ORC cycle whilst taking into account the interrelationships between them. Figure 3-2 shows how the matching parameters together with the design specifications are utilised in computing the required thermophysical properties at each control point. In addition, the arrows connecting each component depicts the interrelationships between components in the Triogen system.

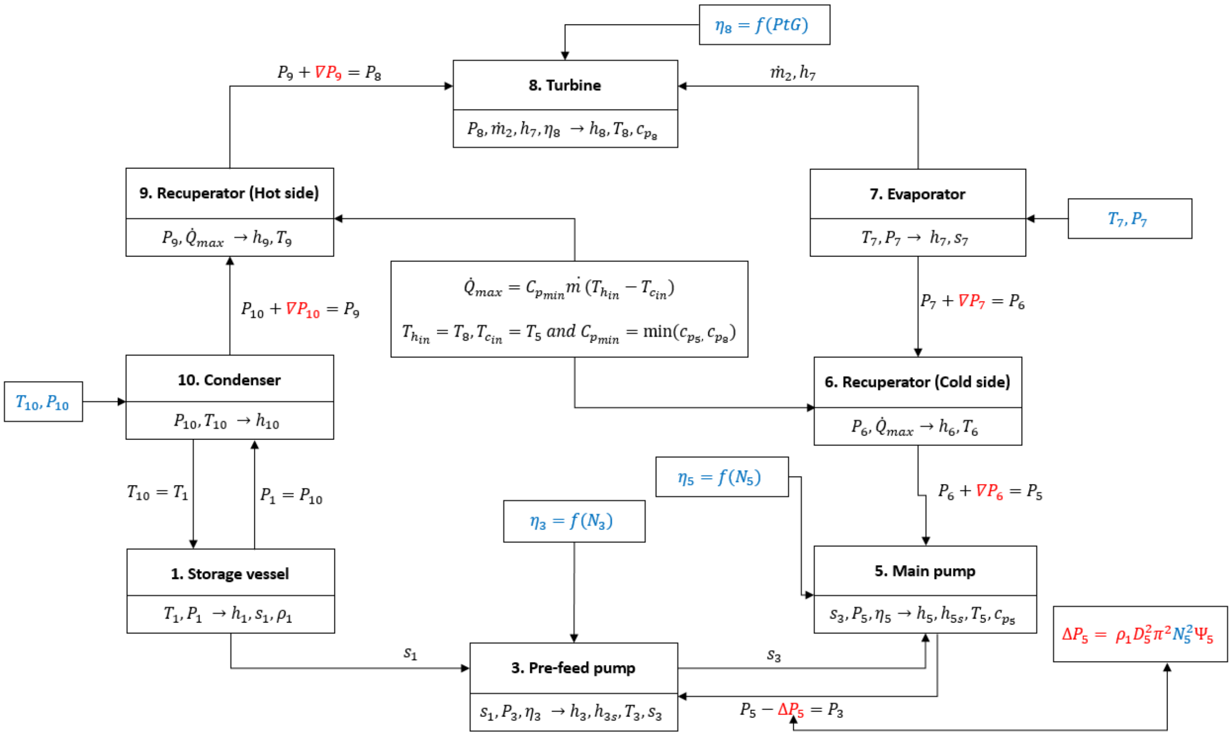

Figure 3-2: Computation algorithm schematic.

Where T is temperature, P is pressure, Ψ is flow coefficient, h is enthalpy, s is entropy, η is efficiency, $\dot{Q}$ is the heat available, Δ represents an increment, ∇ represents a decrement, the subscripts s, in and max represents an isentropic process, inlet and maximum respectively while the numbers in the subscript represents the control point location along the system cycle. The parameters in blue are the control variables while the parameters in red are the component design specifications.

For ease of understanding, general basic relations are utilised in describing the selected algorithm. At the start of this computation, information that defines the operating point for the ORC system (the evaporating and condensing temperature and pressure, pump speeds and available power to grid) and the component design specifications are assumed known.

The first step for this algorithm is to calculate the pressure at each control point. The maximum and minimum pressure, (P_7 and P_{10}) are known so the pressure at the other control points except the pressure at the pre-feed pump exit are easily deducible.

$$P_9 = P_{10} + \nabla P_{10}$$ **Equation 3-60**

$$P_8 = P_9 + \nabla P_9$$

$$P_6 = P_7 + \nabla P_7$$

$$P_5 = P_6 + \nabla P_6$$

$$P_1 = P_{10}$$

The pressure at control points 9, 8, 6 and 5 are simply a summation of the succeeding pressure and the defined pressure drop in the heat exchangers, which have been predefined. In addition, the pressure at control point 1 (storage vessel exit) is assumed to be the same as that at control point 10 (condenser exit) because the working fluid across the storage vessel is assumed to be in thermodynamic equilibrium and thus no work or heat is extracted or added to it. However, the pressure at the pre-feed pump exit is a function of the main pump/turbine shaft rotational speed and the density of the working fluid. The shaft rotational speed is also a control variable but the density of the working fluid must be determined from two known thermophysical properties hence the following step by step analysis.

Starting from control point 1, recall that the working fluid is assumed to be in thermal equilibrium across the storage vessel; therefore, all the thermophysical properties at the condenser exit will remain constant across the storage vessel. However, because only the condensing pressure and temperature are known:

$$P_1 = P_{10}$$ **Equation 3-61**

$$T_1 = T_{10}$$

These two parameters can then be used to compute the other necessary thermophysical parameters at the condenser and storage vessel exit.

$$h_1 = h_{10} = f(P_{10}, T_{10})$$ **Equation 3-62**

$$s_1 = s_{10} = f(P_{10}, T_{10})$$

$$\rho_1 = \rho_{10} = f(P_{10}, T_{10})$$

The calculated entropy and density at control point 1 are utilised as inputs to determine the thermophysical properties at control point 3. First, the pressure at control point 3 is estimated from the difference between the pressure head produced by the main pump and the main pump exit pressure. Ideally, the density to be utilised in computing the pressure head generated by the main pump is that at control point 5 but there is no direct way to compute this density without an iterative procedure. However, in the model assumptions, the density is assumed constant up until the main pump; thus, the selected density is that at control point 1.

$$P_3 = P_5 - \underbrace{(\rho_1 D_5^2 \pi^2 N_5^2 \Psi_5)}_{pressure\ head}$$ **Equation 3-63**

So far, at control point 3, the only known thermophysical property is the pressure but because the main pump is a work addition component, it has an isentropic efficiency. By combining the pressure with the entropy at control point 1, one can calculate the isentropic enthalpy at control point 3. Once the isentropic enthalpy is calculated, the actual enthalpy can be determined using the isentropic efficiency expression for pumps. However, a direct calculation of the isentropic efficiency of the main pump is not readily available, so an expression has been derived from the performance curves provided by the manufacturer.

$$h_{3s} = f(P_3, s_1)$$ **Equation 3-64**

$$h_3 = f(h_1, h_{3s}, P_3, P_1, \rho_1, N_3)$$

Hence, instead of using the isentropic efficiency, a combination of the pressure difference, isentropic enthalpy rise, density and pre-feed pump rotational speed is utilised to determine the enthalpy at control point 3. Now that two actual thermophysical properties are known at control point 3, the other properties can be calculated.

$$T_3 = f(P_3, h_3)$$ **Equation 3-65**

$$s_3 = f(P_3, h_3)$$

The pressure at control point 5 is known and together with the entropy from control point 3, the isentropic enthalpy at control point 5 can be calculated.

$$h_{5s} = f(P_5, s_3)$$ **Equation 3-66**

However, unlike the pre-feed pump, there are no performance maps for the main pump. Therefore, the main pump isentropic efficiency can be estimated by scaling similar pump maps based on the selected pump head coefficient and making some assumptions concerning the main mass flow.

$$\eta_{5s} = f(\dot{m}_2, \gamma, A_{71}, \rho_1, N_5, D_5, d_5)$$ **Equation 3-67**

Where γ, is the ideal specific heat ratio of toluene in the turbine stator (nozzle) and $\dot{m}_2$ is the estimated main mass flow which is estimated from the nozzle critical thermophysical properties. For this research, γ is defined as a function of the thermophysical properties at turbine exit.

$$\dot{m}_2 = f(P_7 T_7, A_{71})$$ **Equation 3-68**

$$\gamma = f(P_8, T_8)$$

Then using the standard isentropic efficiency formula for pumps, the actual enthalpy is determined.

$$h_5 = f(\eta_{5s}, h_5, h_{5s}, h_3)$$ **Equation 3-69**

Subsequently, computation of other thermophysical properties using the pressure and enthalpy at control point 5 is possible.

$$T_5 = f(P_5, h_5)$$ **Equation 3-70**

$$c_{p_5} = f(P_5, h_5)$$

The pressure is the only known property at control point 6. However, control point 6 corresponds to the recuperator cold side exit and a simple heat balance with control point 9 (recuperator hot side exit) will help determine the maximum possible heat exchange in the recuperator.

$$\dot{Q}_{max} = \dot{m}_2 c_{p_{min}} (T_{h_{in}} - T_{c_{in}})$$ **Equation 3-71**

The mass flow rate on both sides of the recuperator is constant and from basic fluid mechanics, it is obvious that the hot fluid will always have the lower specific heat capacity. Therefore, the maximum heat exchange and thus the temperatures at control points 1 and 9 can be calculated keeping in mind the recuperator effectiveness, which is a design parameter.

$$\dot{Q}_{max} = \dot{m}_2 c_{p_8} (T_8 - T_5)$$ **Equation 3-72**

$$\dot{Q} = \varepsilon \dot{Q}_{max}$$

$$T_6 = T_5 + \frac{\dot{Q}}{\dot{m}_2 c_{p_5}}$$

$$T_9 = T_8 - \frac{\dot{Q}}{\dot{m}_2 c_{p_8}}$$

The pressure and temperature can then be used to calculate the other required thermophysical parameters at control point 6.

$$h_6 = f(P_6, T_6)$$ **Equation 3-73**

$$\rho_6 = f(P_6, T_6)$$

The same is valid for control point 9.

$$h_9 = f(P_9, T_9)$$ **Equation 3-74**

$$\rho_9 = f(P_9, T_9)$$

At control point 7, the pressure and temperature are design variables, so calculating the other thermophysical properties is a straightforward procedure.

$$h_7 = f(P_7, T_7)$$ **Equation 3-75**

$$s_7 = f(P_7, T_7)$$

$$\rho_7 = f(P_7, T_7)$$

At control point 8 (turbine outlet), only the pressure is known. However, work is done on the working fluid; therefore, employing the entropy derived from control point 7 will help in determining the isentropic enthalpy at control point 8.

$$h_{8s} = f(P_8, s_7)$$ **Equation 3-76**

In addition, an isentropic efficiency exists for the turbine, because it is a turbomachinery component, and can be utilised in computing the actual enthalpy at control point 8. However, for the turbine, performance maps are not readily available so alternative means must be used in determining the isentropic efficiency. Recall that the available power to grid is also a control variable; thus, an assumption is made for the gross power generated by the turbine and the following expression is derived.

$$\dot{W}_t = PtG + \dot{W}_{mp} + \dot{W}_{pfp} + \dot{W}_{aux} + \underbrace{0.2\dot{W}_t}_{losses}$$ **Equation 3-77**

$$\dot{W}_{pfp} + \dot{W}_{aux} \approx 5KW$$

Where $\dot{W}_t$, PtG, $\dot{W}_{mp}$, $\dot{W}_{pfp}$ and $\dot{W}_{aux}$ are the gross work done by the turbine, available power to grid, main pump work, pre-feed pump work and auxiliary work (process room ventilation and electrical cabinets). Rearranging the expression in Equation 3-77 and filling in the values for the unknown, the gross work done by the turbine can be determined. Hence, the enthalpy at control point 8 is expressed as:

$$h_8 = h_7 - \frac{\dot{W}_t}{\dot{m}_2}$$ **Equation 3-78**

The pressure and enthalpy can then be used in calculating the other thermophysical properties.

$$T_8 = f(P_8, h_8)$$ Equation 3-79

$$\rho_8 = f(P_8, T_8)$$

Finally, a complete description of the ORC cycle is achieved and the desired models can be developed.

3.2.3 Adaptive model

Figure 3-3 shows a schematic representation of the adaptive model developed for the Triogen system. The purpose of an adaptive model is to enable a direct comparison of the true and ideal performance indices of any ORC system. As shown in Figure 3-3, the adaptive model needs the results from the computation algorithm in order to provide the index deviations and in turn, the computation algorithm needs the fluid property model to work to provide the ideal performance indices. In essence, the fluid property model is a key element used in developing the computation algorithm while the computation algorithm is a key element of the adaptive model. As previously mentioned at the introduction to this section, the input for the computation algorithm to calculate the ideal performance indices are the evaporating and condensing thermophysical properties, shaft speeds and available power to grid, which are obtained from sensor readings.

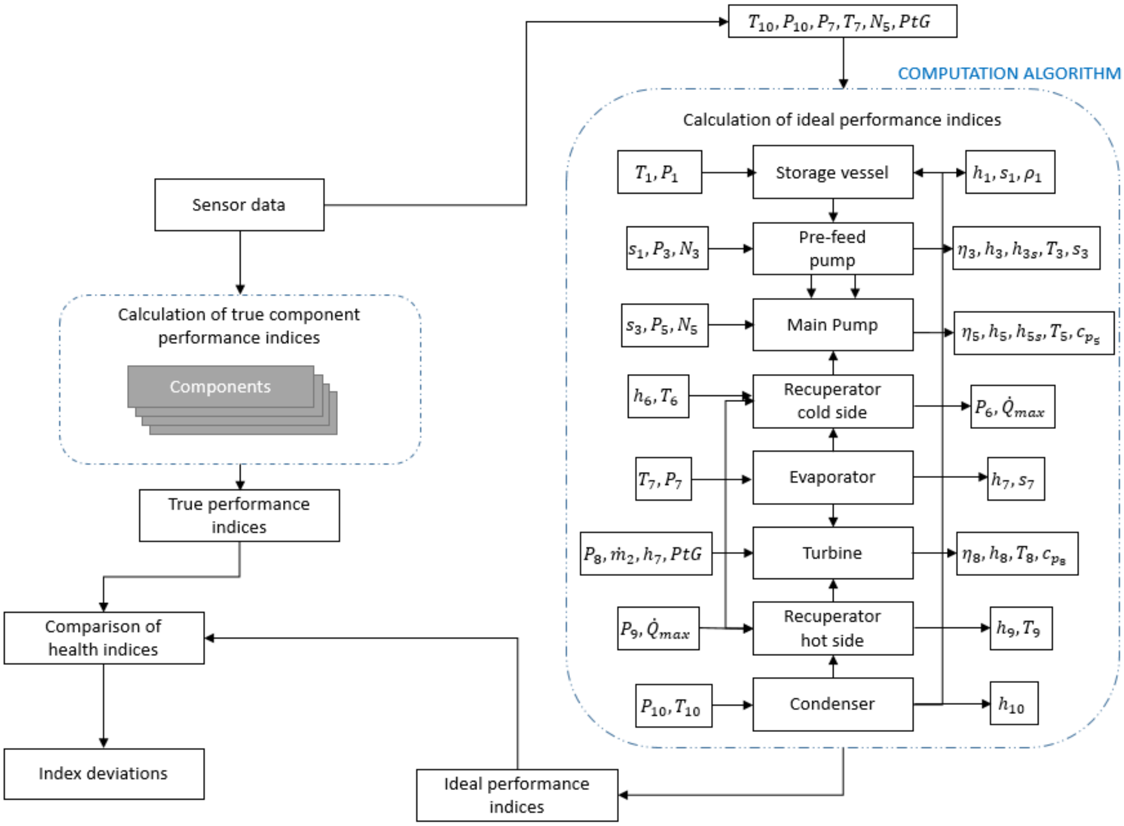

Figure 3-3: Triogen ORC adaptive model.

Setting up the adaptive model is quite straightforward and does not require usage of any third party software because a fluid property model has been developed. The adaptive model has been implemented in Matlab and accepts data in form of .txt files directly from the sensor measurements to compute the true and ideal performance indices, compare them and provide the health status of each component as an output.

3.2.4 Off-design (OD) model

In Figure 3-4, a schematic of the off-design (OD) model developed for the Triogen ORC system is presented. The purpose of developing the OD model is to be able to determine the behaviour of each component in the Triogen system when there is a change in any of the control variables. As previously mentioned, the control variables are the evaporating pressure and temperature (P_7, T_7), condensing pressure and temperature (P_{10}, T_{10}), main pump shaft rotational speed (N_5) and the available power to grid (PtG).

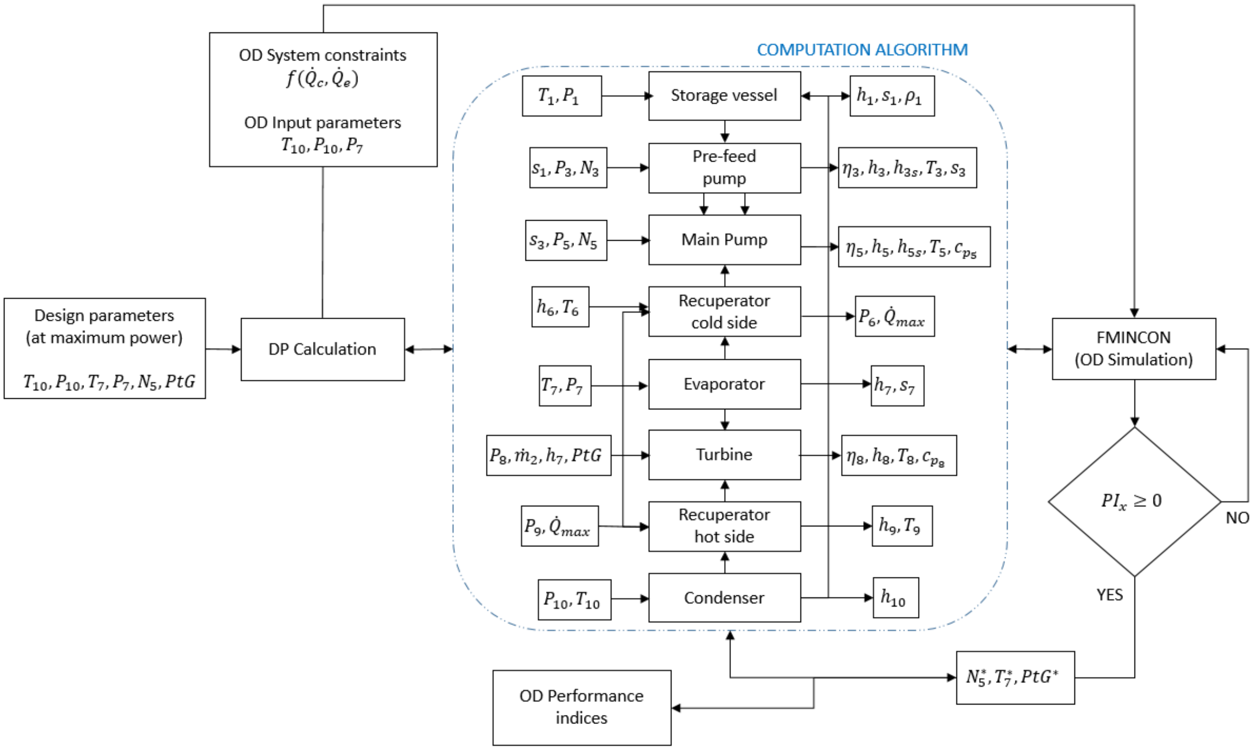

Figure 3-4: Triogen ORC OD model for a deviation in evaporating pressure.

For the OD model, the state of the ORC system can be determined for a deviation in any of the control variables. However, in the Triogen system, the evaporating temperature influences the evaporating pressure and vice versa i.e. a low evaporating temperature corresponds to a low evaporating pressure because the control system has been configured such that the working fluid is superheated before expanding through the turbine. A working fluid with a higher temperature would have more energy and will result in a high shaft rotational speed while a working fluid with a lower temperature has less energy and results in a low shaft rotational speed. Therefore, the evaporating pressure and temperature cannot both be outputs in the

OD simulation; one must be set while the other is determined from the OD simulation to ensure that the system does not correct itself.

The schematic presented in Figure 3-4 is for a deviation in the evaporating temperature with constant design condensing properties and evaporating pressure; the output of the OD simulation is the corresponding shaft speed and available power to grid. First, a design point calculation at maximum power is performed using the defined computation algorithm to size the ORC system. From the design point output, the condensing properties and evaporating pressure are utilised as constant inputs while the available heat in the evaporator and extractable heat in the condenser are set as constraints for the OD simulation. Subsequently, the desired evaporating pressure and the condensing properties are given as inputs to the OD model and the corresponding evaporating temperature, shaft speed and available power to grid are the output of the OD simulation. These output properties of the model are then utilised in calculating the OD operating point for the system. In addition to the constraints, the OD simulation has been setup such that OD output parameters resulting in negative component performance indices (PI_x) values are not considered as part of the solution set.

A Matlab optimisation toolbox “Fmincon” was utilised in developing the OD model. Fmincon minimises the error in a cost function subject to a set of constraints. The Triogen ORC system is a closed system; thus, the cost function selected is the energy balance of the system i.e. the algebraic summation of all the work and heat that influences the system at its boundaries. Furthermore, as mentioned previously, the available heat in the evaporator and extractable heat in the condenser are selected as constraints for the OD simulation to ensure that the optimisation falls within realistic bounds. In addition, additional constraints are set as a function of the thermophysical properties calculated within the optimisation algorithm. The optimisation problem for the schematic in Figure 3-4 is of the form:

$$minimize\ J = \left|\sum E_{system}\right| = \left|\dot{Q}_e - \dot{W}_t - \dot{W}_{mp} - \dot{W}_{pfp} - \dot{Q}_c\right| \qquad \textbf{Equation 3-80}$$

Subject to:

$$T_7 \geq T_7^v$$

$$T_8 \geq T_8^v$$

$$\dot{m}_1 > \dot{m}_2 > 0$$

$$\dot{Q}_e = \dot{Q}_e^{DP}$$

$$\dot{Q}_c = \dot{Q}_c^{DP}$$

Where $\dot{Q}_e$ is the heat input to the evaporator, $\dot{W}_t$ is the work extracted by the turbine, $\dot{W}_{mp}$ is the work supplied to the main pump, $\dot{W}_{pfp}$ is the work supplied to the pre-feed pump and $\dot{Q}_c$ is the heat extracted in the condenser. T_7 is the evaporating temperature, T_8 is the turbine exit temperature, $\dot{m}_1$ and $\dot{m}_2$ are the total and main mass flows and the superscripts v and DP represent saturated vapour state and the design point value respectively. Furthermore, the cost function has been defined as an absolute value to ensure that Fmincon does not return a negative value.

For the optimization, the design vector and their bounds are shown in Table 3-4. The bounds for each design variable except the were selected to cover the normal operating range for each of the affected component.

Table 3-4: Design vector for Fmincon optimization.

Design variable	Upper bound	Lower bound
P_7	$40\ [bar]$	$0\ [bar]$
T_7	$350\ [℃]$	$0\ ℃$
P_{10}	$2\ [bar]$	$0.1\ [bar]$
T_{10}	$80\ [℃]$	$40\ [℃]$
N_5	$450\ [{}^{rev}/_{s}]$	$230\ [{}^{rev}/_{s}]$
PtG	$300\ [KW]$	$50\ [KW]$

In this research, four cases were investigated for the OD simulation. The first three cases assess the OD behaviour of the system at constant condensing properties while the last case investigates the behaviour of the system at constant evaporating properties. It was observed that the degree of freedom of the optimization influences the accuracy of the predicted OD operating point i.e. setting up the OD simulation with more than two optimization outputs would result in different results which depend on the starting point of the optimisation. Therefore, for the first three cases, the evaporating pressure, evaporating temperature and main pump shaft rotational speed are kept constant respectively, in addition to the condensing properties, to ensure that the system stays within realistic limits.

In the first case, the condensing properties and evaporating pressure are kept constant and the main pump shaft speed is varied to observe the behaviour of the available power and evaporating temperature. Figure 3-5 and Figure 3-6 shows the available power and evaporating temperature OD behaviour as a function of the main pump shaft rotational speed respectively.

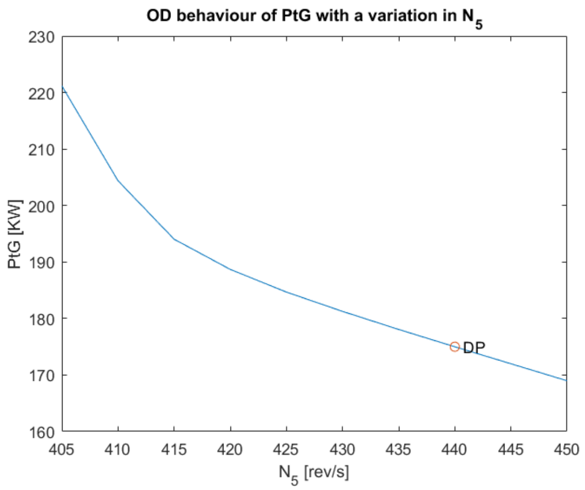

Figure 3-5: OD trend of available power to grid at constant condensing properties and evaporating pressure.

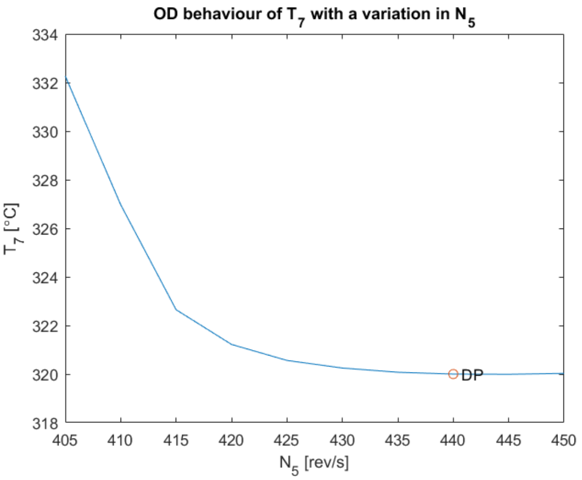

3

Figure 3-6: OD trend of evaporating temperature at constant condensing properties and evaporating pressure.

It can be seen from Figure 3-5 that a higher available power can be obtained if the shaft rotational speed is decreased; however, the limitation to this is a high pressure ratio requirement from the pre-feed pump thus putting a strain on it.

In the second case, the condensing properties and evaporating temperature are kept constant and the main pump shaft speed is varied to observe the behaviour of the available power and evaporating pressure. Figure 3-7 and Figure 3-8 shows the evaporating pressure and available power OD behaviour as a function of the main pump shaft rotational speed respectively.

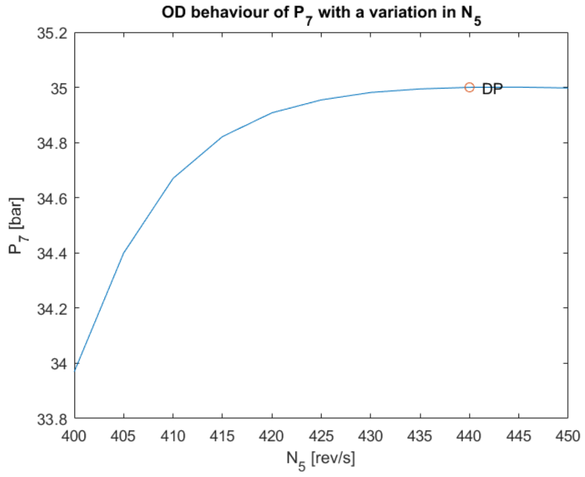

Figure 3-7: OD trend of evaporating pressure at constant condensing properties and evaporating temperature.

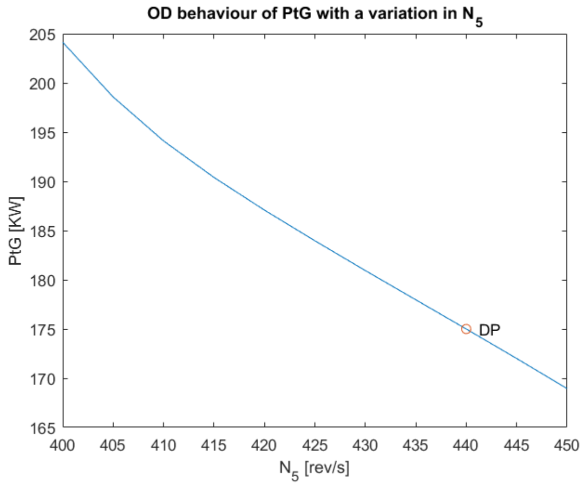

Figure 3-8: OD trend of available power to grid at constant condensing properties and evaporating temperature.

In this case, it can be seen that an increase in the shaft rotational speed will result in a reduction in the available power to grid whereas a decrease would result in an increase in the available power. However, the pre-feed pump pressure ratio requirement is also a limiting factor.

For the third case, the condensing properties and main pump shaft rotational speed are kept constant and the evaporating temperature is varied to observe the behaviour of the available power and evaporating pressure. Figure 3-9 and Figure 3-10 shows the available power and evaporating pressure OD behaviour as a function of the evaporating temperature respectively.

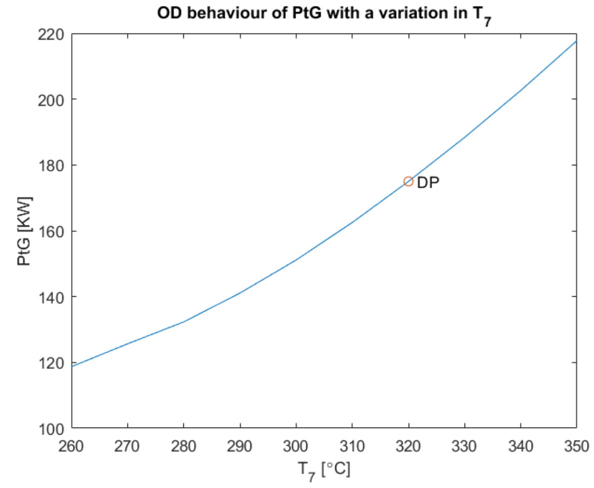

Figure 3-9: OD trend of available power to grid at constant condensing properties and shaft speed.

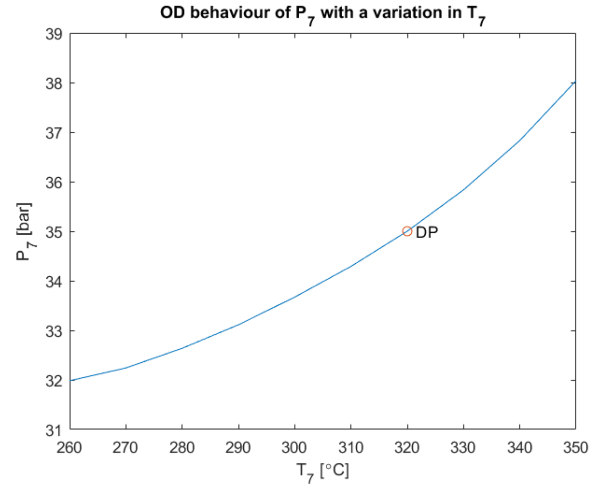

Figure 3-10: OD trend of evaporating pressure at constant condensing properties and shaft speed.

Increasing the evaporating temperature will result in an increase in both the available power to grid and evaporating pressure; however, as in previous cases, the limiting factor is the pressure requirement of the pre-feed pump.

For the last case considered, the evaporating properties and main pump shaft rotational speed are kept constant and the condensing temperature is varied to observe the behaviour of the available power and condensing pressure. Figure 3-11 and Figure 3-12 shows the available power and condensing pressure OD behaviour as a function of the condensing temperature respectively.

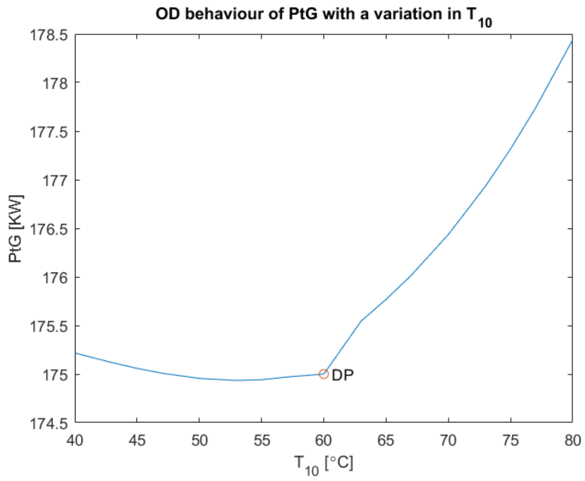

Figure 3-11: OD trend of available power to grid at constant evaporating properties and shaft speed.

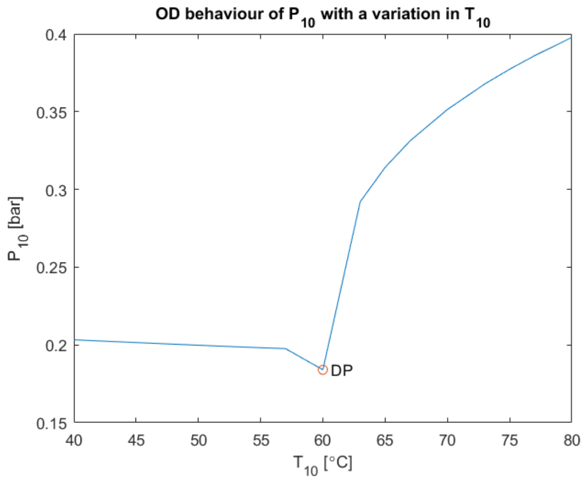

Figure 3-12: OD trend of condensing pressure at constant evaporating properties and shaft speed.

Even though increasing the condensing temperature increases the available power to grid, the main limiting factor to this case is the danger of the working fluid changing into vapour state. A further increase in the condensing temperature will result in an increase in the pressure and cause the working fluid to vaporize. For the Triogen ORC system, the working fluid must remain in a liquid state whilst going through the pumps to prevent severe damage.

4 Component health evaluation

In the previous chapter, the steps taken to identify and derive functions for calculating the thermophysical properties needed in computing key performance indices, defining ruleset combinations for possible faults and prescribing maintenance solutions for each component have been discussed. As mentioned in the previous section, some thermophysical parameters selected as control variables for the Triogen ORC system coupled with available component design specifications are utilised in defining the surrogate baseline model. These thermophysical parameters and the component design specifications are utilised in computing the remaining thermophysical properties of toluene needed to calculate the performance indices for the surrogate baseline model at each of the control points in the ORC cycle. While the surrogate model utilizes the selected control variables and design specifications, the active engine utilizes thermophysical property values obtained from sensor measurements to obtain the necessary thermophysical parameters (e.g. enthalpy, density) that define the performance indices.

The idea behind the proposed methodology is to calculate certain thermophysical properties, at each control point, for both the surrogate baseline model and the active engine to enable comparison of both performance indices and thermophysical property trends; and from these comparisons, the health status of the components can be determined. Section 4.1 describes the fault mechanisms considered for this research, section 4.2 presents the performance indices selected based on the faults considered while section 4.3 presents the methodology employed in developing the rulesets for fault detection in the Triogen ORC system.

4.1 Fault Mechanisms

To successfully isolate and diagnose component faults, the right ruleset (or combination of component performance indices deviation and/or thermophysical properties) must point to the right component fault. Due to the complex nature of the Triogen system and thermodynamic systems in general, fault identification will be limited to primary level identification. Essentially, the types of failure to be considered for each component in this research are cracks and leaks, component material degradation and flow path blockage. Sub-sections 4.1.1 to 4.1.3 provides an explanation for what these faults represent for this research.

4.1.1 Cracks and leaks

In this research, the fault mechanism cracks and leaks generally refers to faults like seal leaks in turbomachinery components and cracks in the heat exchangers. The reason for grouping these failure mechanisms under this particular fault is that exact identification of most of the fault mechanisms necessitates visual inspection. However, this particular fault mechanism can be identified by observing the trend of the total-to-total pressure ratio across the component of interest. For example, the storage vessel is assumed to be a neutral component and not have any influence on the state of the working fluid; i.e. no heat or work is transferred to or extracted from the working fluid in the storage vessel. Therefore, the ideal total-to-total pressure ratio across the storage vessel of the surrogate baseline model is unity and a negative index deviation indicates an internal leak (storage vessel total-to-total pressure ratio of active engine greater than unity) while a positive index deviation indicates an external leak (storage vessel total-to-total pressure ratio of the active engine less than unity).

4.1.2 Component material degradation

Component material degradation encompasses failure mechanisms like corrosion, erosion and breakage. The idea behind this fault group is that these failure mechanisms in one way or the other results in component material removal. In addition, these failure mechanisms are grouped together because they have a major impact component surface and in turn influence the dynamic characteristics of the working fluid, by increasing the fluid flow cross sectional area, and the performance of the component. Performance trends of the total-to-total pressure ratio and the efficiency (for turbomachinery components) or effectiveness (for heat exchangers) are good indicators of this fault mechanism. For example, a decrease in only the total-to-total pressure ratio across the main pump would naturally lead one to imply leakage while only a decrease in the pump isentropic efficiency could imply pump degradation. However, it is possible that there is a simultaneous deterioration in both health indices; in such a case, monitoring the power consumed by the main pump would help in correctly identifying the root cause.

4.1.3 Flow path blockage

Failure mechanisms like clogging and fouling fall under this category. This fault mechanism is the opposite of component material degradation in the sense that flow path blockage leads to a reduction in fluid flow cross sectional area. However, performance trends used in detecting component material degradation are also applicable in this case. The main difference being that intuitively, performance trends will behave opposite to that of component material degradation. For example, without loss of generality, the total-to-total pressure ratio across a component in this research is defined as the ratio of the total outlet pressure to the total inlet pressure. Therefore, a lower than expected total-to-total pressure ratio across a heat exchanger would signify component material degradation because the fluid flow cross sectional area has been increased whereas, a higher than expected total-to-total pressure ratio would signify flow path blockage because the fluid flow cross sectional area has been increased.

4.2 Performance indices

Ideally, it is better to select each performance index in a way that it adequately describes the component(s) which it is applied to so that the true condition of each component can be easily determined. Dimensional analysis of turbomachinery components describes turbomachinery performance using non-dimensional groups [65], which include the corrected mass flow, corrected rotor speed, pressure ratio, isentropic, or polytropic efficiency, ratio of specific heats and Reynolds number. However, for the Triogen ORC, only certain obtainable non-dimensional properties have been selected as performance indices for the components. These non-dimensional properties are the total-to-total pressure ratio, isentropic efficiency, heat exchanger effectiveness and mass flow rate.

The storage vessel is assumed to be a neutral component and not have any influence on the state of the working fluid; i.e. no heat or work is transferred to or extracted from the working fluid in the storage vessel. Therefore, total-to-total pressure ratio is a sufficient health parameter. The pumps on the other hand are subject to any of the three fault mechanisms described in section 4.1; therefore, as well as the total-to-total pressure ratio, isentropic efficiencies must also be monitored. The heat exchangers are also prone to any of the three fault mechanisms but is not a work-transferring device. Therefore, the heat exchanger effectiveness has been selected as a health indicator instead.

The total-to-total pressure ratio across any component is expressed as the ratio of the total pressure of the working fluid exiting the storage vessel to that entering it. i.e.

$$PR_x = \frac{P_{t_n}}{P_{t_{n-1}}} \; (-) \qquad \textbf{Equation 4-1}$$

Where PR_x is the pressure ratio across a component x, P_{t_n} is the total pressure at a control point n while $P_{t_{n-1}}$ is the total pressure ratio at the control point that precedes n.

However, the thermophysical functions that have been derived are to calculate the static pressure; as a result, the pressure ratio has to be re-written to account for the total pressure by utilizing the velocity and density of the working fluid. The total pressure ratio can be obtained by summing the dynamic and static pressures and is obtained as follows:

The total pressure of a fluid is expressed as:

$$P_t = P_s + \frac{1}{2}\rho V^2 \; (Nm^{-2}) \qquad \textbf{Equation 4-2}$$

Where P_t is the total pressure, P_s is the static pressure, ρ is the density and V is the velocity of the fluid.

Expressing the velocity as a function of the mass flow yields:

$$V = \frac{\dot{m}}{\rho A} \; (ms^{-1}) \qquad \textbf{Equation 4-3}$$

Where $\dot{m}$ is the mass flow rate, ρ is the density and A is the flow area.

Inserting Equation 4-3 into Equation 4-2 yields the expression for the total-to-total pressure ratio as:

$$PR_x = \frac{P_{t_n} e^5 + \frac{1}{2}\left(\frac{\dot{m}_n}{A_n}\right)^2 \frac{1}{\rho_n}}{P_{t_{n-1}} e^5 + \frac{1}{2}\left(\frac{\dot{m}_{n-1}}{A_{n-1}}\right)^2 \frac{1}{\rho_{n-1}}}$$

Where the factor e^5 is included to convert the static pressure from the unit of bar to Nm^{-2}.

The isentropic efficiency is expressed as:

$$\eta_{ns} = \frac{h_{ns} - h_{n-1}}{h_n - h_{n-1}}$$ **Equation 4-4**

Where η_{ns} is the isentropic efficiency, h_{ns} is the isentropic enthalpy and h_n is the actual enthalpy at a control point n while h_{n-1} is the actual enthalpy at the control point that precedes n.

In addition, the volumetric efficiency is a parameter of interest. The volumetric efficiency is the ratio of the actual flow rate to the theoretically expected flow rate void of losses. For this research, the volumetric efficiency is expressed as:

$$\eta_v = \frac{\dot{V}_{engine}}{\dot{V}_{model}}$$ **Equation 4-5**

The resulting value is a comparison on its own and ranges from 0 to 1 and is a measure of the severity of leakage in the pre-feed pump. For the pre-feed pump, this health index is easily determined as the ratio of the actual engine flow rate to that of the model by employing the equations derived from performance maps. However, the same cannot be done for the main pump because of the absence of performance curves.

The heat exchanger effectiveness is defined as:

$$\varepsilon_n = \frac{T_{hi} - T_{ho}}{T_{hi} - T_{ci}}$$ **Equation 4-6**

Where ε_n is the heat exchanger effectiveness, T_{hi} is the hot fluid inlet temperature T_{ho} is the hot fluid outlet temperature and T_{ci} is the cold fluid inlet temperature at a control point n.

Equations for calculating the total and main mass flow rates have been provided during the derivation of the state equations. However, the lubrication mass flow rate is of great importance as quick identification of a drop could save the entire ORC system from severe damage. As previously mentioned, a single shaft connects the turbine to the main pump also acts as the stator for the turbo-generator. For smooth running of the generator and system in general, it is imperative that the enough lubrication is available to the bearings to prevent direct contact with the shaft. When there is contact between the shaft and bearings, the bearing temperature increases and the shaft is damaged due to friction. In addition, an inconsistent supply of lubrication fluid to the bearings, due to clogged lubrication channels or irregular fluctuating system conditions, would induce vibration in the shaft and consequently in the turbine; thus resulting in catastrophic damage. Thus, to prevent this occurrence, the mass flow supplied for lubrication and cooling should be kept at an acceptable level with respect to the operating condition of the ORC. This mass flow rate is defined as:

$$\dot{m}_{lub} = \dot{m}_1 - \dot{m}_2$$ **Equation 4-7**

Where $\dot{m}_{lub}$ is called the lubrication mass flow rate, $\dot{m}_1$ is the total mass flow rate and $\dot{m}_2$ is the main mass flow rate in the ORC system.

In conclusion, the index deviation of the health indices are calculated as follows:

$$\%PI = \frac{PI_{measured} - PI_{surrogate}}{PI_{surrogate}}$$ **Equation 4-8**

Where $PI_{measured}$ is the measured performance index i.e. performance parameter of the engine being assessed, $PI_{surrogate}$ is the surrogate model performance index prediction and $\%PI$ is the percentage deviation which gives an indication of the deterioration severity for a component.

4.3 Ruleset definition

Observing component performance indices alone might not give a true diagnosis in some cases hence the need for rulesets; also, because of the complex interrelationships between the systems components, obtaining the right ruleset for each failure mechanism necessitates the construction of a fault table to be able to make a clear distinction between faults with overlapping patterns. It is intended that this fault table be used in identifying possible health and thermophysical parameter set for identifying specific ORC faults. The fault table will be generated by varying selected health parameters in order to observe the system response to change. To achieve this, first the surrogate model has to be set to a reference operating point, in this case maximum power to grid, and subsequently simulations can be run whilst varying different health parameters.

For each of the components, all the health parameters selected for it will be varied simultaneously i.e. where one or more health parameter has been selected to analyse the condition of a component, all parameters shall be varied, whilst maintaining the design values for the other components, and a performance map will be created in the process. The values listed in Table 4-1 have been utilised for the simulation and the results obtained for each component with the accompanying trend plots are presented from subsections 4.3.1 to 4.3.7.

Table 4-1: Input values for component fault simulation.

Control variable	Design value
T_{FI}	490 ℃
T_{FO}	180 ℃
T_{CI}	40 ℃
T_{CO}	55 ℃
T_7	320 ℃
P_7	35 bar
T_{10}	60 ℃
P_{10}	0.2 bar
N_3	1450 rpm
N_5	450 rev/s
PtG	175 KW
Ψ_5	0.65
ε_R	0.89
∇P_6	0 bar
∇P_7	0 bar
∇P_9	0 bar
∇P_{10}	0 bar

Where T_{FI} and T_{FO} are the flue gas inlet and outlet temperatures, T_{CI} and T_{CO} are the coolant inlet and outlet temperatures and ε_R is the recuperator effectiveness.

These values presented in Table 4-1 are the standard design values for the ORC system at maximum power. To simulate each component fault, the state equations that have been developed and presented in sub-section 3.1.2 are modified such that a desired outcome is achieved. For the fault simulations, the pressure ratio and component efficiencies (or effectiveness for heat exchangers) are varied. To vary the pressure ratio of a component, a multiplying factor, which takes a value between 0 and 1, is added to the exit pressure relation for that component. While in varying the efficiencies (or effectiveness) the equation to calculate the actual enthalpy (or temperature) at the exit of the component under consideration is re-written as a function of the efficiency (or effectiveness) of that component. From sub-sections 4.3.1 to 4.3.7, the results obtained for the simulations are presented and discussed.

4.3.1 Storage vessel

For the storage vessel, only the fault mechanism cracks and leaks can occur because the working fluid is assumed to be in thermal equilibrium across it i.e. neither work or heat is added to or extracted from the working fluid going through it. Hence, only the variation of the total-to-total pressure ratio is necessary. For the system design in this case, all design parameters listed in Table 4-1 are kept constant. In addition, the pressure relation at control point 1, which is the storage vessel exit, is re-written as:

$$P_1 = P_{10}PR_1$$

Equation 4-9

Where PR_1 is the pressure ratio across the storage vessel and assumes a value from 0 to 1 for the simulation. A value of zero is in essence shutdown while one represents normal operating condition of the ORC system. Plots obtained for the simulation are presented from Figure 4-1 to Figure 4-7.

The next component after the storage vessel is the pre-feed pump and ideally, the effects of a fault occurring in the storage vessel should be visible on the health parameters of the pre-feed pump.

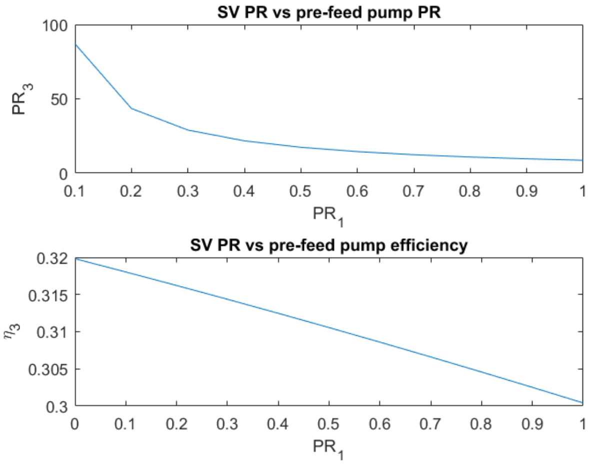

Figure 4-1: Pre-feed pump health indices trend for storage vessel deterioration.

From the Figure 4-1, it can be seen that as the pressure ratio across the storage vessel deteriorates, the efficiency and pressure ratio across the pre-feed pump become favourable. This effect is expected since the efficiency of the pre-feed pump is a function of the enthalpy at the storage vessel exit; with all other components operating effectively at the design condition, a lower temperature and pressure would yield a lower enthalpy at the storage vessel exit thus resulting in a higher efficiency and pressure ratio of the pre-feed pump. However, careful observation of Figure 4-1 shows that the improvement in the pre-feed pump efficiency is only minimal and that the more visible effect is in the pressure ratio; therefore, the pressure ratio would be a better indicator of a fault in the storage vessel. A good way to confirm this inference is to inspect the power consumed by the pre-feed pump. Figure 4-2 shows the behaviour of the power consumed by the pre-feed pump as the pressure ratio across the storage vessel changes.

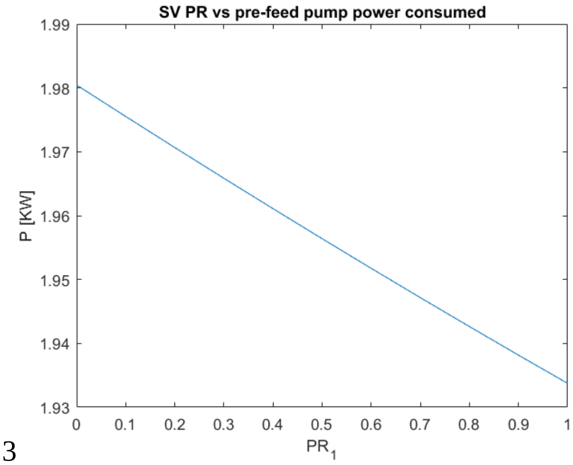

3.3

Figure 4-2: Pre-feed pump power trend for storage vessel deterioration.

Referring to Figure 4-2, almost 45Watts of extra power is needed when the entire pressure to the fluid is lost. I.e. there exist a negative linear relationship between the power required by the pre-feed pump and the pressure ratio across the storage vessel.

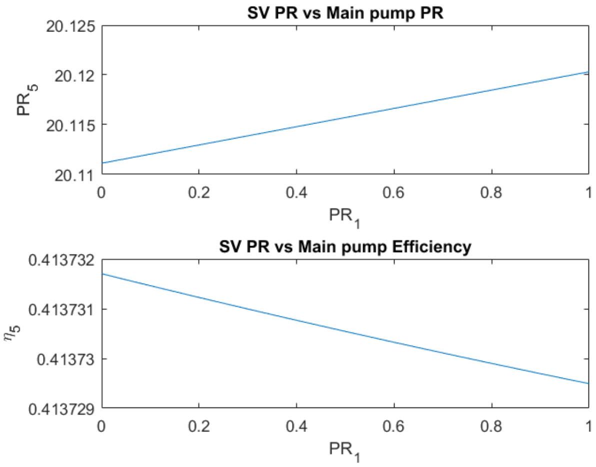

Figure 4-3: Main pump health indices trend for storage vessel deterioration.

The next component after the pre-feed pump is the main pump. Referring to Figure 4-3, the effects of the pressure drop across the storage vessel on the main pump is negligible. As can be seen, the pressure ratio across the main pump and the efficiency do not vary much. Furthermore, the efficiency appreciates by about 0.0001% while the pressure ratio deteriorates by about 0.02% as the pressure ratio across the storage vessel decreases.

The pressure drop across the storage vessel has no effect on the pressure ratio across the cold side of the recuperator nor the effectiveness; thus, it has no effect on the hot side. The reason for this is that the effectiveness of the recuperator has been set as a design variable from the start.

Also for the evaporator, there is minimal effect as can be seen in Figure 4-4. There is no change in the pressure ratio across the evaporator and the total change in evaporator effectiveness is less than 1%.

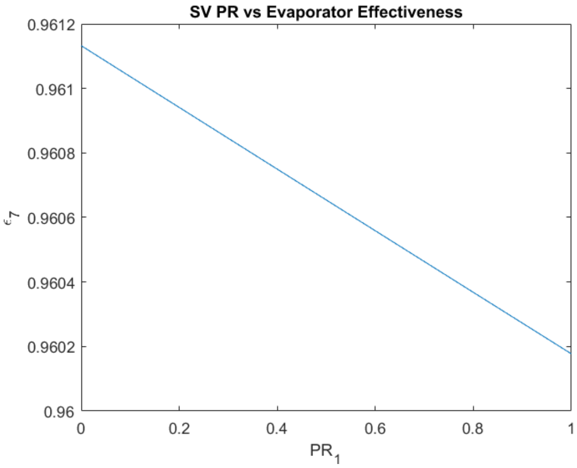

Figure 4-4: Evaporator health index trend for storage vessel deterioration.

However, there is a decrease in the turbine efficiency and a slight increase in the pressure ratio across the turbine as the pressure ratio across the storage vessel decreases (Figure 4-5). Though negligible, this reversed behaviour in the turbine is because of the definition of the pressure ratio for this research. The turbine being a work-extracting component always has a lower pressure at its exit unlike the pumps, which are work addition components.

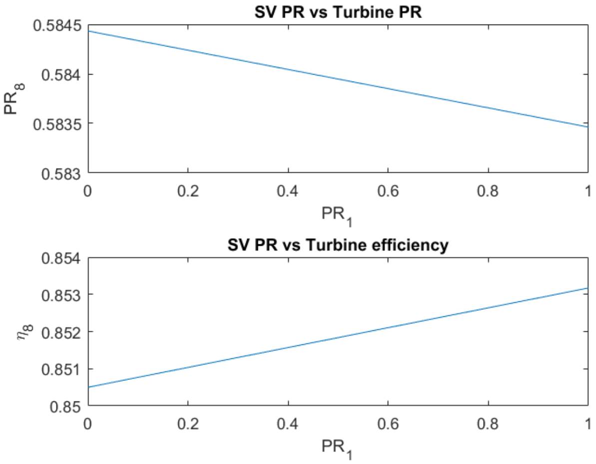

Figure 4-5: Turbine health indices trend for storage vessel deterioration.

For the condenser, the effectiveness also increases as the pressure ratio across the storage vessel reduces (Figure 4-6). This increase in effectiveness in total is also negligible and less than 1%.

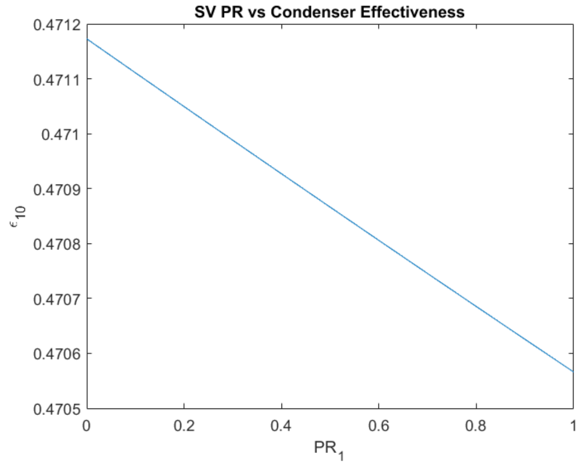

Figure 4-6: Condenser health index trend for storage vessel deterioration.

A look at the overall system performance (Figure 4-7) shows that a decrease in the pressure ratio across the storage vessel also has very little effect on the thermal and overall efficiency of the ORC system.

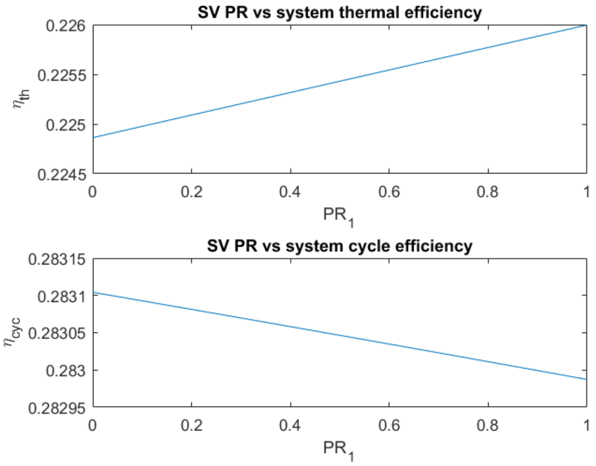

Figure 4-7: Overall system performance trend for storage vessel deterioration.

In summary, a decrease in the pressure ratio across the storage vessel has no significant effect on the other components in the ORC except the pre-feed pump and thus does not adversely affect the overall system performance. However, a reduction in the pressure ratio across the storage vessel corresponds to the case of an external leak. Furthermore, in the Triogen system, a toluene concentration sensor (designed to monitor the system control volume) detects external leaks and shuts off the system when a set concentration limit is breached. Nevertheless, if the toluene concentration sensor fails, monitoring the pressure ratio across the storage vessel is a fast and efficient way to detect this leak. Thus, the rule set for detecting external leaks in the storage vessel should also contain the pre-feed pump power and pressure ratio across the pre-feed pump since the pre-feed pump tries to compensate for this pressure loss by using more power to generate more pressure head.

4.3.2 Pre-feed pump

In the pre-feed pump, any of the three selected fault mechanism can occur. Thus, both the total-to-total pressure ratio and the main-pump isentropic efficiency will be varied in order simulate pump degradation. Here, the state equation for calculating the pre-feed pump exit pressure is also modified in the same manner as that of the storage vessel.

$$P_3 = (P_5 - (\rho_1 D_5^2 \pi^2 N_5^2 \Psi_5))PR_3 \quad \text{Equation 4-10}$$

Where PR_3 is the pressure ratio across the pre-feed pump and assumes a value from 0 to 1 for the simulation. In addition, the standard equation to compute the isentropic efficiency of a pump is utilised in estimating the enthalpy at the exit so that it is possible to vary the pre-feed pump isentropic efficiency.

$$h_3 = h_1 + \frac{h_{3s} - h_1}{\eta_{3s}} \quad \text{Equation 4-11}$$

Before the pre-feed pump is the storage vessel and in this case, because the storage vessel precedes the pre-feed pump, there is no effect on it when there is deterioration in the pre-feed pump.

The next component after the pre-feed pump is the main pump. Like in the case of the storage vessel where the succeeding component is affected, when the pressure ratio across the pre-feed pump decreases, there is a rise in the pressure ratio across the main pump. However, there is not much change in the main pump isentropic efficiency regardless of the pressure or isentropic efficiency drop across the pre-feed pump. Figure 4-8 shows the main pump pressure ratio and efficiency variations with changing pressure ratio.

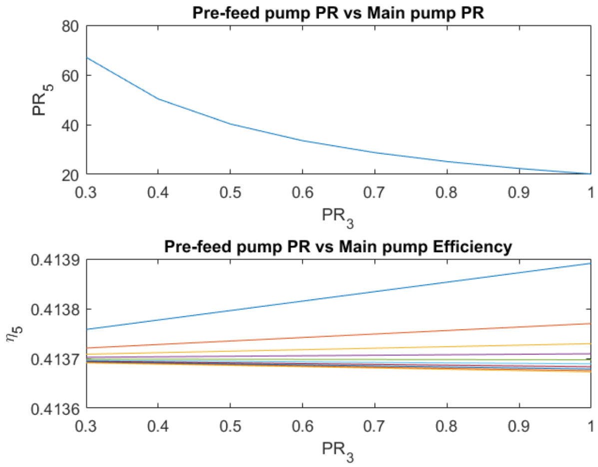

Figure 4-8: Main pump health indices trend for pre-feed pump deterioration.

For the simulation, varying the efficiency of the pre-feed pump did not have any significant effect on the main pump efficiency and no effect at all on the pressure ratio. Nonetheless, it is interesting to observe that at lower pre-feed pump efficiencies, the efficiency of the main pump decreases with decreasing pre-feed pump pressure ratio but increases with decreasing pre-feed pump pressure ratio at much higher pre-feed pump isentropic efficiencies. The reason for this is that the main job of the pre-feed pump is to provide enough suction head to the main pump irrespective of the efficiency.

After the main pump is the cold side of the recuperator. The recuperator effectiveness is a component design value and thus is unchanged in the simulation; therefore, the effectiveness and the pressure ratios across the hot and cold side are unaffected.

Next is the evaporator. The pressure drop across the pre-feed pump has no effect on the pressure drop across the evaporator because the recuperator determines the inlet pressure and the outlet pressure is a set design value. However, the pressure drop across the pre-feed pump has very little effect on the evaporator effectiveness as can be seen in Figure 4-9. A deterioration in the pressure ratio across the pre-feed pump results in a slight deterioration in the evaporator effectiveness.

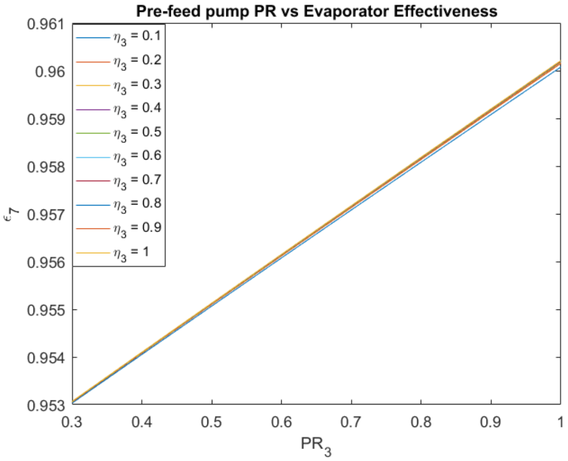

Figure 4-9: Evaporator health index trend for pre-feed pump deterioration.

After the evaporator is the turbine. Referring to Figure 4-10, there is also a negligible deviation in the isentropic efficiency and pressure ratio across the turbine. The plot also shows that regardless of the isentropic efficiency of the pre-feed pump, the same effect occurs in the turbine for a deterioration in the pressure ratio across the pre-feed pump. Though negligible, a deterioration in the pressure ratio across the pre-feed pump results in a deterioration in the pressure ratio across the turbine and an appreciation in the turbine isentropic efficiency.

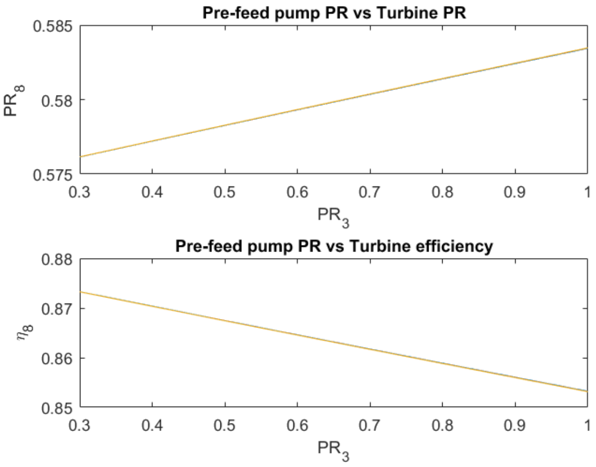

Figure 4-10: Turbine health index trend for pre-feed pump deterioration.

In the condenser, a reduction in the pressure ratio across the pre-feed pump or a change in the isentropic efficiency results in a deterioration of less than 4% for the condenser effectiveness. The pressure ratio across the condenser is unaffected by a change in the pre-feed pump pressure ratio but the condenser effectiveness is, albeit negligible (Figure 4-11). Also noteworthy is that lower pre-feed pump isentropic efficiencies results in a larger reduction in compressor effectiveness.

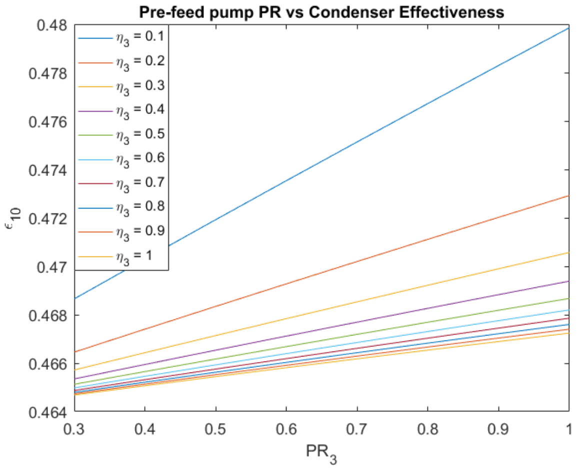

Figure 4-11: Condenser health index trend for pre-feed pump deterioration.

Figure 4-12 shows that the effect of a deterioration in the pre-feed pump also has a negligible effect on the overall system performance. Although negligible, a decrease in the pressure ratio across the pre-feed pump causes an increase in the system thermal efficiency regardless of pre-feed pump efficiency. In addition, a decrease in the pressure ratio across the pre-feed pump results in a decrease in cycle efficiency at higher pre-feed pump efficiencies and an increase in cycle efficiency at lower pre-feed pump isentropic efficiencies.

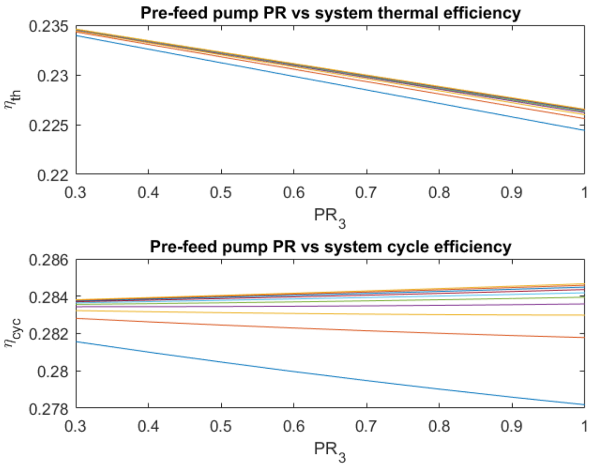

Figure 4-12: Overall system performance trend for pre-feed pump deterioration.

In summary, just like in the case of the storage vessel, only the succeeding component is affected. A drop on the pressure ratio across the pre-feed pump would influence the pressure head that the main pump has to produce which translates to a higher shaft rotational speed. Recall that pre-feed pump also supplies the needed pressure to the lubrication and bearing system, which ensures that there is no contact between the hydrodynamic bearing and the shaft; however, if the pre-feed pump does not provide the required pressure, it is impossible for the shaft to attain a higher speed without causing damage. Thus, it is imperative that the ruleset to evaluate a pressure drop across the pre-feed pump should contain the pressure ratio across the main pump so that no catastrophic damage occurs.

4.3.3 Main pump

Just like the pre-feed pump, any of the three selected fault mechanism can occur in the main pump. Therefore, the total-to-total pressure ratio and isentropic efficiency are also valid health indices. Additionally, the volumetric efficiency is another performance index selected for the pre-feed pump. However, it cannot be calculated for the main pump because it is a function of the volumetric flow rate, which is not easily deducible for the main pump due to unavailable performance maps. Therefore, only deteriorations due to the total-to-total pressure ratio and isentropic efficiency will explored for this case.

The state equation for calculating the main pump exit pressure has been modified in the same manner as in previous sections.

$$P_5 = (P_6 + \nabla P_6)PR_5 \qquad \text{Equation 4-12}$$

Where PR_5 is the pressure ratio across the pre-feed pump and assumes a value from 0 to 1 for the simulation. In addition, the standard equation to compute the isentropic efficiency of a pump is utilised in estimating the enthalpy at the exit so that it is possible to vary the main pump isentropic efficiency.

$$h_5 = h_3 + \frac{h_{5s} - h_3}{\eta_{5s}}$$ **Equation 4-13**

Before the main pump is the pre-feed pump and because the computation algorithm of the surrogate model has been designed such that the head generated by the main pump at the operating speed determines the exit pressure of the pre-feed pump, there is an observable effect on the pressure ratio across the pre-feed pump. This effect is presented in Figure 4-13. It can be seen that the pressure ratio across the pre-feed pump and the pre-feed pump isentropic efficiency decreases linearly as the pressure ratio across the main pump deteriorates. Furthermore, as the pressure ratio of the main pump approaches a little below 95.5% of its design value, complete pressure is lost in the pre-feed pump. The significance of this plot is that the main pump and thus the system in general is unable to perform without enough suction head from the pre-feed pump. In addition, varying the isentropic efficiency of the main pump had no effect on the efficiency of the pre-feed pump.

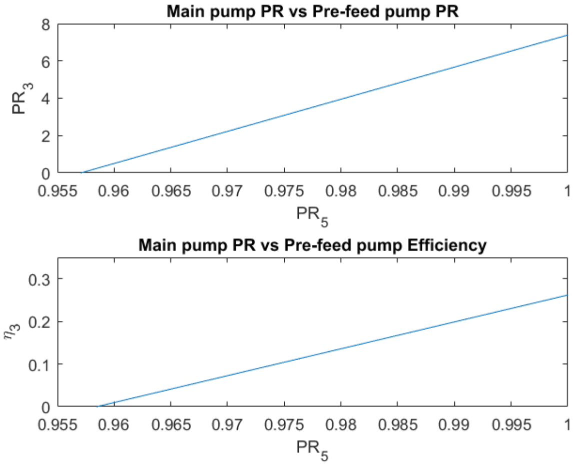

Figure 4-13: Pre-feed pump health index trend for main pump deterioration.

The next component after the main pump is the recuperator; while a variation in the isentropic efficiency of the main pump had no effect on the recuperator, a deterioration in the pressure ratio across the main pump results in a rise in the pressure ratio across the cold side of the recuperator (Figure 4-14). However, because the effectiveness of the recuperator has been set from the start, this rise in pressure ratio across the cold side of the recuperator corresponding to a drop in pressure ratio across the main pump had no effect on the hot side of the recuperator.

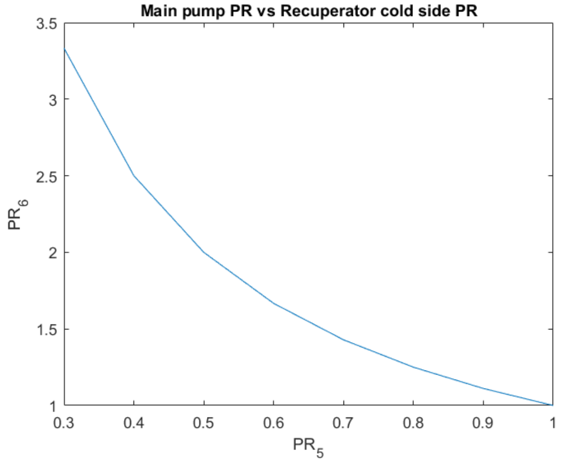

Figure 4-14: Recuperator (cold side) health index trend for main pump deterioration.

In the evaporator (Figure 4-15), a deterioration in the pressure ratio across the main pump results in a gradual decrease in evaporator effectiveness. However, a deterioration in the main pump isentropic efficiency has a more significant effect on the evaporator effectiveness with the value dropping faster with decreasing main pump isentropic efficiency. In addition, as the isentropic efficiency of the main pump approaches 10% while producing 40% of the possible head, the effectiveness of the evaporator tends drops sharply which indicates an inoperable condition.

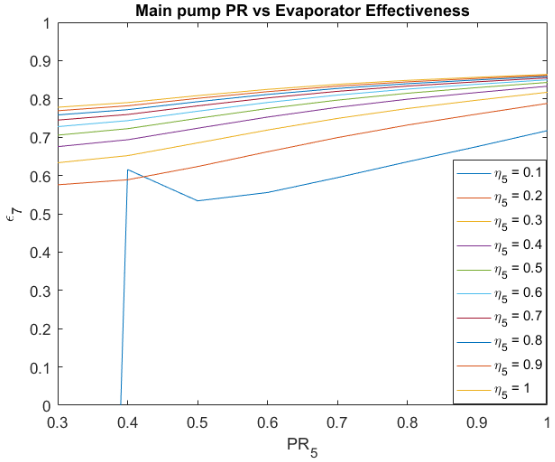

Figure 4-15: Evaporator health index trend for main pump deterioration.

In the turbine, the pressure ratio effect is more severe (Figure 4-16). A pressure drop across the main pump puts a strain on the turbine and much higher main pump isentropic efficiencies are required as the pressure drop increases. In addition, beyond a certain main pump pressure ratio, the ORC system cannot operate. This means that, at maximum power, deterioration in the pressure ratio across the main pump has a significant effect on the turbine performance. Intuitively, this makes sense because the main pump and turbine are mounted on the same shaft so they run at the same speed; therefore, to produce the same power for an underperforming main pump, the turbine must be extra efficient.

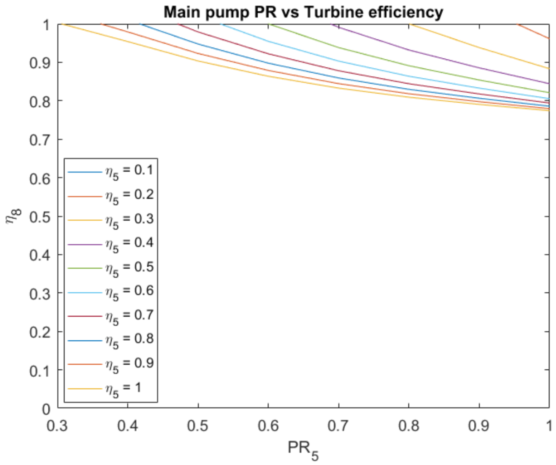

Figure 4-16: Turbine health index trend for main pump deterioration.

The condenser experiences a rise in effectiveness for main pump isentropic efficiencies above 10% as the pressure ratio across the main pump deteriorates (Figure 4-17) whereas, at 10% main pump isentropic efficiency, the condenser effectiveness decreases with an increase in main pump pressure ratio. In addition, the main pump pressure ratio vs condenser effectiveness curve rotates about a main pump pressure ratio of about 0.65 as the main pump isentropic efficiency is varied. This rotation is clockwise as the isentropic efficiency increases from 20% to maximum; thus, this means that at a main pump pressure ratio of 0.65 and main pump isentropic efficiencies above 10%, the condenser effectiveness will remain unchanged regardless of the main pump isentropic efficiency. Furthermore, as with the evaporator, as the isentropic efficiency of the main pump approaches 10% while producing 40% of the possible head, the effectiveness of the condenser tends towards a negative value, which is impossible and thus signifies an inoperable condition.

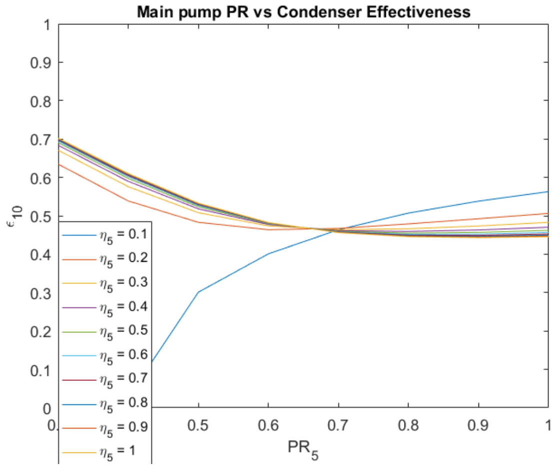

Figure 4-17: Condenser health index trend for main pump deterioration.

A look at the overall system performance (Figure 4-18) shows that a change in the main pump pressure ratio has a negligible effect on the thermal efficiency but significantly affects the cycle efficiency while the main pump isentropic efficiency has a lesser effect on the cycle efficiency but a greater effect on the thermal efficiency of the ORC system.

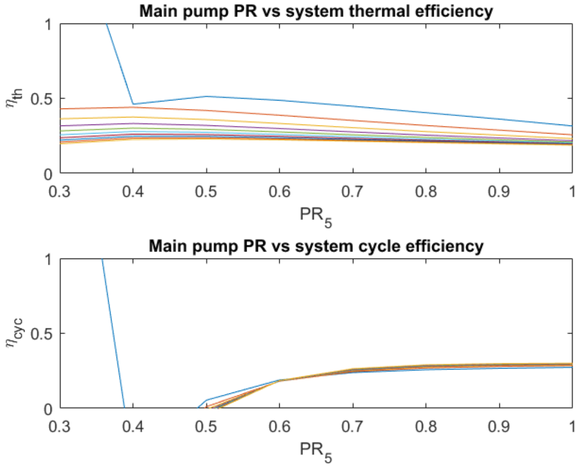

Figure 4-18: Overall system performance for main pump deterioration.

In conclusion, the effect of a deterioration in the main pump pressure ratio and isentropic efficiency affects the other components in the ORC system because its performance has a direct influence on them. Nonetheless, the best combination for the ruleset would include the pressure ratio across the cold side of the recuperator and the turbine efficiency because the effects of a pressure drop across the main pump results in a more rapid change on these health parameters.

4.3.4 Recuperator

For both sides of the recuperator, the total-to-total pressure ratio and the effectiveness have been selected as health indices and are varied to observe performance trends. However, variation of the effectiveness affects both sides of the recuperator; therefore, the effectiveness will be varied in conjunction with both side total-to-total pressure ratios to observe the performance trends for either side of the recuperator. As for previous cases, the pressure at the exit of the cold side of the recuperator is modified into the form:

$$P_6 = (P_7 + \nabla P_7)PR_6 \qquad \text{Equation 4-14}$$

Where PR_6 is the pressure ratio across the cold side of the recuperator and assumes a value from 0 to 1 for the simulation. And at the hot side, the equation for the exit pressure is re-written as:

$$P_9 = (P_{10} + \nabla P_{10})PR_9 \qquad \text{Equation 4-15}$$

Where PR_9 is the pressure ratio across the hot side of the recuperator and assumes a value from 0 to 1 for the simulation. The recuperator effectiveness has already been included in the original derivation of the state equations so there is no need for further modification.

In the cold side of the recuperator, the pressure ratio across the storage vessel is unaffected. However, the pressure ratio and efficiency across the pre-feed pump are only affected by a deterioration in the pressure ratio across the cold side of the recuperator and not by a deterioration in recuperator effectiveness. The reason for this effect, shown in Figure 4-19, is that the evaporating pressure dictates the pressure at each control point upstream of the evaporator exit. A deterioration in the pressure ratio across the cold side of the recuperator has a huge negative impact on the pressure ratio across the pre-feed pump and the pre-feed pump isentropic efficiency. Furthermore, the main pump becomes inoperable at maximum power when the pressure ratio across the cold side of the recuperator approaches 95% of its design value.

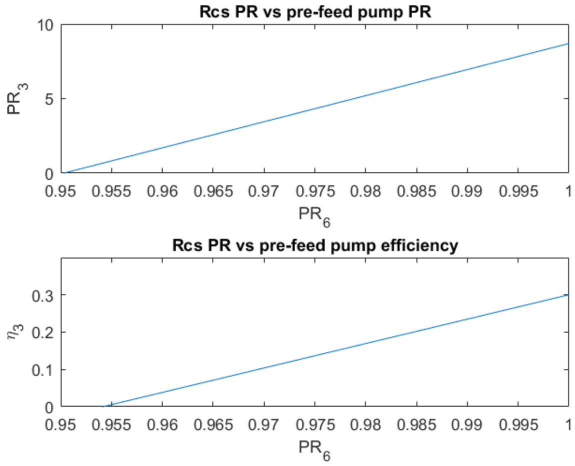

Figure 4-19: Pre-feed pump health indices trend for recuperator (cold side) deterioration.

In the main pump, the pressure ratio drops rapidly just as the pressure ratio across the cold side of the recuperator goes a little below 95% of its capacity. However, as the pressure ratio across the cold side of the recuperator decreases, the isentropic efficiency of the main pump rises though negligibly (Figure 4-20). In addition, the recuperator effectiveness has no effect on the performance characteristics of the main pump.

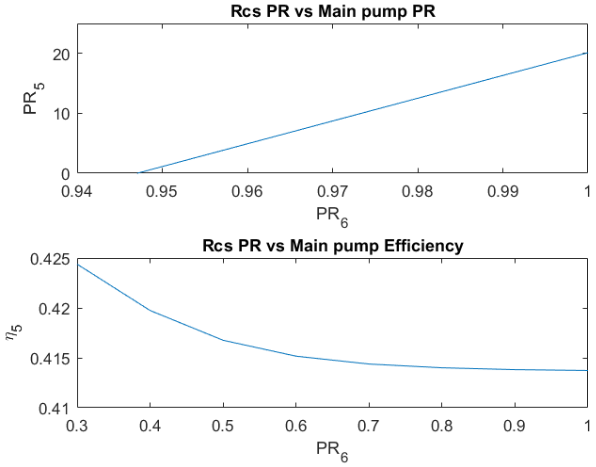

Figure 4-20: Main pump health indices trend for recuperator (cold side) deterioration.

The pressure ratio across the hot side of the recuperator is neither affected by a deterioration in recuperator effectiveness nor a pressure drop across the cold side of the recuperator. However, a deterioration in the pressure ratio across the cold side of the recuperator results in a rise in the pressure ratio across the evaporator but a deterioration in the recuperator effectiveness has no effect on the pressure ratio across the evaporator (Figure 4-21). Furthermore, both a deterioration in recuperator effectiveness and the pressure ratio across the cold side of the recuperator influence the evaporator effectiveness. At normal operating conditions and without any deterioration in the cold side of the recuperator (at $PR_6 = 1$), the effectiveness of the evaporator increases with increasing recuperator effectiveness but as the pressure ratio across the cold side of the recuperator deteriorates; the evaporator effectiveness reduces at higher recuperator effectiveness and increases at lower recuperator effectiveness.

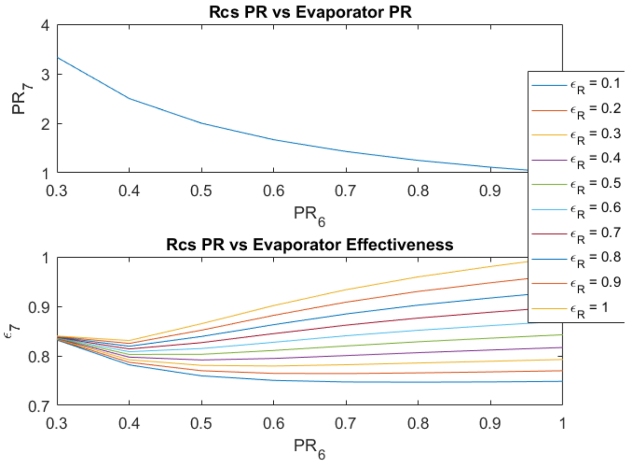

Figure 4-21: Evaporator health indices trend for recuperator (cold side) deterioration.

The pressure ratio across the turbine and the turbine isentropic efficiency are unaffected by a deterioration in recuperator effectiveness. However, as the pressure ratio across the cold side of the recuperator decreases, the pressure ratio across the turbine decreases while the turbine isentropic efficiency increases and exceeds 100% just before the pressure ratio across the cold side of the recuperator drops below 75% (Figure 4-22).

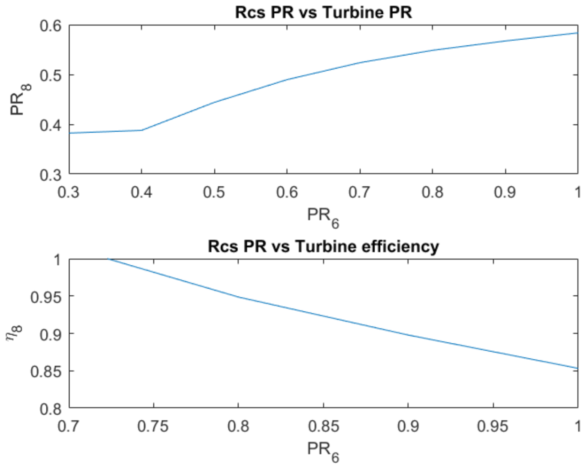

Figure 4-22: Turbine health indices trend for recuperator (cold side) deterioration.

In the condenser, a drop in the pressure ratio across the cold side of the recuperator has no effect on the condenser pressure ratio; however, the pressure drop causes the condenser effectiveness to drop at lower recuperator effectiveness but as the recuperator effectiveness improves, the condenser effectiveness begins to rise exponentially (Figure 4-23).

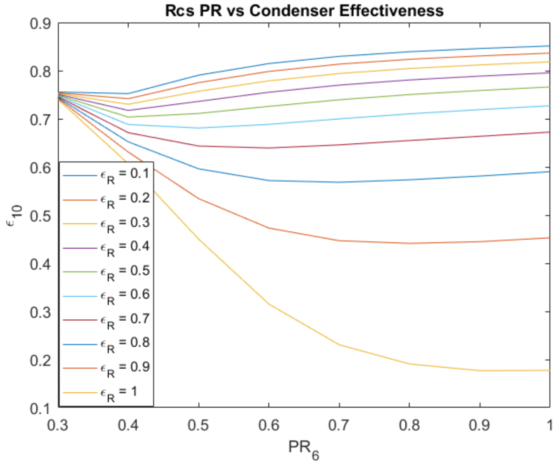

Figure 4-23: Condenser health index trend for recuperator (cold side) deterioration.

In conclusion, an observation of the pressure ratios across components upstream of the cold side of the recuperator gives a good indication of the severity of pressure deterioration in the cold side of the recuperator while observing the effectiveness of the evaporator and condenser gives an indication of the state of the recuperator effectiveness. Thus, the ruleset selected must contain these key health indices.

Furthermore, varying the pressure ratio across the hot side of the recuperator together with the recuperator effectiveness does not have as much effect as the cold side. A pressure drop across the recuperator hot side only influences the pressure ratio of the condenser whilst a deterioration of the recuperator effectiveness only affects the condenser and evaporator effectiveness.

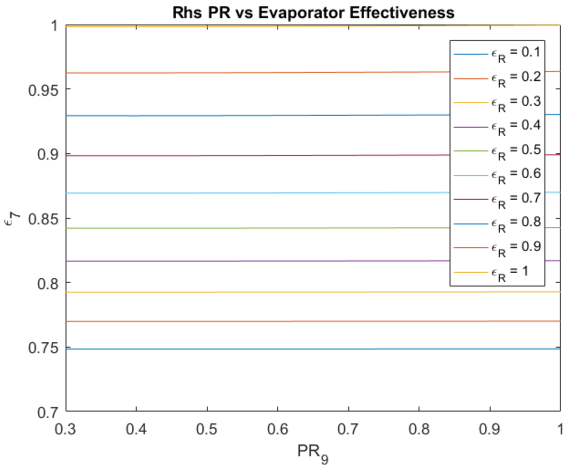

Figure 4-24: Evaporator health index trend for recuperator (hot side) deterioration.

As shown in Figure 4-24, a deterioration in the recuperator effectiveness causes the evaporator effectiveness to drop rapidly. In total, the evaporator effectiveness drops by 25% when there is no heat transfer between the hot and cold side of the recuperator i.e. the evaporator effectiveness will be 25% less without the recuperator being part of the ORC system. Furthermore, a change in the pressure ratio across the hot side of the evaporator has no effect on the evaporator effectiveness.

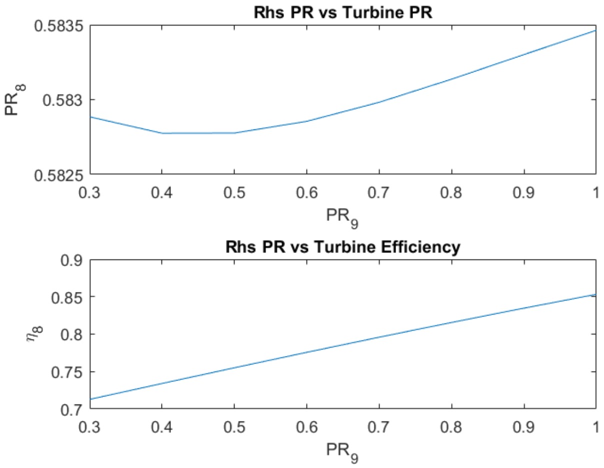

Figure 4-25: Turbine health index trend for recuperator (hot side) deterioration.

A change in the recuperator effectiveness has no effect on both the pressure ratio across the turbine or the turbine isentropic efficiency (Figure 4-25). This follows intuitively because regardless of the recuperator degradation or underperformance, the design temperature for the evaporator is constant for this simulation and thus the turbine inlet temperature is the same. However, the pressure ratio across the hot side of the recuperator has a significant effect on the turbine isentropic efficiency but a not so significant effect on the pressure ratio across the turbine.

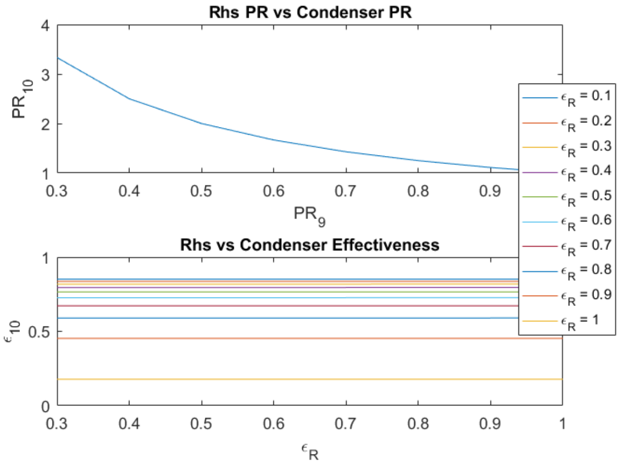

Figure 4-26: Condenser health index trend for recuperator (hot side) deterioration.

In Figure 4-26, the effect of a deterioration in the recuperator effectiveness and pressure ratio are shown. A deterioration in the pressure ratio across the hot side of the recuperator results in a rise in the pressure ratio across the condenser. In addition, a drop in the recuperator effectiveness results in a rise in condenser effectiveness.

A look at the overall system performance (Figure 4-27) shows that a change in the pressure ratio across the cold side of the recuperator has a significant effect on both the thermal and cycle efficiency. A decrease in the pressure ratio results in an increase followed by a decrease in the thermal efficiency and an exponential decrease in the cycle efficiency. Furthermore, a change in recuperator effectiveness causes an increase in the cycle and thermal efficiencies. In addition, at lower pressure ratios, the effect of a change in the recuperator effectiveness becomes less on the thermal and cycle efficiencies.

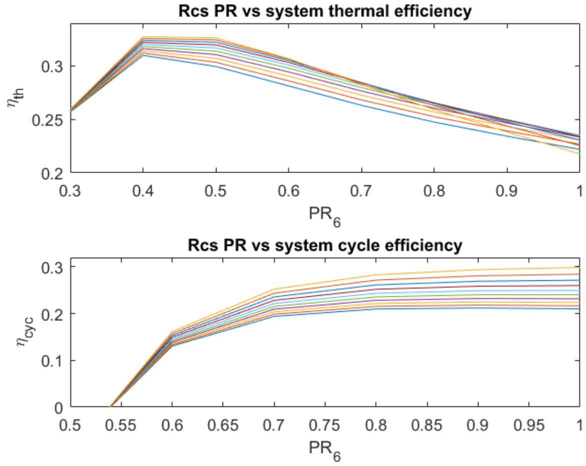

Figure 4-27: Overall system performance for recuperator (cold side) deterioration.

In Figure 4-28, it is obvious that a change in the pressure ratio across the hot side of the recuperator has very little effect on the thermal efficiency and no effect on the cycle efficiency at constant recuperator effectiveness. Furthermore, a change in recuperator effectiveness causes a slight variation in the thermal efficiency but a comparatively larger variation in the cycle efficiency. A complete loss of recuperator effectiveness would cause the cycle efficiency to drop by almost 30% and the thermal efficiency to vary by less than 8%.

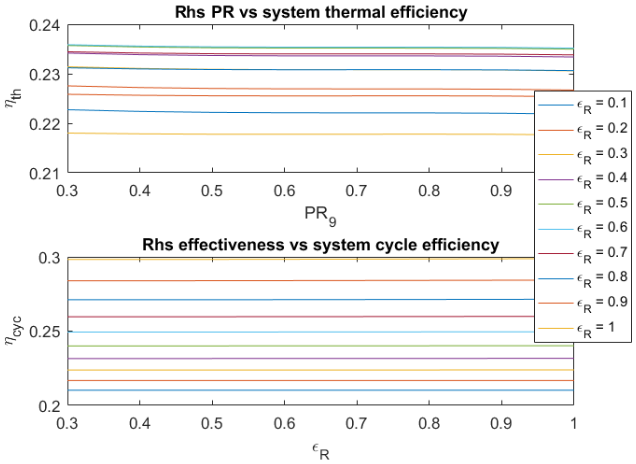

Figure 4-28: Overall system performance for recuperator (hot side) deterioration.

Summarily, a drop in the recuperator effectiveness only influences the effectiveness of the evaporator and condenser. While the evaporator effectiveness deteriorates due to a deterioration in the recuperator effectiveness, the condenser effectiveness appreciates. The reason for this is that the surrogate model is designed such that the condensing pressure and temperature is constant; therefore, regardless of the inlet temperature and pressure of the condenser the state of the working fluid upon exiting the condenser is always constant. On the other hand, the evaporator effectiveness is a function of its inlet temperature and because the recuperator effectiveness dictates this inlet temperature of the evaporator, a deterioration in recuperator effectiveness means a lower inlet temperature of the evaporator and thus a lower evaporator effectiveness since the inlet and outlet temperature of the flue gas are kept constant.

4.3.5 Evaporator

For the evaporator, the total-to-total pressure ratio and the effectiveness have been selected as health indices. Recall that the effectiveness is a function of the hot fluid inlet and outlet temperatures as well as the cold fluid inlet temperature and that the flue gas inlet and outlet temperature and the evaporator exit temperature are inputs for the surrogate model. Furthermore, a reduced effectiveness of the evaporator should influence the outlet temperature of the evaporator. Thus, to vary evaporator degradation, the evaporator exit temperature will not be an input but rather expressed as a function of its effectiveness.

The evaporator exit pressure is a control variable and is expressed as:

$$P_7 = 35PR_7 \qquad \text{Equation 4-16}$$

Where PR_7 is the pressure ratio across the evaporator and assumes a value from 0 to 1 for the simulation. In addition, the evaporator effectiveness ε_E is introduced into the state equations to calculate the temperature at the evaporator inlet.

$$T_6 = \frac{T_{FI}(\varepsilon_E - 1) + T_{FO}}{\varepsilon_E} \qquad \text{Equation 4-17}$$

The effects of varying the evaporator pressure ratio resulted in an accelerated deterioration of the pre-feed pump characteristics. However, a deterioration in the evaporator effectiveness had no effect on the pre-feed pump. Figure 4-29 shows that the pre-feed pump pressure ratio and isentropic efficiency completely deteriorates before the evaporator pressure ratio reaches 95% of its design value.

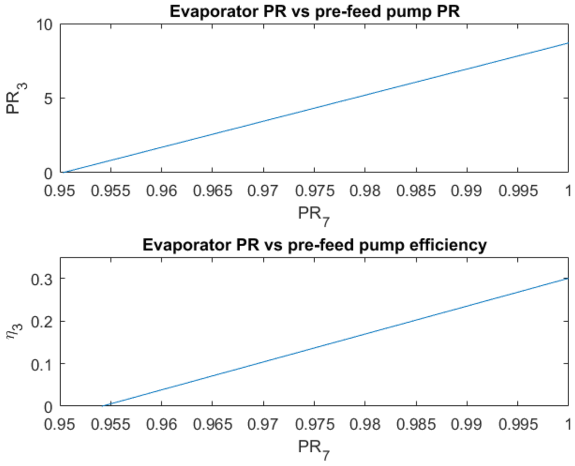

Figure 4-29: Pre-feed pump health indices trend for evaporator deterioration.

In the main pump, a reduction in the evaporator pressure ratio also causes a rapid decline in the main pump pressure ratio; however, the main pump isentropic efficiency only deteriorates to around 15% (Figure 4-30) of its design value. In addition, just like with the pre-feed pump, a change in the evaporator effectiveness has no effect on the main pump performance characteristics.

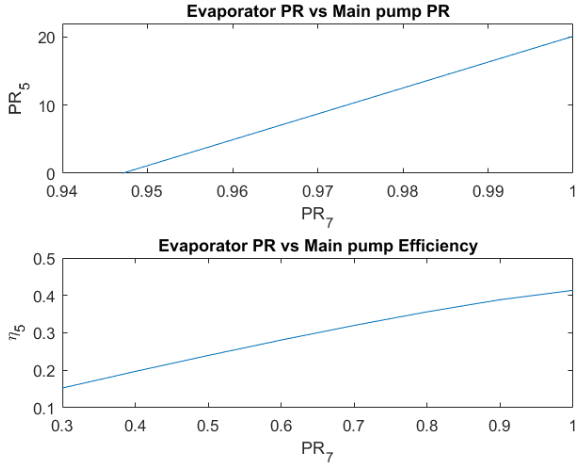

Figure 4-30: Main pump health indices trend for evaporator deterioration.

In the recuperator, a change in the evaporator pressure ratio has no effect on the cold side or hot side pressure ratio but a change in the evaporator effectiveness and pressure ratio has some effect on the recuperator effectiveness (Figure 4-31). At higher evaporator pressure ratios, the recuperator effectiveness is lowest for lower evaporator effectiveness but becomes unstable as the pressure ratio across the evaporator reduces.

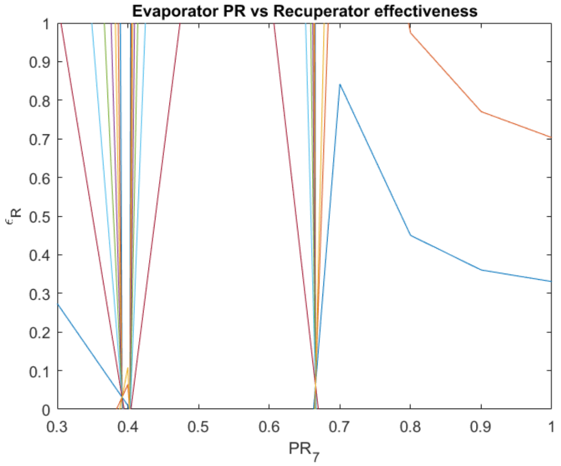

Figure 4-31: Recuperator (cold side) health indices trend for evaporator deterioration.

A change in evaporator effectiveness has no effect on the turbine performance. However, a deterioration in evaporator pressure ratio results in a gradual deterioration in the turbine pressure ratio up until when pressure is totally lost in the turbine when the evaporator pressure ratio approaches at 60% of its design value. Beyond a 60% drop in the evaporator pressure ratio, the pressure ratio across the turbine becomes unstable. Furthermore, a deterioration in evaporator pressure ratio results in an increase in the turbine isentropic efficiency until the pressure ratio across the evaporator drops below 90% when the turbine becomes inoperable (Figure 4-32).

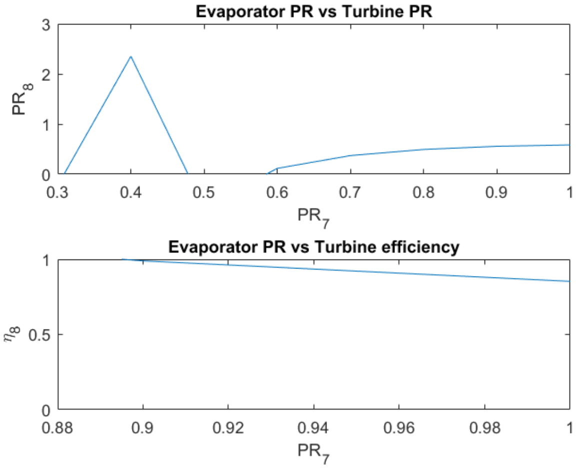

Figure 4-32: Turbine health indices trend for evaporator deterioration.

Figure 4-33 shows that in the condenser, a very unstable phenomenon occurs for the condenser effectiveness with varying evaporator pressure ratio and effectiveness. Essentially, the condenser effectiveness stays close to unity, regardless of the evaporator pressure ratio, at low evaporator effectiveness, which is intuitive because there is less heat to be extracted from the system. Furthermore, as the evaporator effectiveness increases, there is a haphazard behaviour for the condenser effectiveness with varying pressure ratio.

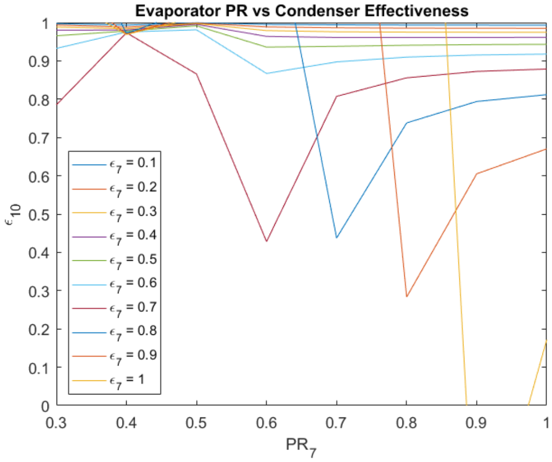

Figure 4-33: Condenser health indices trend for evaporator deterioration.

The overall system performance (Figure 4-34) shows that a deterioration in the pressure ratio across the evaporator has a significant effect on both the thermal and cycle efficiency. A deterioration in the evaporator pressure ratio results in an increase in the thermal efficiency for all evaporator effectiveness values; however, as the pressure ratio across the evaporator exceeds 60% of its design value, the thermal efficiency assumes very unstable values. This behaviour is intuitive because at steady operating conditions, if pressure is lost in the evaporator there will be more heat transferred to the working fluid because the mass flow increases. Furthermore, there is a reduction in cycle efficiency as the pressure ratio across the evaporator increases; the reason for this is that the overall cycle pressure ratio determines the amount of work extracted in the turbine, thus affecting the overall efficiency of the ORC system. In addition, a change in recuperator effectiveness causes an increase in the cycle and thermal efficiencies. Also noticeable in Figure 4-34 is that an increase in evaporator effectiveness causes the peak of the cycle efficiency curve to increase and the cycle becomes inoperable as the pressure ratio across the evaporator goes a little below 55% of its design value.

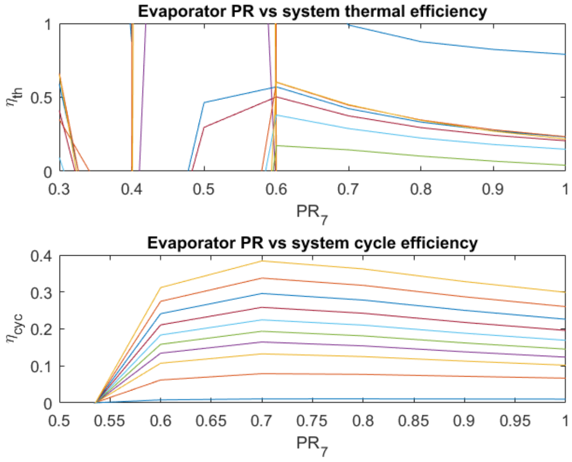

Figure 4-34: Overall system performance for evaporator deterioration.

Summarily, only the pre-feed pump, main pump and turbine performance characteristics provide a better reflection of the evaporator health condition because of the unstable nature of the health parameters of the other components.

4.3.6 Turbine

Like the other turbomachinery components, all three fault mechanisms considered in this research can occur in the turbine; thus, deterioration of the total-to-total pressure ratio and the isentropic efficiency will be assessed to obtain performance trends. The state equation of the pressure at the exit of the turbine is re-written as:

$$P_8 = (P_9 + \nabla P_9)PR_8 \qquad \textbf{Equation 4-18}$$

Where PR_8 is the pressure ratio across the turbine and assumes a value from 0 to 1 for the simulation. While the state equation to calculate the enthalpy at the exit of the turbine is re-written as a function of the isentropic efficiency to be able to run simulations for different values.

$$h_8 = h_7 - \eta_{8s}(h_7 - h_{8s}) \qquad \textbf{Equation 4-19}$$

For this case of the turbine, the storage vessel, pre-feed pump, main pump, and pressure ratio across the cold side of the recuperator are neither unaffected by a pressure drop across the turbine nor by a change in the turbine isentropic efficiency. However, the pressure ratio across the hot side of the recuperator is significantly affected by a deterioration in the turbine pressure ratio as can be seen in Figure 4-35.

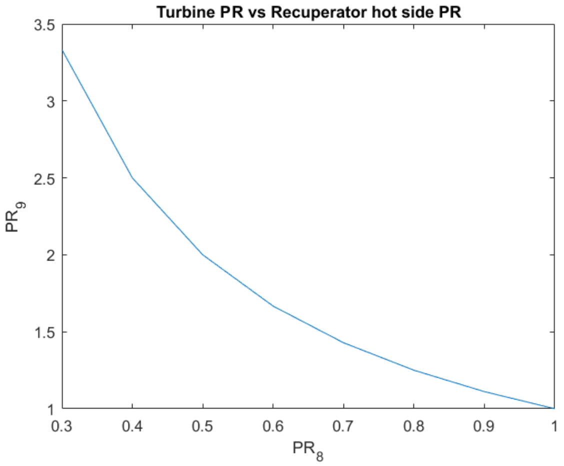

Figure 4-35: Recuperator (hot side) health index trend for turbine deterioration.

There is a rapid rise in the pressure ratio across the hot side of the recuperator with a decrease in the turbine pressure ratio. Furthermore, an interesting observation is that as the pressure ratio across the turbine drops to around 30% of its ideal value, the pressure ratio across the hot side of the recuperator more than triples.

In the evaporator, as the pressure ratio across the turbine decreases, the evaporator effectiveness deteriorates; and, as the isentropic efficiency of the turbine decreases, the effectiveness of the evaporator becomes more favourable (Figure 4-36). However, at low turbine isentropic efficiencies, the evaporator effectiveness curve tends towards unity signifying that the evaporator exceeds its operating range beyond a turbine isentropic efficiency of 70%.

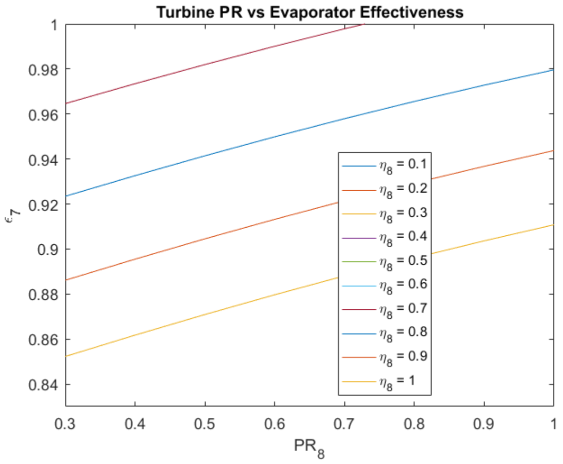

Figure 4-36: Evaporator health index trend for turbine deterioration.

A deterioration in turbine pressure ratio corresponds to a deterioration in the condenser effectiveness at high turbine isentropic efficiencies albeit negligible; however, as the turbine isentropic efficiency decreases, the condenser effectiveness becomes almost constant regardless of the magnitude of the pressure ratio across the turbine. Furthermore, a deterioration in turbine isentropic efficiency corresponds to an improvement in the condenser effectiveness (Figure 4-37).

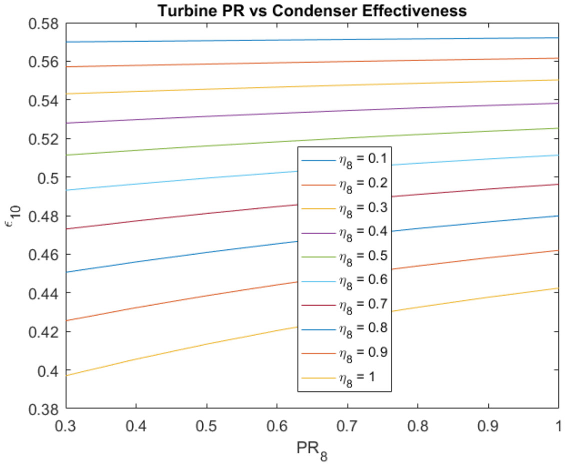

Figure 4-37: Condenser health index trend for turbine deterioration.

The overall system performance (Figure 4-38) shows that a change in the pressure ratio across the turbine has a significant effect on both the thermal and cycle efficiency. A deterioration in the turbine pressure ratio results in an increase in both the thermal and cycle efficiencies for all values of turbine isentropic efficiencies; however, the thermal efficiency at low turbine isentropic efficiencies fall outside the realistic operating range. Thus, high turbine isentropic efficiencies are much more desirable for the ORC to operate.

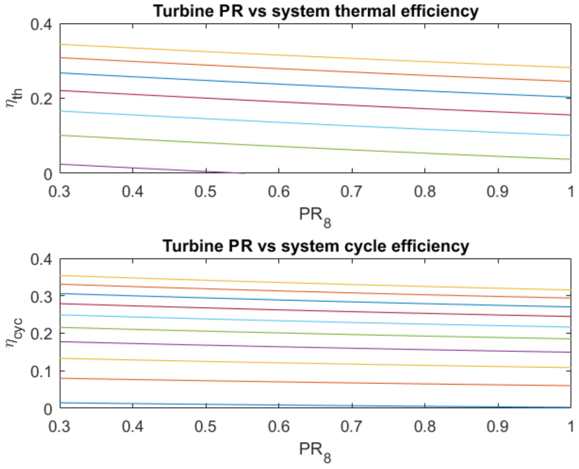

Figure 4-38: Overall system performance for turbine deterioration.

Summarily, the only components affected by a deterioration in the turbine performance are the hot side of the recuperator, the evaporator and the condenser. This is expected because the turbine exit pressure, hot side of the recuperator and condenser exit pressure are interrelated. Therefore, to ascertain a deterioration in turbine health, the rulesets would be a combination of the health indices of these three components.

4.3.7 Condenser

The total-to-total pressure ratio and the effectiveness have been selected as the health indices to be used in assessing the condenser performance. In addition, as with the case of the evaporator, the effectiveness of the condenser is a function of the hot fluid inlet and outlet temperatures as well as the cold fluid inlet temperature. However, the cooling fluid inlet and outlet temperature and the condenser exit temperature are inputs for the surrogate model and a reduced effectiveness of the condenser would directly influence its outlet temperature. Therefore, to vary condenser deterioration, the condenser exit temperature will be expressed as a function of the effectiveness.

The state equation for the condenser outlet pressure is re-written as:

$$P_{10} = 0.2PR_{10} \qquad \textbf{Equation 4-20}$$

Where PR_{10} is the pressure ratio across the condenser and assumes a value from 0 to 1 for the simulation. Furthermore, the condenser effectiveness ε_C is introduced into the state equations to calculate the temperature at the evaporator inlet.

$$T_{CI} = \frac{T_9(\varepsilon_C - 1) + T_{10}}{\varepsilon_C} \qquad \textbf{Equation 4-21}$$

In Equation 4-21, it is evident that running the simulation only affects the coolant inlet temperature; thus, it follows that the coolant mass flow rate is adjusted accordingly to ensure that the condensing temperature is kept constant.

A deterioration in the condenser effectiveness has no effect on the components in the ORC system because the condensing temperature is set constant regardless of the state of the system. In real life application, this is always the case because the condenser will always produce a set output irrespective of the inlet conditions. However, a deterioration in the condenser pressure ratio has some noticeable effect on some of the components.

As presented in Figure 4-39, a deterioration in the condenser pressure ratio results in slight rise in the pressure ratio across the pre-feed pump. The pressure ratio across the pre-feed pump first rises gradually but as the pressure ratio across the condenser further deteriorates, the pressure rise across the pre-feed pump rises to almost thirty times the initial value. In addition, a deterioration in the pressure ratio across the condenser results in a negligible increase in the pre-feed pump isentropic efficiency.

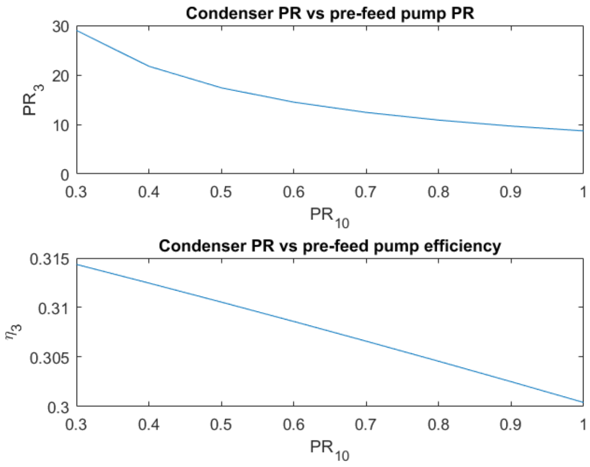

Figure 4-39: Pre-feed pump health indices trend for condenser deterioration.

Furthermore, a deterioration in the pressure ratio across the condenser causes a negligible decrease and increase in the pressure ratio and isentropic efficiency of the main pump respectively (Figure 4-40).

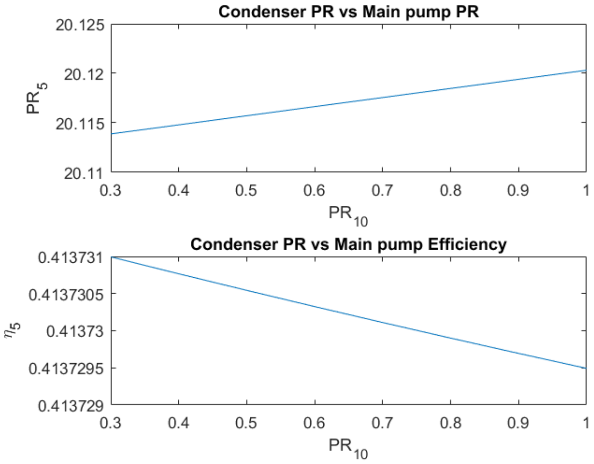

Figure 4-40: Main pump health indices trend for condenser deterioration.

Neither a deterioration in the condenser pressure ratio nor effectiveness has any effect on both sides of the recuperator or on the turbine pressure ratio and isentropic efficiency. However, a deterioration in the condenser pressure ratio has an interesting but negligible effect on the evaporator effectiveness but no effect on the evaporator pressure ratio (Figure 4-41). As the pressure ratio across the condenser decreases, there is a decrease then an increase in the evaporator effectiveness.

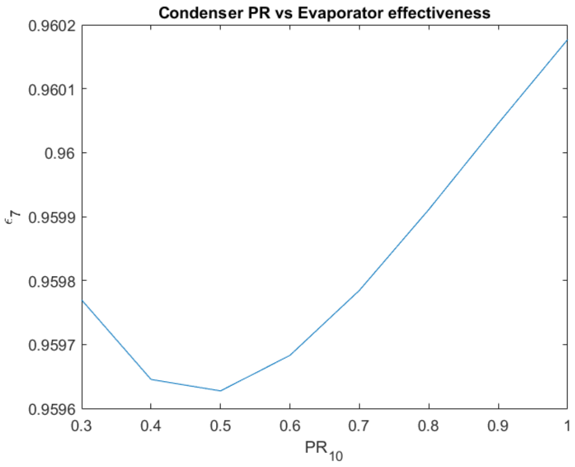

Figure 4-41: Evaporator health index trend for condenser deterioration.

The overall system performance (Figure 4-42) reveals that a deterioration in condenser effectiveness has no effect on both the thermal and cycle efficiency. However, a deterioration in the pressure ratio across the condenser has an effect on the thermal and cycle efficiencies, though negligible.

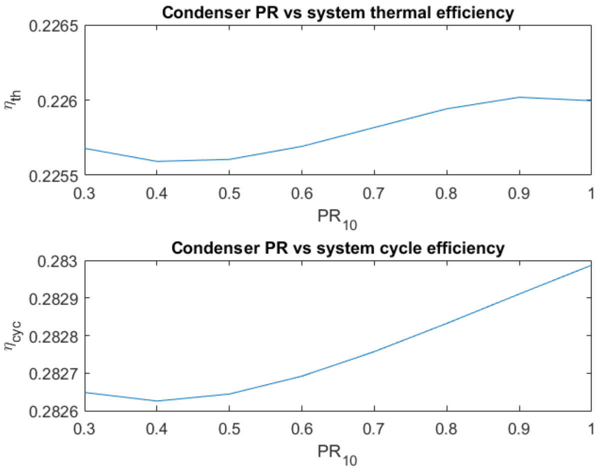

Figure 4-42: Overall system performance for condenser deterioration.

In summary, the only significant effect because of a condenser deterioration is a deterioration in the pre-feed pump pressure ratio. Therefore, an assessment of the pre-feed pump pressure ratio would aid in identifying fault root cause in the case of a condenser defect and should be included in the ruleset.

4.3.8 Summary

In previous sub-sections, deterioration modes were simulated for each of the components in the ORC system and the effects have been recorded and discussed. However, because of the interrelationships between components, ascertaining fault root cause when the system behaves below par is difficult. Furthermore, an assessment of the health parameters only is in most cases insufficient to identify the source of the problem. Thus, Table 4-2 presents a fault table where the health indices are listed alongside the thermophysical properties at each control point in the system and the properties that are subject to change in the event of a health index deviation are identified.

Table 4-2: Component health indices effect on system thermophysical properties.

	P_1	T_1	P_3	T_3	P_5	T_5	P_6	T_6	P_7	T_7	P_8	T_8	P_9	T_9	P_{10}	T_{10}
PR_1	X		X	X		X		X			X	X		X		
PR_3			X	X		X		X				X		X		
η_{3s}				X		X		X				X		X		
PR_5			X	X	X	X		X				X		X		
η_{5s}						X		X				X		X		
PR_6			X	X	X	X	X	X				X		X		
PR_9								X			X	X	X	X		
ε_R								X						X		
PR_7			X	X	X	X	X		X			X		X		
ε_E								X						X		
PR_8								X			X	X		X		
η_{8s}								X				X		X		
PR_{10}	X		X	X		X		X			X	X	X	X	X	
ε_C																

Note that this fault table is unique to the computation algorithm selected for the surrogate modelling of the ORC system. The control variables (e.g. evaporating and condensing thermophysical properties) are unaffected in this simulation and because the storage vessel has been assumed neutral. In addition, the condenser effectiveness has no effect on the system thermophysical parameters because the condensing temperature has been set as a control variable. An assessment of the index deviation charts in combination with the fault table (Table 4-2) should be utilised to determine the root cause of fault in the ORC system. For example, all components except the turbine has some effect on the pressure ratio across the pre-feed pump; thus, it is possible that the index deviation chart shows a deviation in the pre-feed pump characteristics because of smearing effects. However, a deterioration in the pre-feed pump pressure ratio only affects the main pump pressure ratio and has no significant effect on the health indices of the other components; thus it possible to eliminate the possibility of a fault with the pre-feed pump if the main pump is unaffected.

Table 4-3: Component health indices interrelationships.

	PR_1	PR_3	η_{3s}	PR_5	η_{5s}	PR_6	PR_9	ε_R	PR_7	ε_E	PR_8	η_{8s}	PR_{10}	ε_C
PR_1	■	X	X	X	X			X		X	X	X		X
PR_3		■		X	X			X		X	X	X		X
η_{3s}			■		X			X		X	X	X		X
PR_5		X	X	■	X	X		X		X		X		X
η_{5s}					■			X		X		X		X
PR_6		X	X	X	X	■		X	X	X	X	X		X
PR_9							■	X		X	X	X	X	X
ε_R								■		X				X
PR_7		X	X	X	X	X		X	■		X	X		X
ε_E								X		■				X
PR_8							X	X		X	■			X
η_{8s}								X		X	X	■		X
PR_{10}	X	X	X	X	X		X	X		X	X	X	■	X
ε_C														■

Furthermore, Table 4-3 presents the fault interrelationship between health indices. In the next chapter, health analysis is performed on two Triogen ORC systems, which are currently in operation; and, the root cause of the deviations, observed are determined. It is important to keep in mind that the simulated faults and corresponding trends represent the behaviour of the ORC at the optimum design conditions.

5 Validation and performance

In this chapter, the condition monitoring tool is applied to two Triogen ORC's currently in operation. The purpose of carrying out this procedure on an active engine is to ensure that the condition monitoring tool that has been developed is able to perform the function for which it has been designed. The condition monitoring tool has been implemented in Matlab and the data, which is drawn from Triogen archives, is read as .txt files, processed, analysed and conclusions are drawn concerning the health status of the ORC. As discussed previously, the control variables are used as input values in describing the surrogate model and the component design specifications are constants that have been selected based on consultation with the engineers at Triogen. Table 5-1 presents the input data for the Matlab script.

Table 5-1: Input values for case studies.

Control variable	**Design value**
T_{FI}	$T_{FI_{eng}}$
T_{FO}	$T_{FO_{eng}}$
T_{CI}	$T_{CI_{eng}}$
T_{CO}	$T_{CO_{eng}}$
T_7	$T_{7_{eng}}$
P_7	$P_{7_{eng}}$
T_{10}	$T_{10_{eng}}$
P_{10}	$P_{10_{eng}}$
N_3	$1450\ rpm$
N_5	$N_{5_{eng}}$
PtG	PtG_{eng}
Ψ_5	0.65
ε_R	0.89
∇P_6	0.386 bar
∇P_7	0.544 bar
∇P_9	0.000594 bar
∇P_{10}	0.01 bar

Where the subscript "eng" symbolizes the active engine parameter value.

It is important to mention that deviation charts presented represent the state of the system at the end of each case. Furthermore, the data utilised were checked to ensure that the system behaviour was steady at the end and did not vary to eliminate faults that may appear because of random fluctuations in the system.

5.1 Case 1

In this test, the data considered is over a period of one week for normal operation of the Triogen ORC system. Fault diagnostics was run to assess the ORC performance and the results, describing the state of the ORC system at the end of the duration considered, are presented and discussed. It is also important to note that there are no archived data for the pre-feed pump exit temperature and the condenser exit temperature and pressure. Therefore, the properties of the working fluid in the storage vessel has been assumed to be the condensing pressure and temperature while the pre-feed pump exit temperature was computed using pump curves and sensor readings for the active engine.

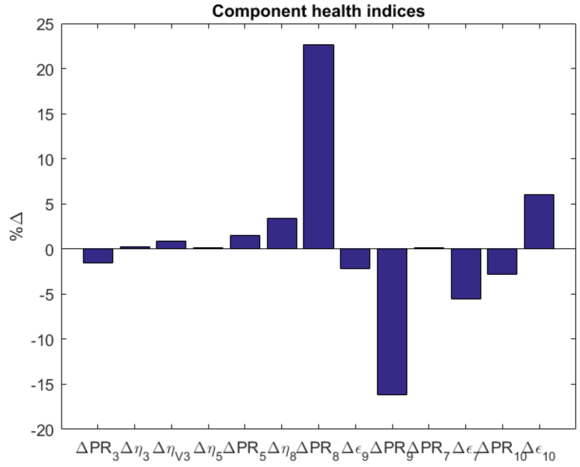

Figure 5-1: Index deviations (case 1).

Figure 5-1 shows the index deviations that were obtained for all the components in the ORC system. The deviations from left to right are the pressure ratio, isentropic efficiency and volumetric efficiency of the pre-feed pump, isentropic efficiency and pressure ratio across the main pump, isentropic efficiency and pressure ratio across the turbine, effectiveness and pressure ratio across the recuperator, pressure ratio and effectiveness of the evaporator and the pressure ratio and effectiveness of the condenser. At first glance, the deviation plot points to the turbine pressure ratio (+23% deviation) as the main source of the problem. Furthermore, the pressure ratio across the hot side of the recuperator shows a negative deviation, and the pressure ratio across the main pump and pre-feed pump shows very slight negative and positive deviations respectively.

However, deviations in the pressure ratio across the turbine and hot side of the recuperator seem to be interrelated. Additionally, Equation 3-60 shows that the design pressure drops in the recuperator and condenser influence the pressures and thus could be the reason for such high deviations in the pressure ratios obtained in the diagnostic results. If the pressure drops in the condenser and hot side of the recuperator are made to match for the model and active ORC, the deviation pattern shown in Figure 5-2 is obtained.

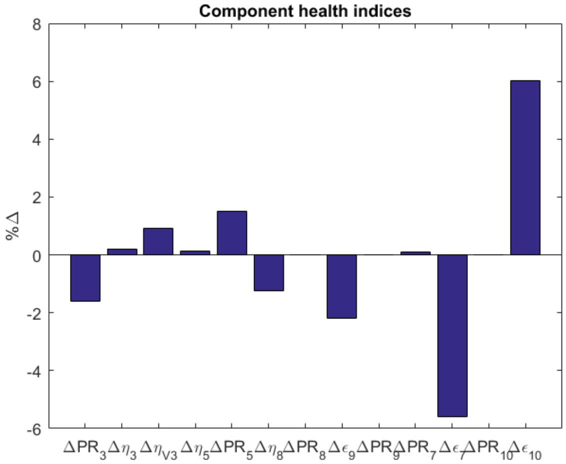

Figure 5-2: Index deviations after first tuning (case 1).

It can be seen that the pressure ratio deviations of the turbine and hot side of the recuperator are now eliminated whilst the other deviations maintain their previous values except that of the turbine isentropic efficiency, which becomes negative. Furthermore, the highest index deviation is now only 6%, which occurs for the condenser effectiveness, followed by the evaporator effectiveness, which is slightly less.

The deviations in the condenser and evaporator effectiveness are most likely due to the deviation in the recuperator effectiveness. A lower recuperator effectiveness would affect the exit temperatures at the hot and cold side of the recuperator, which are the inlet temperatures for the evaporator and condenser. Furthermore, the other minor deviations likely because of rounding off errors since this condition monitoring tool makes use of many mathematical formulas. To strengthen this hypothesis even further, if we make the recuperator effectiveness of the model and active engine match, we obtain the results shown in Figure 5-3.

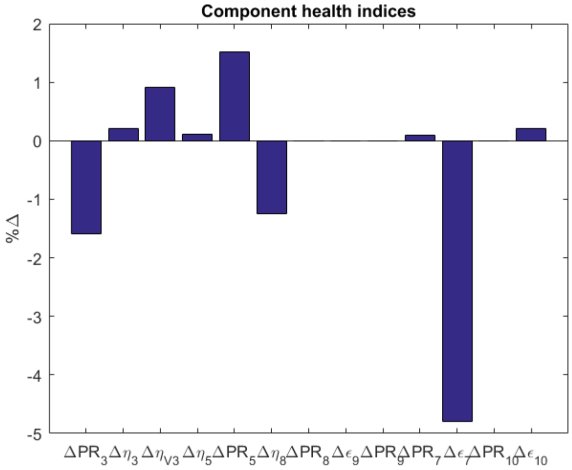

Figure 5-3: Index deviations after second tuning (case 1).

Figure 5-3 shows that the deviation in evaporator effectiveness reduces but is still significant. The temperature at the exit of the cold side of the recuperator (control point 6) is responsible for this deviation because the evaporator effectiveness is a function of the inlet and outlet temperature of the flue gas and the temperature at control point 6. Thus, there is most likely a significant amount of heat loss because of material degradation in that section. A look at Figure 5-4 shows that this is the case.

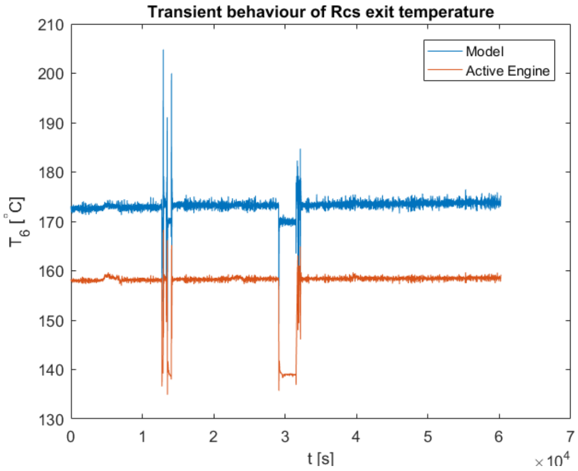

Figure 5-4: Exit temperature at cold side of the recuperator (case 1).

Figure 5-4 shows that the model predicts the temperature to be around 10% more than the value obtained from the sensor. If the temperature at control point 6 is made to match for the engine and model, the deviations shown in Figure 5-5 are obtained.

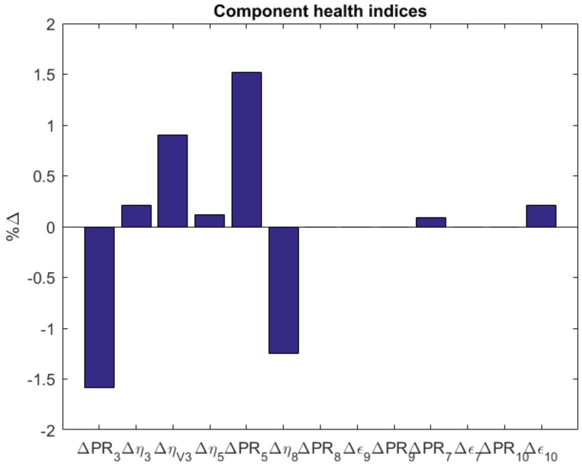

Figure 5-5: Index deviations after third tuning (case 1).

After tuning, the highest deviations now occur for the pressure ratio across the pre-feed pump and main pump. Furthermore, observing the thermophysical properties at the inlet and outlet of both components revealed the cause to be because of the pressure at the pre-feed pump exit. Making the pressure at the exit of the pre-feed pump to match for the model and active ORC yields the deviations shown in Figure 5-6.

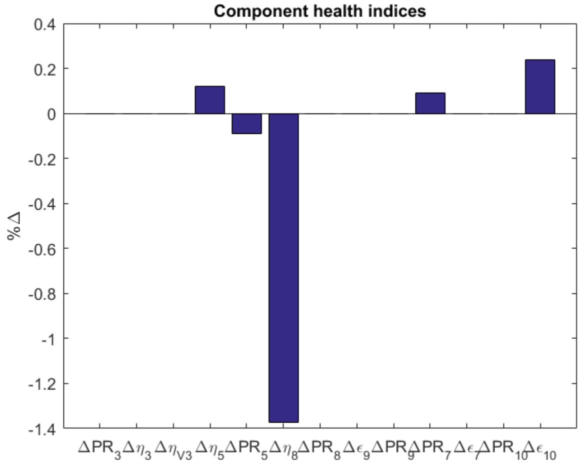

Figure 5-6: Index deviations after fourth tuning (case 1).

From Figure 5-6, it can be seen now that the deviations are minimal after tuning. Furthermore, the deviation observed for the turbine isentropic efficiency is due to approximation errors. The exit properties of the turbine influence the efficiency and because of the huge pressure ratio across the turbine, error due to approximations are inevitable. In addition, the other minor deviations are because of smearing effects due to approximations from the other components.

In summary, the condition monitoring tool has been applied to an active engine and the results have been presented. The parameters that were tuned to arrive at the final state, which is shown in Figure 5-6, are the pressure drops in the hot side of the recuperator and condenser, the recuperator effectiveness, the exit temperature at the cold side of the recuperator, and the pressure at the exit of the pre-feed pump. The pressure drops in the condenser and evaporator can arguable be determined inconsequential because they are component design specifications; also, the pressure drops are less than assumed by the model so they are within the allowable pressure drop. However, exit pressure of the pre-feed pump and exit temperature of the cold side of the recuperator are critical parameters since they are calculated. Thus, assuming all sensor readings correct for this case, there is either some leakage in the pre-feed pump probably due to the seals or some degradation of its impeller due to erosion and there is some fouling in the section between the cold side of the recuperator and the evaporator. Furthermore, an observation of the recuperator effectiveness for the active ORC reveals an obvious deterioration occurred over the period observed (Figure 5-7).

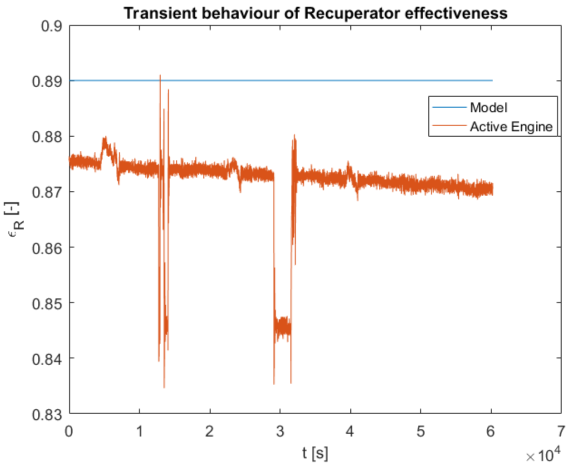

Figure 5-7: Recuperator effectiveness (case 1).

This deterioration though gradual has a significant effect on the system performance as was shown in the deviation charts in Figure 5-1. Furthermore, from the trend in Figure 5-7, it is obvious that this deterioration had been developing over time. Therefore, we can say there is some degree of material degradation (in this case fouling) in the cold side of the recuperator, which caused the negative deviation for the evaporator effectiveness and the positive deviation for the condenser effectiveness.

5.2 Case 2

For this second case, the data considered is for a different ORC over a period of six weeks. Fault diagnostics was run to assess the ORC performance and the results, describing the state of the ORC system at the end of the duration considered, are presented and discussed. Again, it is important to note that there are no archived data for the pre-feed pump exit temperature and condenser exit temperature or pressure. Therefore, the properties of the working fluid in the storage vessel has been assumed to be the condensing pressure and temperature while the pre-feed pump exit temperature was computed using pump curves and sensor readings for the active engine.

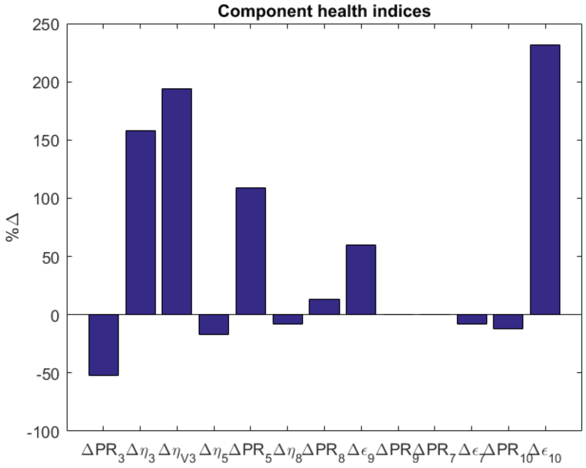

Figure 5-8: Index deviations (case 2).

Figure 5-8 shows the index deviations that were obtained for all the components in this ORC system. The deviations from left to right are the pressure ratio, isentropic efficiency and volumetric efficiency of the pre-feed pump, isentropic efficiency and pressure ratio across the main pump, isentropic efficiency and pressure ratio across the turbine, effectiveness and pressure ratio across the recuperator, pressure ratio and effectiveness of the evaporator and the pressure ratio and effectiveness of the condenser. The bar graph points to the condenser effectiveness as the health index with the largest deviation. In addition, the volumetric and isentropic efficiencies of the pre-feed pump and the pressure ratio of the main pumps shows strong positive deviations while the pressure ratio across the pre-feed pump shows a negative deviation. The condenser effectiveness of the pre-feed pump for the actual engine is almost 250% more than that of the model, which reveals that there must be some issue with the temperature at the exit of the hot side of the recuperator. Upon thorough investigation, the root cause showed an error in the sensor reading for this temperature compared to that estimated by the model (Figure 5-9).

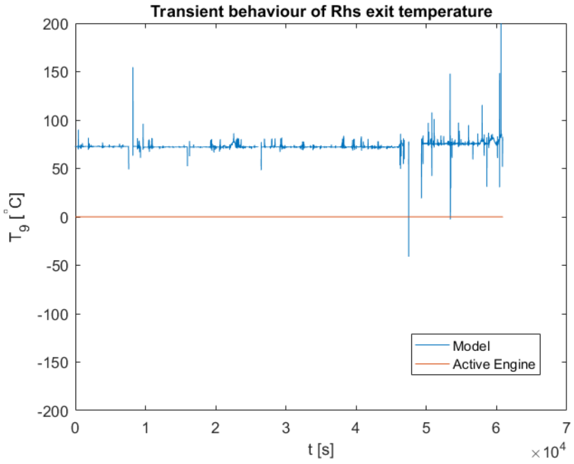

Figure 5-9: Exit temperature at the hot side of the recuperator (case 2).

The temperature sensor did not collect any results. Thus, allowing the sensor reading for the active engine assume the value of the model yields the result in Figure 5-10.

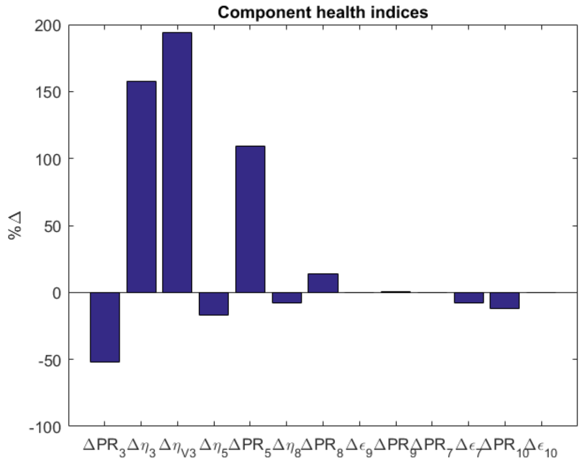

Figure 5-10: Index deviations after first tuning (case 2).

What can be observed in Figure 5-10 is that as well as the deviation in the condenser effectiveness being nullified, the deviation in recuperator effectiveness has been greatly reduced. Furthermore, the largest deviations are now occurring in the volumetric and isentropic efficiencies of the main pump and the pressure ratio across the main and pre-feed pumps. The large deviation in the volumetric efficiency of the pre-feed pump indicates that the head delivered by the pre-feed pump is lower than that predicted by the model. An inspection of the plot for the pressure at the pre-feed pump exit yields the result in Figure 5-11.

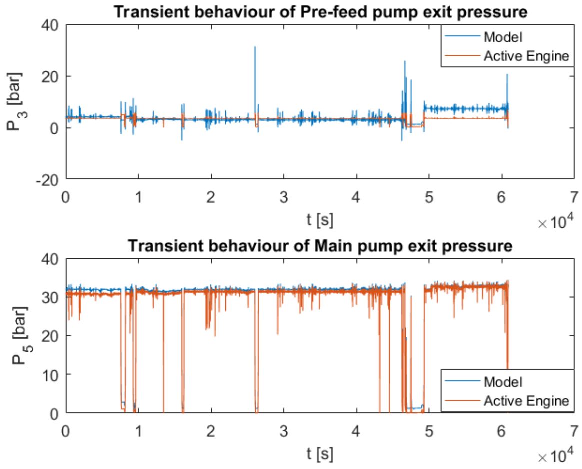

Figure 5-11: Pre-feed and main pump exit temperatures (case 2).

From Figure 5-11, it can be observed that the pressure at the main pump exit of the active ORC is similar to that of the model whereas that of the pre-feed pump is lower. Furthermore, this difference in pre-feed pump pressure lasts for almost three hours so the initial suspicion of a fault in the pre-feed pump is confirmed. If the pressure at the exit of the pre-feed pump for the model is tuned to match that of the active ORC, the deviations shown in are obtained.

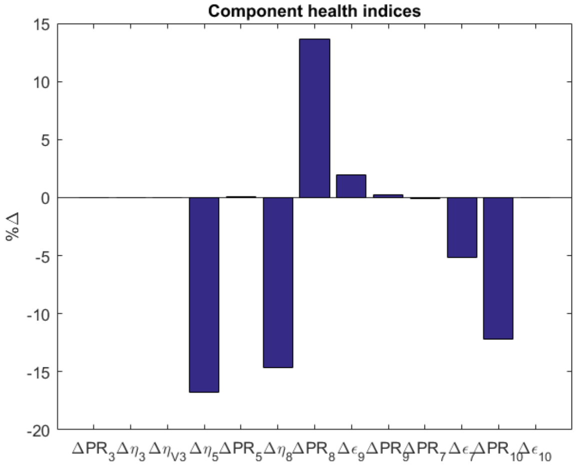

Figure 5-12: Index deviations after second tuning (case 2).

The health indices with the highest deviation are now the main pump isentropic efficiency, the turbine isentropic efficiency and the turbine pressure ratio. Furthermore, upon observation of the turbine and main pump thermophysical properties, the temperature at the turbine and main pump exit turned out to be higher than that predicted by the model. The pressure and temperatures influence the isentropic efficiencies of the main pump and turbine; however, observations showed that the temperatures rather than the pressure are responsible for this deviation. This pattern points to possible excess heat in these components; moreover, the main pump, turbine and generator are mounted on the same shaft in a hermetically sealed casing; thus, insufficient cooling within the casing would be evident on both outlets. Moreover, observations from the sensor readings showed a steady rise in the temperature of the electrical stator and bearings prior to the end of the period considered. Figure 5-13 shows this observation and it can be clearly seen that the bearing temperature influences the main pump exit temperature.

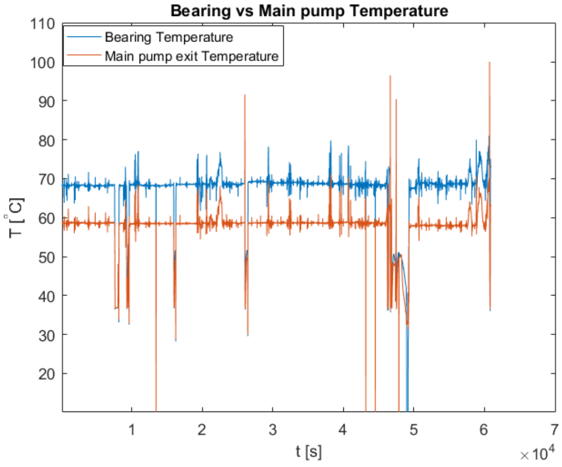

Figure 5-13: Bearing vs Outlet temperature of Main pump (case 2).

Nevertheless, these deviations in Figure 5-12 indicates that the actual engine underperforms; hence, it is safe to say that the enthalpies at the exit of the main pump and turbine of the active engine are responsible. If the temperatures at the exit of the main pump and turbine for the model are tuned to match that of the active ORC, the results in Figure 5-14 are obtained.

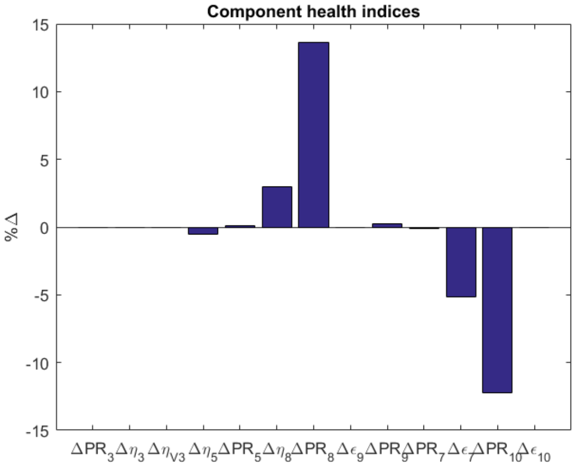

Figure 5-14: Index deviations after third tuning (case 2).

In Figure 5-14, the health indices with the highest deviation are the condenser pressure ratio, turbine pressure ratio and the evaporator effectiveness. Recall that in the previous case (section 5.1), the pressure drops in the heat exchangers for the model was tuned to that of the active engine to eliminate the pressure ratio deviations; also, because the thermophysical properties at the exit of the evaporator are control variables, the cause of the deviation in the evaporator effectiveness is the evaporator inlet temperature. Moreover, the recuperator effectiveness has been kept at the design value. Thus, if the pressure at the exit of the turbine and hot side of the recuperator for the model are tuned to that of the active ORC alongside the evaporator inlet temperature (control point 6), the result in Figure 5-15 is obtained.

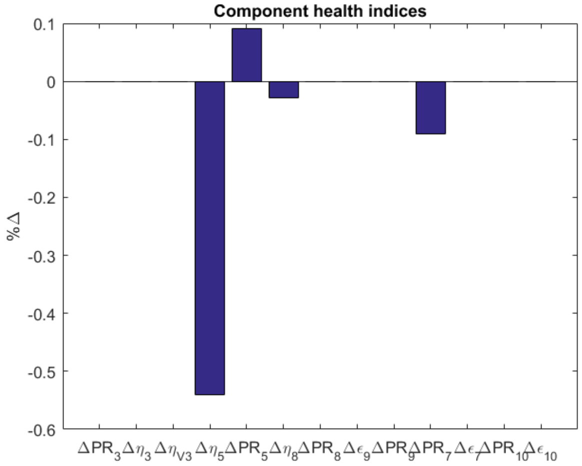

Figure 5-15: Index deviations after fourth tuning (case 2).

In Figure 5-15, it can be seen that the deviations are minimal due to the tuning. These deviations are less than 1% and are likely a result of approximations in the model; thus, they can be assumed negligible.

In summary, the condition monitoring tool has been applied to an active engine and the results have been presented. The parameters that were tuned to arrive at the final state, which is shown in Figure 5-15, are the pressure at the exit of the pre-feed pump, pressure at the condenser inlet, temperature at the exit of both sides of the recuperator, exit temperature of the main pump and the exit pressure and temperature of the turbine. The deviation due to the temperature at the exit of the hot side of the recuperator is confirmed to be because of sensor error. However, the exit pressure of the pre-feed pump, exit temperature of the turbine, exit temperature of the main pump and exit temperature of the cold side of the recuperator are critical parameters since they are calculated. Thus, assuming all sensor readings correct for this case, there is either a huge amount of leakage in the pre-feed pump probably due to the seals or a serious deterioration of the pump impeller probably due to erosion. As for the temperatures at the exit of the turbine and main pump, there is possibly insufficient cooling in the container housing the main pump, shaft and turbine. Finally, the exit temperature deviation at the cold side of the recuperator signifies fouling in the cold side.

6 Final remarks

The present research was aimed at developing a robust condition monitoring tool for the Triogen ORC system so as to be able to detect and isolate component faults based on fluid thermophysical property trends. In doing so, a surrogate baseline model was created to be able to account for variations in operating conditions during fault diagnosis. In addition, failure modes were simulated for each component and the performance trends were observed and recorded.

Section 6.1 summarises the findings in the validation and performance of the condition monitoring tool, section 6.2 answers the research questions initially posed and section 6.3 presents the main contributions of this research. From the findings, section 6.4 discusses the limitations to this research and section 6.5 discusses the proposed recommendations.

6.1 Main findings

In validating the condition monitoring tool, two cases were considered and diagnosis was performed using Matlab. The condition monitoring tool is an equation based model; so, a programming script, containing the system equations structured according to the computation algorithm, was developed in Matlab to represent the GTPtracker software.

The important aspects considered were ease of application and effectiveness of the condition monitoring tool. Concerning the ease of application, the user only needs to load the sensor data into Matlab using .txt files and run the code to get the diagnostic results. Furthermore, the results obtained in both cases were sufficient and fault prognosis was an easy and straightforward process. However, in both cases, because the pressure drops in the heat exchangers were classified as component design specifications (i.e. assumed constant), component pressure ratios that were dependent on these heat exchanger pressure drops showed some deviation. Therefore, it is difficult to identify actual pressure ratio deviations in components whose inlet or exit pressures are influenced by these pressure drops because they are assumed constant. Nevertheless, the most likely faults that can occur in the heat exchangers are easily identifiable from temperature patterns.

6.2 Answers to research questions

In this section, the formulated research questions are answered based on the results obtained and the observations made during the course of the research. In the answers provided, the sub-questions, which define the main questions, are addressed to provide answers to the general question.

1. *Which condition monitoring technique should be selected for the Triogen ORC system?*

From the literature study, the final conclusion based on the requirements for an online condition monitoring tool revealed that the non-linear GPA method was the most ideal. The non-linear GPA technique was found to employ thermodynamic relations, which is desirable for any condition monitoring tool. In addition, it is not as complex as the other GPA techniques and has an acceptable computation time as well as a good degree of accuracy. However, a direct application of the non-linear GPA technique is not possible because the GTPtracker does not support iterative processes; thus, a unique non-linear method was developed to configure the GTPtracker for the Triogen ORC system whilst maintaining robustness. Furthermore, the non-linear method that was developed is presented in the main part of this research alongside the steps to be taken for proper implementation.

2. *How should component health parameters be derived and corrected for ORC condition monitoring?*

   As shown in the research, existing component performance indices can be adopted for the Triogen system. Performance indices for all the components in the Triogen system are readily available from literature. However, due to the unavailability of some key parameters, some of the performance indices had to be modified in order to obtain a means of assessing their performance. An example is the heat exchanger effectiveness where a modification was introduced in order to express it only as a function of the inlet and outlet temperatures.

   In addition, because the surrogate model was developed as an exact model, there was no need for component condition parameter corrections. Furthermore, it is possible to assess the condition of all the components simultaneously unlike in the widely known non-linear GPA technique where sensitivity analysis had to be carried out to determine the condition parameters that were most affected because of a fault.

3. *How can engine component faults be identified and isolated for the Triogen ORC system?*

   In this research, every component of the condition monitoring tool was discussed in detail. Upon development of the surrogate model, deterioration modes were simulated for each component and the effect on the system thermophysical parameters as well as the other components health parameters were observed and recorded in form of fault tables. These fault tables are to serve as a guide for the user in selecting which parameters should be included in the ruleset for any particular fault unique to a component. Furthermore, the deterioration modes that were simulated give a good indication of the limits of each component with respect to a deterioration in any one component; thus serving as a guide in defining tolerance limits for each component in the rulesets.

   Sensor errors are easily determined through observation of the thermophysical property trends at each of the control points as demonstrated in section 5.2. The fault tables give an indication of which thermophysical parameters are affected for a particular fault and if that parameter is unchanged after the fault has been tolerated then the most likely reason is a sensor malfunction.

4. *How can the condition monitoring tool be checked for robustness?*

   The best method that can be utilised in validating a model is by testing it with real life data. Referring to sections 5.1 and 5.2, real data was diagnosed with the condition monitoring tool that was developed in this research and a thorough analysis was provided alongside the final prognosis. This is evidence enough that the tool is robust and capable of detecting and isolating component faults.

6.3 Main contributions

This research has not only successfully developed a robust condition monitoring tool for Organic Rankine Cycle systems but has also succeeded in introducing a new and efficient method of developing off-design models for thermodynamic systems. Conventional off-design models are either assumption based which draws the penalty of low accuracy or employ advanced modelling techniques with the penalty of an increased computation time. However, this research has succeeded in creating an off-design model with minimal assumptions, fast computation time and accurate results. In the cases considered during the validation of the model, about 61000 data points were processed in less than 11 seconds thus giving an average of about 5,545 data points per second. To provide a better indication of the importance of these numbers, each data point represents a sensor measurement taken in a second; thus, the condition monitoring tool is more than capable of analysing and producing results in real time.

6.4 Limitations

The only limitation to this research is that the fluid property model will tend to over predict, under predict or not predict at all the component thermophysical properties outside the component operating range because the fluid property model is designed for maximum accuracy within the bounds of the component operating range. An example is presented in Figure 6-1.

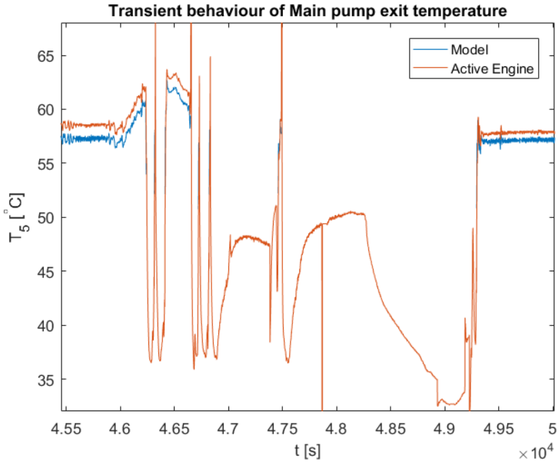

Figure 6-1: Surrogate vs Active engine for Main pump exit temperature

The plot in Figure 6-1 shows a case where the model fails to predict the temperature at the main pump exit. The reason for this is because in the fluid property model, the main pump is designed to operate between a range of 50℃ to 80℃ thus making it impossible to predict temperatures outside this range.

6.5 Practical recommendations

In this research, a major difficulty was encountered in developing a dynamic model for the turbine and main pump. The reason for this is that they are developed in-house and thus uncharacterised. However, characterising the turbine and main pump would not only improve the model but also introduce the possibility of eliminating some sensors in the Triogen system. An example is the pre-feed pump where only the pressure is measured at the outlet. Without a performance map for the pre-feed pump it would have been impossible to define the properties at the outlet for the active engine and thus assumptions would have had to be made. Nevertheless, without the temperature sensor, the performance maps provided by the manufacturer was utilised in determining the temperature analytically and thus the pre-feed pump condition could be assessed.

Furthermore, because of the problems encountered as a result of selecting a constant value for the pressure drop in the hot side of the recuperator, future research should be directed towards developing accurate pipe loss models. At the moment, the loss models that can be developed for the system will be inaccurate because of the mass flow assumptions in the system. If the turbomachinery components are characterised, better estimation of the system mass flow will be possible; thus, better loss models can be developed.

References

1. Triogen, *Sales argument and information*. 2012: Goor, Netherlands.
2. B&B Agema GmhB, *Gas Turbine Tracker presentation*. Aachen, Germany.
3. Verbiest M.L, *Gas Path Analysis for enhanced aero-engine condition monitoring and maintenance*, in *Process and Energy Technology*. 2017, Delft University of Technology: Delft, Netherlands. p. 158.
4. Escher, P., *Pythia: An object-orientated gas path analysis computer program for general applications*. 1995.
5. Urban, L.A., *Gas path analysis applied to turbine engine condition monitoring*. Journal of Aircraft, 1973. **10**(7): p. 400-406.
6. Dixon, S.L. and C. Hall, *Fluid mechanics and thermodynamics of turbomachinery*. 2013: Butterworth-Heinemann.
7. Thulukkanam, K., *Heat exchanger design handbook*. 2013: CRC Press.
8. Volponi, A.J., *Gas turbine parameter corrections*. TRANSACTIONS-AMERICAN SOCIETY OF MECHANICAL ENGINEERS JOURNAL OF ENGINEERING FOR GAS TURBINES AND POWER, 1999. **121**: p. 613-621.
9. Kaboukos, P., et al., *Optimizing diagnostic effectiveness of mixed turbofans by means of adaptive modelling and choice of appropriate monitoring parameters*. 2003, NATIONAL TECHNICAL UNIV ATHENS (GREECE) LAB OF THERMAL TURBOMACHINES.
10. Li, Y., *Performance-analysis-based gas turbine diagnostics: A review*. Proceedings of the Institution of Mechanical Engineers, Part A: Journal of Power and Energy, 2002. **216**(5): p. 363-377.
11. Stamatis, A. and K. Papailiou. *Discrete operating conditions gas path analysis*. in *AGARD conference proceedings*. 1988. AGARD.
12. Urban, L.A., *Gas turbine engine parameter interrelationships*. 1969: Hamilton Standard Division of United Aircraft Corporation.
13. Visser, W.P.J., *Generic Analysis Methods for Gas Turbine Engine Performance: The development of the gas turbine simulation program GSP*. 2015.
14. Stamatis, A., et al., *Gas turbine component fault identification by means of adaptive performance modeling*. ASME paper, 1990(90-GT): p. 376.
15. Stamatis, A., K. Mathioudakis, and K. Papailiou, *Adaptive simulation of gas turbine performance*. Journal of engineering for gas turbines and power, 1990. **112**(2): p. 168-175.
16. Bettocchi, R. and P. Spina, *Diagnosis of gas turbine operating conditions by means of the inverse cycle calculation*. ASME paper, 1999(99-GT): p. 185.
17. Biagioni, L., R. Cinottf, and L. d'Agostino, *Turboshaft engine condition monitoring by Bayesian identification*. Ahsiracfésmggv ISABE, 2001: p. 29.
18. Chen, D. and Z. Zhu, *Model identification-based fault analysis method applied to jet engines*. Proceedings of 15th ISABE, 2001.
19. Consumi, M. and L. d'Agostino. *Monitoring and fault diagnosis of a turbojet by Bayesian inference*. in *ISABE- International Symposium on Air Breathing Engines, 13 th, Chattanooga, TN*. 1997.
20. Consumi, M.a.d.A., L., *A statistical inference approach to gas path analysis of a turbofan*. The american institute of Aeronautics and Astronautics (AIAA), 1998. **98**(3551).
21. Lambiris, B., et al., *Adaptive modeling of jet engine performance with application to condition monitoring*. Journal of propulsion and power, 1994. **10**(6): p. 890-896.
22. Mathioudakis, K. and K. Papailiou, *Optimal measurement and health index selection for gas turbine performance status and fault diagnosis*. Journal of engineering for gas turbines and power, 1992. **114**: p. 209.

23. Navez, A. and T. Aero, *Engine physical diagnosis using a robust parameter estimation method.* 2001.
24. Santa, I. *Diagnostics of gas turbine engines based on thermodynamic parameters*. in *6th Mini Conference on Vehicle System Dynamics, Identification and Anomalies*. 1998.
25. Tsalavoutas, A., et al. *Monitoring the performance of a twin-shaft ship propulsion turbine by means of adaptive modeling*. in *RTO symposium on gas turbine operation and technology for land, sea and air propulsion and power systems, Ottawa, Canada*. 1999.
26. Zedda, M. and R. Singh, *Gas turbine engine and sensor fault diagnosis using optimization techniques.* Journal of propulsion and power, 2002. **18**(5): p. 1019-1025.
27. Singh, R., *Advances and opportunities in gas path diagnostics.* 15th ISABE, Paper No. ISABE-2003-1008, 2003.
28. Gulati, A., M. Zedda, and R. Singh. *Gas turbine engine and sensor multiple operating point analysis using optimization techniques*. in *36th AIAA/ASME/SAE/ASEE Joint Propulsion Conference and Exhibit*. 2000.
29. Fonseca, C.M. and P.J. Fleming. *Genetic Algorithms for Multiobjective Optimization: FormulationDiscussion and Generalization*. in *Icga*. 1993.
30. rey Horn, J., N. Nafpliotis, and D.E. Goldberg, *Multiobjective optimization using the niched pareto genetic algorithm.* IlliGAL report, 1993(93005): p. 61801-2296.
31. Srinivas, N. and K. Deb, *Muiltiobjective optimization using nondominated sorting in genetic algorithms.* Evolutionary computation, 1994. **2**(3): p. 221-248.
32. Zhang, J. and P. Roberts, *On-line process fault diagnosis using neural network techniques.* Transactions of the Institute of Measurement and Control, 1992. **14**(4): p. 179-188.
33. Volponi, A.J., et al., *The use of Kalman filter and neural network methodologies in gas turbine performance diagnostics: a comparative study.* Journal of Engineering for Gas Turbines and Power(Transactions of the ASME), 2003. **125**(4): p. 917-924.
34. Zedda, M. and R. Singh. *Fault diagnosis of a turbofan engine using neural networks-A quantitative approach*. in *34th AIAA/ASME/SAE/ASEE Joint Propulsion Conference and Exhibit*. 1998.
35. Bin, S., Z. Jin, and Z. Shaoji, *An investigation of artificial neural network (ANN) in quantitative fault diagnosis for turbofan engine.* ASME paper, 2000(2000-GT): p. 32.
36. Eustace, R. and P. Frith, *Utilizing Repair and Overhaul Experience in a Probabilistic Neural Network for Diagnosing Gas-Path Faults.* ISABE Paper, 2001(2001-1050).
37. Eustace, R. and G. Merrington. *Fault diagnosis of fleet engines using neural networks*. in *ISABE-International Symposium on Air Breathing Engines, 12 th, Melbourne, Australia*. 1995.
38. Patel, V., et al. *Gas turbine engine condition monitoring using statistical and neural network methods*. in *Modeling and Signal Processing for Fault Diagnosis (Digest No.: 1996/260), IEE Colloquium on*. 1996. IET.
39. Romessis, C., A. Stamatis, and K. Mathioudakis, *A parametric investigation of the diagnostic ability of probabilistic neural networks on turbofan engines.* ASME paper, 2001(2001-GT): p. 0011.
40. Kohonen, T., *Self-organized formation of topologically correct feature maps.* Biological cybernetics, 1982. **43**(1): p. 59-69.
41. Roemer, M., *'Testing of a Real-Time Health Monitoring and Diagnostics System for Gas Turbine Engines.* Paper No. AIAA-98-3603, 1998.
42. Eustace, R. *Neural network fault diagnosis of a turbofan engine*. in *ISABE- International Symposium on Air Breathing Engines, 11 th, Tokyo, Japan*. 1993.
43. Kohonen, T., *Self-organization and associative memory*. Vol. 8. 2012: Springer Science & Business Media.
44. Hecht-Nielsen, R., *Nearest matched filter classification of spatiotemporal patterns.* Applied Optics, 1987. **26**(10): p. 1892-1899.
45. Torella, G. *Expert systems and neural networks for fault isolation in gas turbines*. in *ISABE-International Symposium on Air Breathing Engines, 13 th, Chattanooga, TN*. 1997.

46. Torella, G. and G. Lombardo. *Utilization of neural networks for gas turbine engines*. in *ISABE-International Symposium on Air Breathing Engines, 12 th, Melbourne, Australia*. 1995.
47. Arkov, V., et al., *Aircraft engine condition monitoring: stochastic identification and neural networks.* 1997.
48. Patel, V. and V. Kadirkamanathan. *Adaptive self-learning fault detection system for gas turbine engines*. in *9th International Conference: Condition Monitoring and Diagnostic Engineering Management, Sheffield, UK*. 1996.
49. Patel, V., V. Kadirkamanathan, and H. Thompson, *A novel self-learning fault detection system for gas turbine engines.* 1996.
50. Patel, V., et al., *Utilising a SIMULINK gas turbine engine model for fault diagnosis.* IFAC Proceedings Volumes, 1995. **28**(26): p. 237-242.
51. Patel, V., et al., *An intelligent fault diagnosis system for gas turbine engines.* Proc. of Aerotech, 1995. **95**.
52. Fahlman, S.E. and C. Lebiere. *The cascade-correlation learning architecture*. in *Advances in neural information processing systems*. 1990.
53. Jackson, P., *Introduction to expert systems.* 1986.
54. Doel, D.L. *The role for expert systems in commercial gas turbine engine monitoring*. in *ASME 1990 International Gas Turbine and Aeroengine Congress and Exposition*. 1990. American Society of Mechanical Engineers.
55. Pettigrew, J. *Effective turbine engine diagnostics*. in *AUTOTESTCON Proceedings, 2001. IEEE Systems Readiness Technology Conference*. 2001. IEEE.
56. Breese, J., et al. *Automated decision-analytic diagnosis of thermal performance in gas turbines*. in *Proceedings of the International Gas Turbine and Aeroengine Congress and Exposition, Cologne, Germany, American Society of Mechanical Engineers*. 1992.
57. Horvitz, E.J., J.S. Breese, and M. Henrion, *Decision theory in expert systems and artificial intelligence.* International journal of approximate reasoning, 1988. **2**(3): p. 247-302.
58. Mast, T.A., et al. *Bayesian belief networks for fault identification in aircraft gas turbine engines*. in *Control Applications, 1999. Proceedings of the 1999 IEEE International Conference on*. 1999. IEEE.
59. Palmer, C.A., *Combining Bayesian belief networks with gas path analysis for test cell diagnostics and overhaul.* ASME paper, 1998(98-GT): p. 168.
60. Pearl, J., *Probabilistic Reasoning in Intelligence Systems.* M organ æaufmann, áan M ateo, CA, 1988.
61. Romessis, C., A. Stamatis, and K. Mathioudakis, *Setting up a belief network for turbofan diagnosis with the aid of an engine performance model.* ISABE paper, 2001. **1032**: p. 19-26.
62. Moore, R.L. and M.A. Kramer, *Expert systems in on-line process control*. 1986: MIT.
63. Price, C. and M. Lee, *Applications of deep knowledge.* Artificial Intelligence in engineering, 1988. **3**(1): p. 12-17.
64. Dickes, R., et al., *Modelling of organic Rankine cycle power systems in off-design conditions: An experimentally-validated comparative study.* Energy, 2017. **123**: p. 710-727.
65. Saravanamuttoo, H.I.H., G.F.C. Rogers, and H. Cohen, *Gas turbine theory*. 2001: Pearson Education.

A Appendix

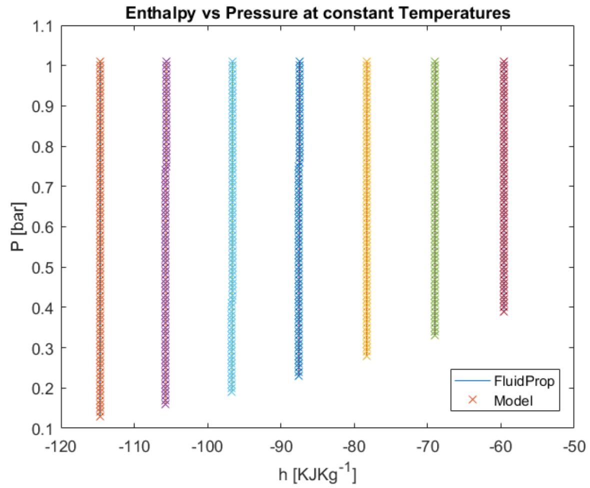

Figure A-1: Enthalpy storage vessel (Equation 3-13).

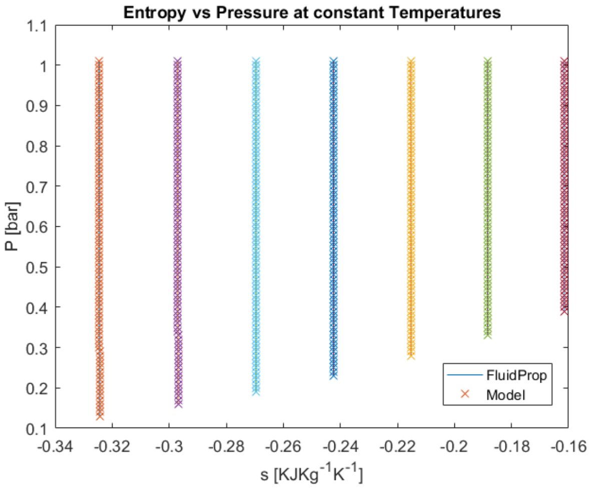

Figure A-2: Entropy storage vessel (Equation 3-14).

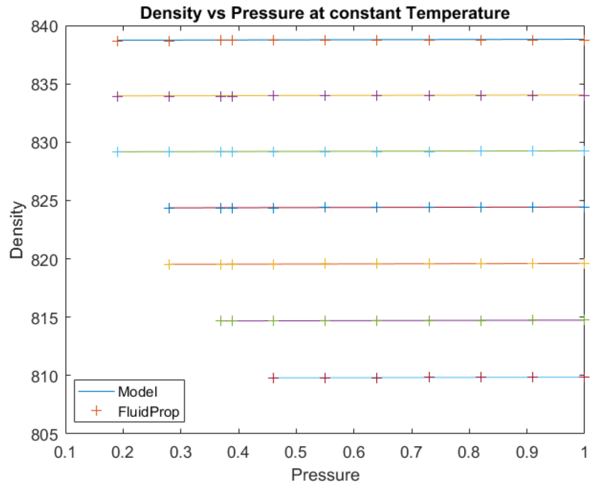

Figure A-3: Storage vessel Density (Equation 3-15).

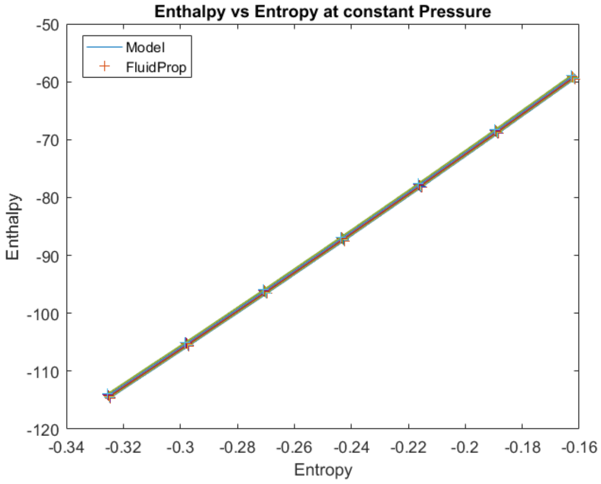

Figure A-4: Pre-feed pump Isentropic Enthalpy (Equation 3-17).

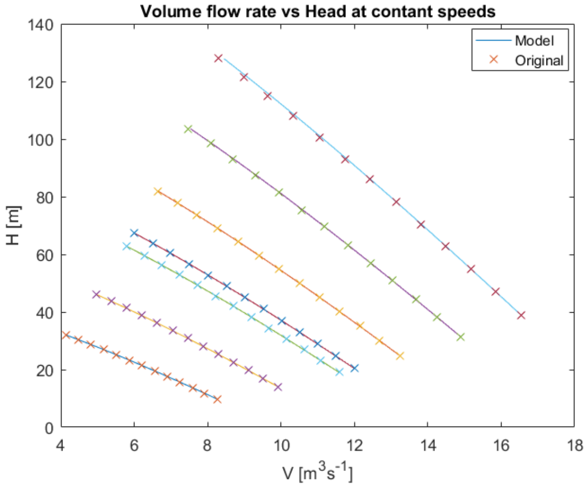

Figure A-5: Pre-feed pump volume flow rate (Equation 3-19**).**

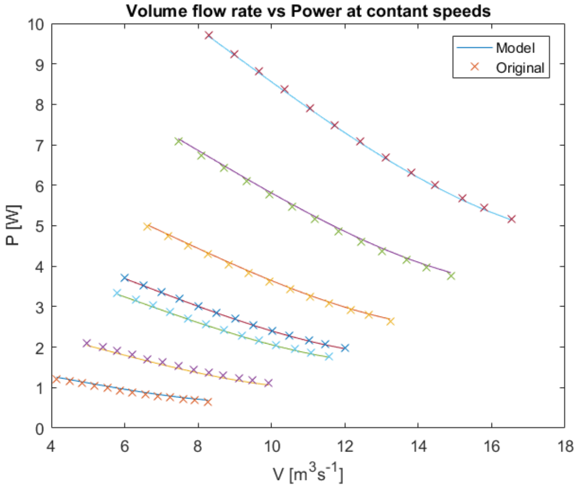

Figure A-6: Pre-feed pump power (Equation 3-20**).**

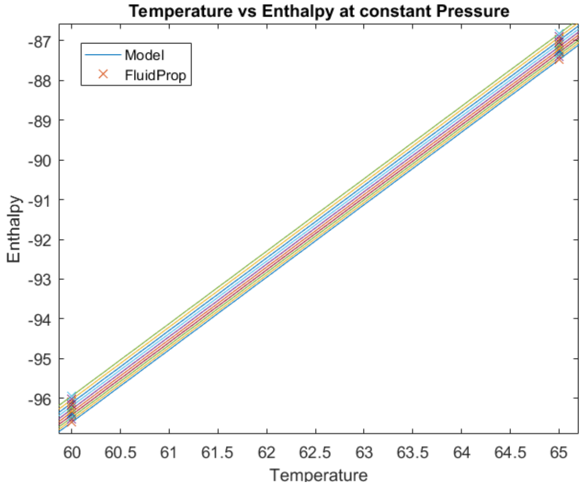

Figure A-7: Pre-feed pump Temperature (Equation 3-24).

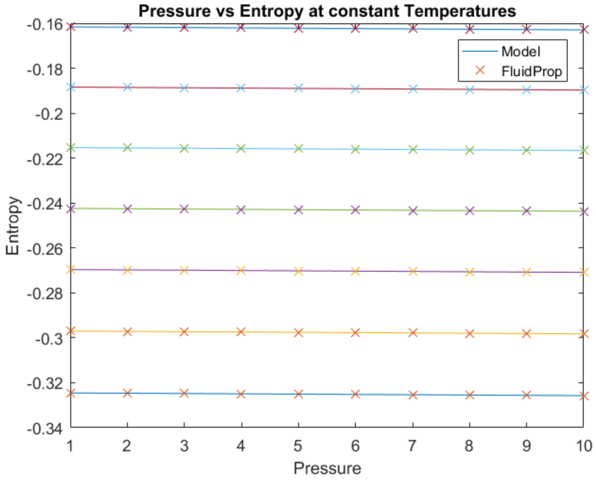

Figure A-8: Pre-feed pump Entropy (Equation 3-25).

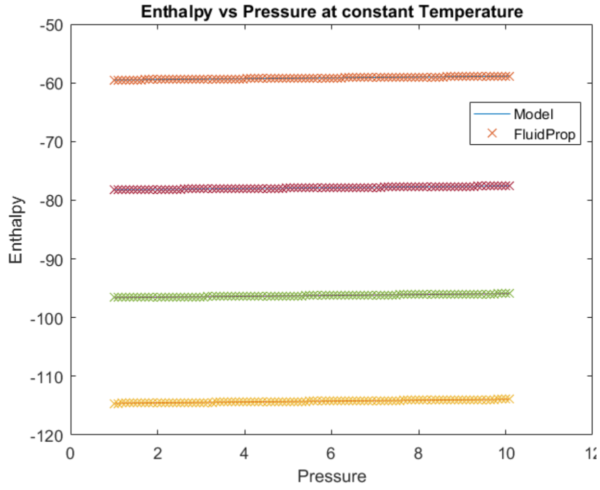

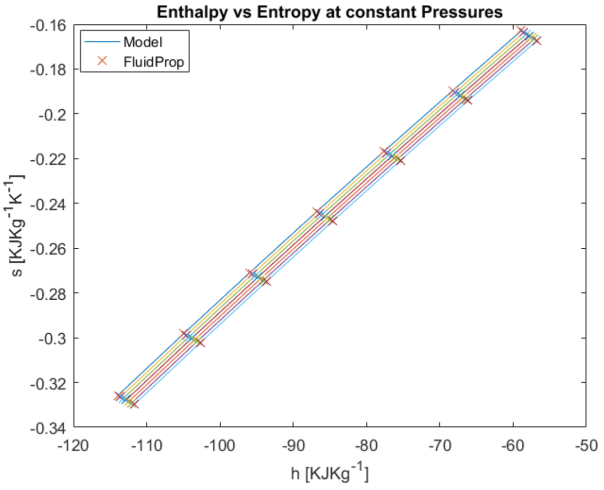

Figure A-9: Pre-feed pump Enthalpy (Equation 3-26).

Figure A-10: Main pump isentropic Enthalpy (Equation 3-28).

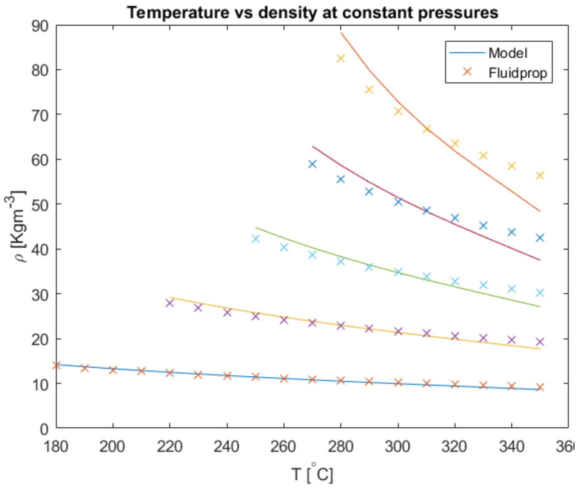

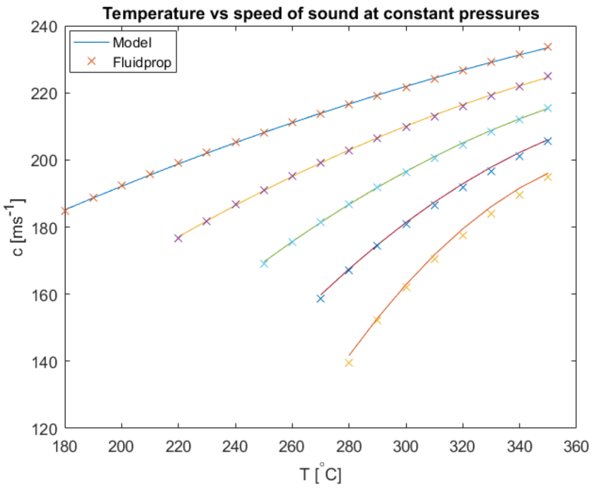

Figure A-11: Nozzle critical Density (Equation 3-30).

Figure A-12: Nozzle critical speed of sound (Equation 3-31).

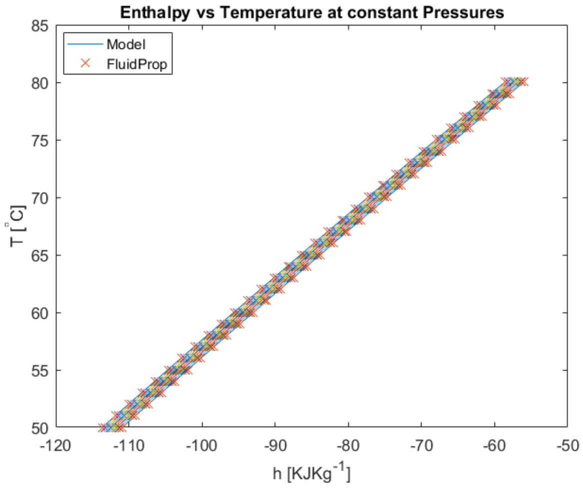

Figure A-13: Main pump Temperature (Equation 3-36).

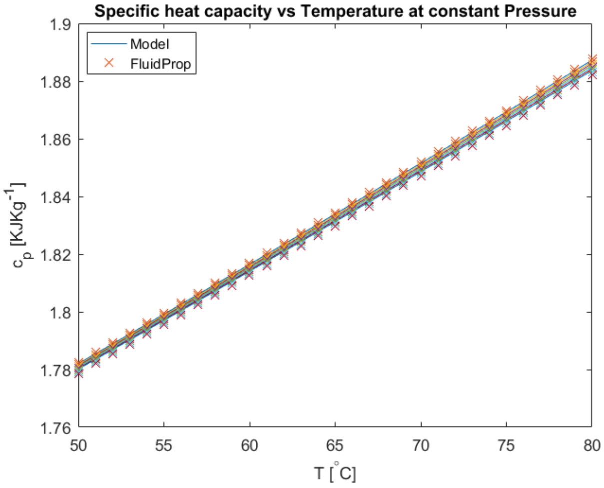

Figure A-14: Main pump specific heat capacity (Equation 3-37).

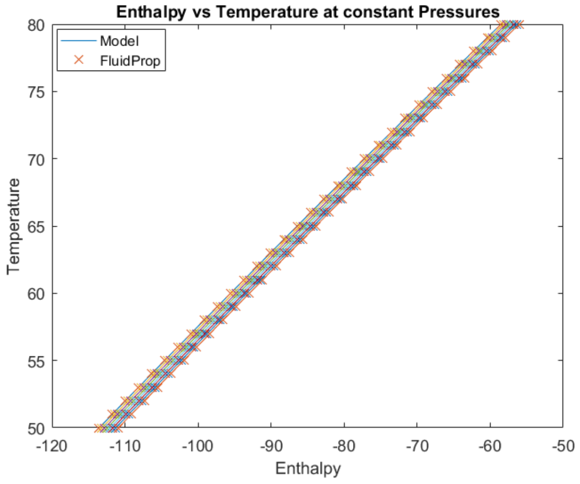

Figure A-15: Main pump Enthalpy (Equation 3-38).

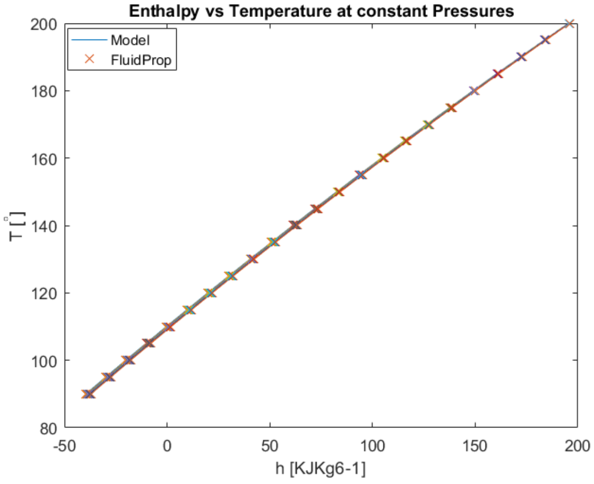

Figure A-16: Recuperator (cold side) Enthalpy (Equation 3-45).

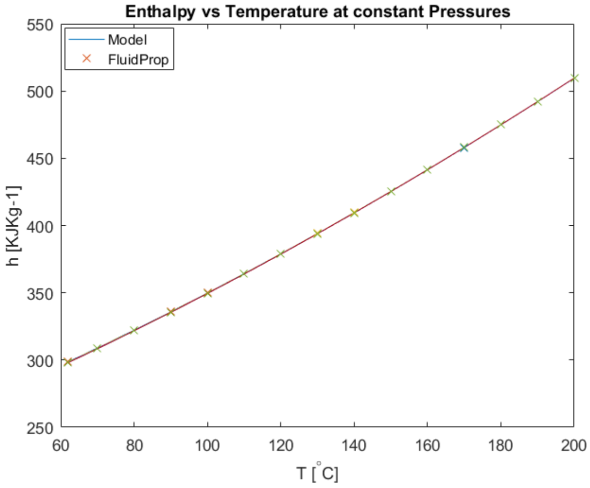

Figure A-17: Recuperator (hot side) Enthalpy (Equation 3-46).

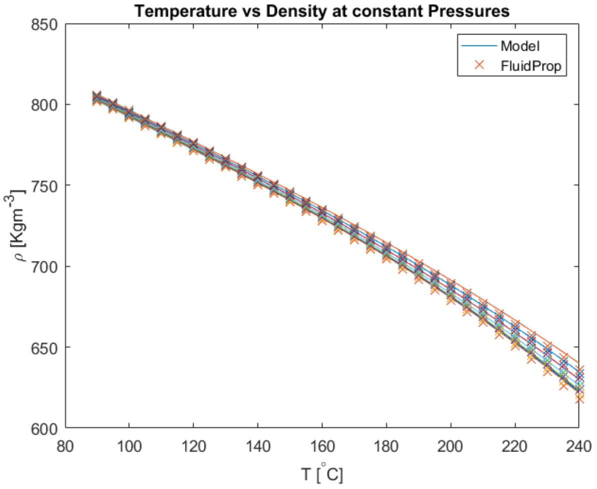

Figure A-18: Recuperator (cold side) Density (Equation 3-47).

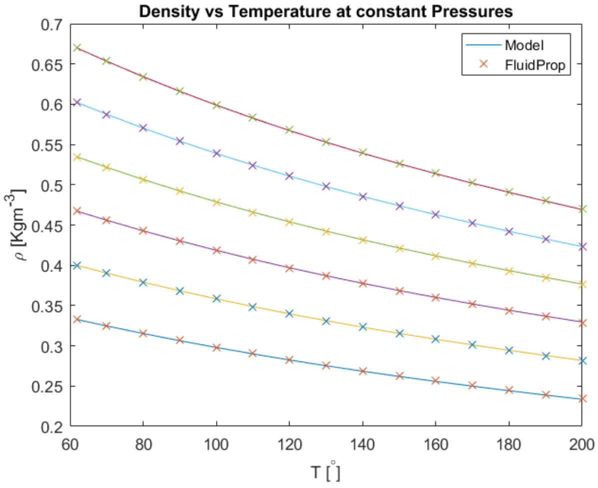

Figure A-19: Recuperator (hot side) Density (Equation 3-48).

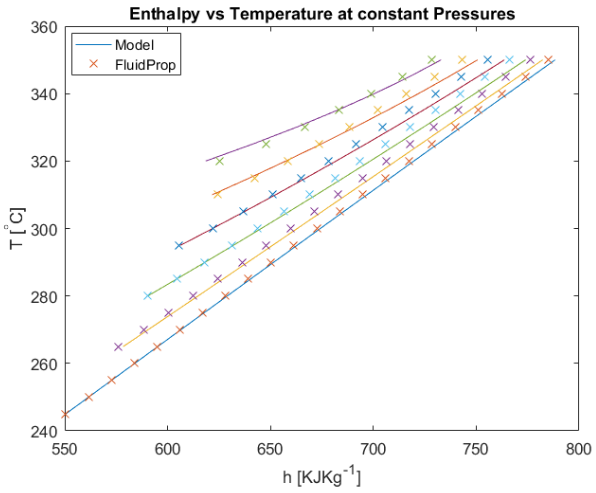

Figure A-20: Evaporator Enthalpy (Equation 3-49).

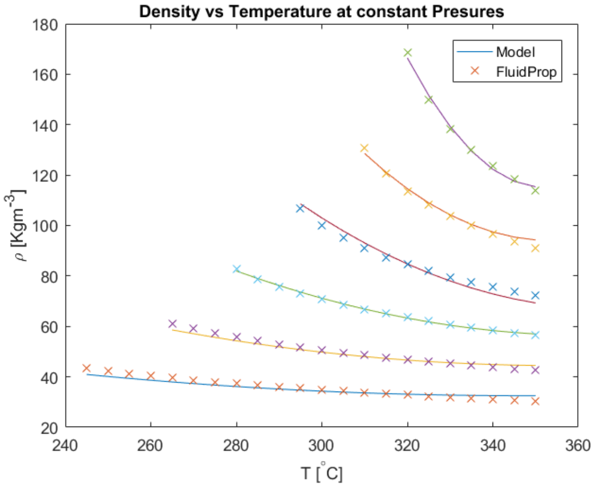

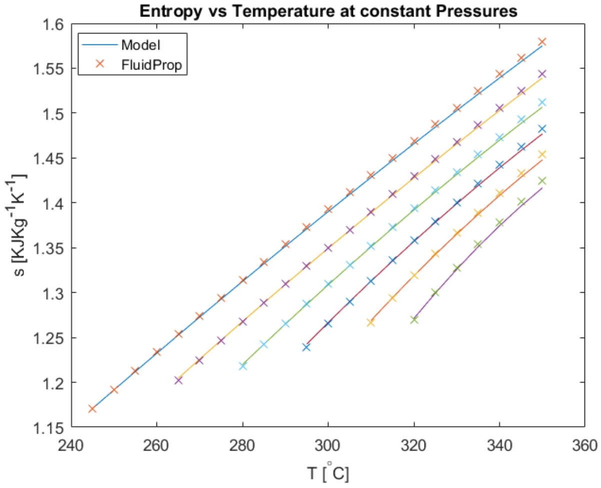

Figure A-21: Evaporator Density (Equation 3-50).

Figure A-22: Evaporator Entropy (Equation 3-51).

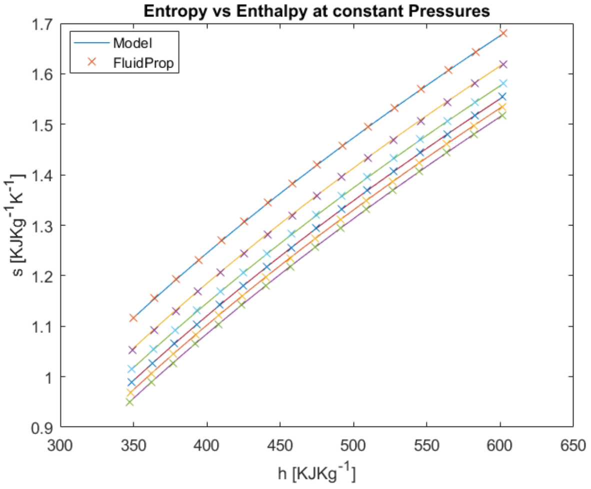

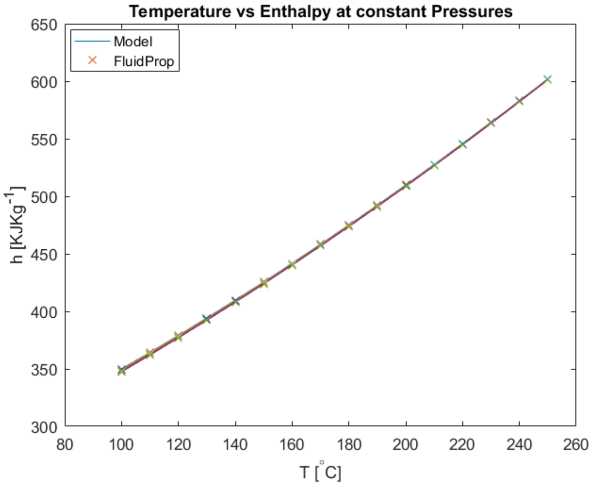

Figure A-23: Turbine isentropic Enthalpy (Equation 3-53).

Figure A-24: Turbine Temperature (Equation 3-56).

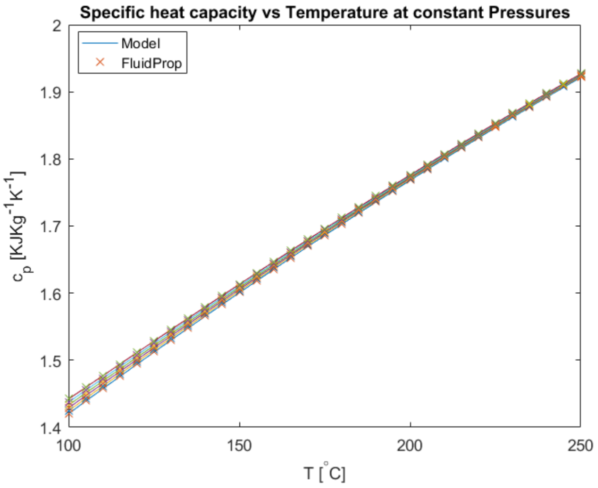

Figure A-25: Turbine specific heat capacity (Equation 3-57).

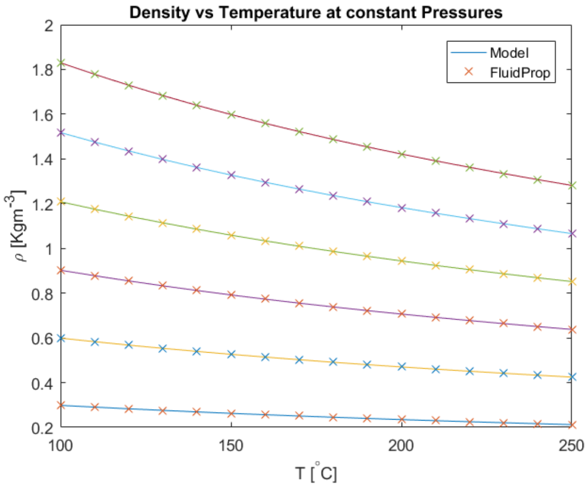

Figure A-26: Turbine Density (Equation 3-58).

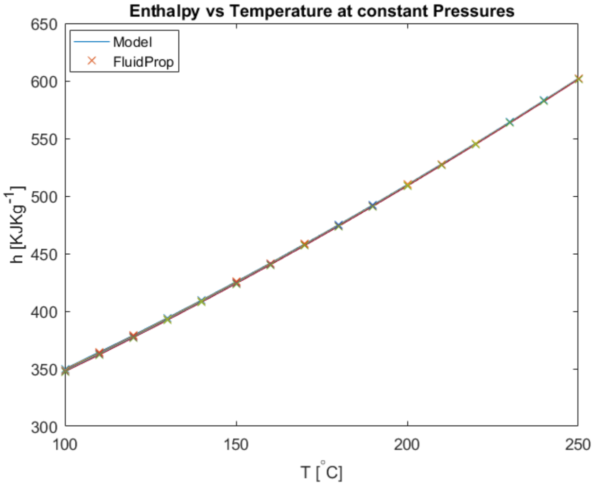

Figure A-27: Turbine Enthalpy (Equation 3-59).

```
close all
clear variables
clc

tic
%%Active ORC parameters
T7Eng = load('T7EngGTP5.txt');
T1Eng = load('T1EngGTP5.txt');
N5Eng = load('N5EngGTP5.txt');

P1Eng = load('P1EngGTP5.txt');
P3Eng = load('P3EngGTP5.txt');
P5Eng = load('P5EngGTP5.txt');
P7Eng = load('P7EngGTP5.txt');
P8Eng = load('P8EngGTP5.txt');
P9Eng = load('P9EngGTP5.txt');
T5Eng = load('T5EngGTP5.txt');
T6Eng = load('T6EngGTP5.txt');
T8Eng = load('T8EngGTP5.txt');
T9Eng = load('T9EngGTP5.txt');
TFIEng = load('TFIGTP5.txt');
TFOEng = load('TFOGTP5.txt');
TCIEng = load('TCIGTP5.txt');
TCOEng = load('TCOGTP5.txt');
PtGEng = load('PtGGTP5.txt');

for i = 1:length(T7Eng)

%%Matching (Key) parameters
T_7(i) = T7Eng(i);
T_1(i) = T1Eng(i);
P_1(i) = P1Eng(i);
N_5(i) = N5Eng(i);
PtG(i) = PtGEng(i);
P_7(i) = P7Eng(i);
%%Flue gas
TFI(i) = TFIEng(i);
TFO(i) = TFOEng(i);
TCI(i) = TCIEng(i);
TCO(i) = TCOEng(i);

%%Geometric parameters
A = (1.1*8.1*18)/1000000; %Nozzle throat area
D_5 = 0.056; %main pump impeller diameter in m
d_5 = 0.0046; %main pump discharge area in m. Two discharge holes
d_cond_in = 0.3556; %condenser inlet tube diameter in meters
d_cond_ex = 0.1143; %condenser exit tube diameter in meters

%%Component losses/parameters
psi_5 = 0.65; %ranges from 0.65-0.5  %%Selected design value%%
Recup_eff = 0.89;
g = 9.81;
N_3 = 1450; %Pre-feed pump speed in rpm
Pdrop_Rc = 0.386;%Cold side recuperator pressure drop
Pdrop_E = 0.544; %Evaporator pressure drop
Pdrop_c = 0.01;%Condenser pressure drop
Pdrop_Rh = 0.000594;%Hot side recuperator pressure drop

%%
    %%PRESSURE at Recup cold exit&MP exit
    P_6(i) = P_7(i) + Pdrop_E;
    P_5(i) = P_6(i) + Pdrop_Rc;
```

```
%%
   %%1 storage vessel exit
   h_1(i) = ((2.719e-09*T_1(i)^2) + (-8.269e-08*T_1(i)) + 9.318e-06)*P_1(i)^2 + ((-4.444e-09*T_1(i)^3) + (-1.714e-07*T_1(i)^2) + (-8.703e-05*T_1(i)) + 0.08099)*P_1(i) + ((1.111e-05*T_1(i)^3) + (-0.0004048*T_1(i)^2) + (1.746*T_1(i)) - 202.4);
   s_1(i) = ((-4.9e-07*T_1(i)) - 0.00011)*P_1(i) + ((-2.952e-06*T_1(i)^2) + (0.005814*T_1(i)) - 0.6077);
   rho_1(i) = ((((-1.017e-08)*T_1(i)^2) + (3.735e-07*T_1(i)) - (4.348e-05))*P_1(i)^2) + ((((3.105e-06)*T_1(i)^2) + ((0.0002845)*T_1(i)) + 0.07088)*P_1(i)) + (((-0.0004762)*T_1(i)^2) - (0.9038*T_1(i)) + 885.1);
%%
   %%3 pre-feed pump exit
   P_3(i) = P_5(i) - ((rho_1(i)*(pi^2)*(D_5^2)*(N_5(i)^2)*psi_5)/100000);
   h_3s(i) = (-0.0003106*P_3(i)^2 + 0.006695*P_3(i) - 1.735)*s_1(i)^4 + (-0.0003447*P_3(i)^2 + 0.01245*P_3(i) + 4.172)*s_1(i)^3 + (-0.0002273*P_3(i)^2 + 0.01789*P_3(i) + 95.73)*s_1(i)^2 + (-0.001136*P_3(i)^2 + 0.04523*P_3(i) + 383.7)*s_1(i) + (-2.108e-05*P_3(i)^2 + 0.1285*P_3(i) - 0.1304);
   %Extra calculations for system parameters
   deltaP_3(i) = (P_3(i)-P_1(i));
   H_3(i) = (deltaP_3(i)*100000)/(rho_1(i)*g); %head in meters
   V_3(i) = ((((-0.00936*exp(-0.0069*N_3)) + ((-0.0001897)*exp(-0.002966*N_3)))*H_3(i)^3) + (((0.0158*exp(-0.004869*N_3)) + (0.001029*exp(-0.001683*N_3)))*H_3(i)^2) + (((-0.55*exp(-0.00238*N_3)) + (-0.178*exp(-0.0003959*N_3)))*H_3(i)) + ((0.009919*N_3) + (-0.001277)))/3600; %vol flow rate in m3/s
   m_1(i) = V_3(i)*rho_1(i);
   Pow_3(i) = (0.001884*(V_3(i)*3600)^3) + (((-2.45e-05*N_3) + (1.17e-06))*(V_3(i)*3600)^2) + (((-5.918e-08*N_3^2) + (-9.25e-09*N_3)+ 7.336e-07)*(V_3(i)*3600)) + ((7.846e-06*N_3^2) + (-0.01139*N_3) + 5.333); %shaft power of pre-feed pump
   %
   h_3(i) = h_1(i)+(Pow_3(i)/m_1(i));
   %h_3(i) = h_1(i)+(sqrt((Pow_3(i)/m_1(i))*(h_3s(i)-h_1(i))));OLD
   %h_3(i) = ((h_3s(i) - h_1(i))/eff_3)+h_1(i);%Simulating pump fault
   T_3(i) = (-1.515e-09*P_3(i)^2 + 1.021e-07*P_3(i) - 0.0002849)*h_3(i)^2 + (2.652e-06*P_3(i)^2 + 8.356e-05*P_3(i) + 0.4949)*h_3(i) + (-0.0007576*P_3(i)^2 - 0.02197*P_3(i) + 110.5);
   s_3(i) = (6.09e-12*T_3(i)^2 - 5.262e-12*T_3(i) + 4.163e-08)*P_3(i)^2 + (-2.476e-09*T_3(i)^2 - 1.681e-07*T_3(i) - 0.0001203)*P_3(i) + (-2.952e-06*T_3(i)^2 + 0.005814*T_3(i) - 0.6077);
   rho_3(i) = (((-8.11e-09*T_3(i)^2) + (1.385e-07*T_3(i)) - 3.622e-05)*P_3(i)^2) + (((1.333e-08*T_3(i)^3) + (4.81e-07*T_3(i)^2)+ (0.0004532*T_3(i)) + 0.06732)*P_3(i)) + ((-2.222e-05*T_3(i)^3) + (0.003857*T_3(i)^2)+ (-1.182*T_3(i)) + 890.9);
   PF_pump_eff(i) = (h_3s(i) - h_1(i))/(h_3(i) - h_1(i));

%%
   %%Main mass flow calculation (From Nozzle)
   G_noz = 1.09; %Gamma(cp/cv)
   P_crt(i) = P_7(i)*((2/(G_noz+1))^(G_noz/(G_noz-1))); %critical pressure
   T_crt(i) = T_7(i)*(2/(G_noz+1)); %Critical Temperature
   rho_crt(i) = (-1.288e-09*P_crt(i)^4 + 5.937e-08*P_crt(i)^3 - 1.012e-06*P_crt(i)^2 + 6.994e-06*P_crt(i) - 1.659e-05)*T_crt(i)^3 + (1.28e-06*P_crt(i)^4 - 5.887e-05*P_crt(i)^3 + 0.001003*P_crt(i)^2 - 0.00693*P_crt(i) + 0.01644)*T_crt(i)^2 + (-0.0004242*P_crt(i)^4 + 0.01945*P_crt(i)^3 - 0.3316*P_crt(i)^2 + 2.285*P_crt(i) - 5.43)*T_crt(i) + (0.04682*P_crt(i)^4 - 2.138*P_crt(i)^3 + 36.49*P_crt(i)^2 - 248.4*P_crt(i) + 596.6)+(0.001067*P_crt(i)^3 + 0.01*P_crt(i)^2 + 0.1033*P_crt(i) - 0.52); %critical density
   c_crt(i) = (-5.59e-08*P_crt(i)^4 + 2.435e-06*P_crt(i)^3 - 4.237e-05*P_crt(i)^2 + 0.0002169*P_crt(i) - 0.0007415)*T_crt(i)^2 + (3.699e-05*P_crt(i)^4 - 0.001604*P_crt(i)^3 + 0.02826*P_crt(i)^2 - 0.1372*P_crt(i) + 0.678)*T_crt(i) + (-0.006168*P_crt(i)^4 + 0.2671*P_crt(i)^3 - 4.786*P_crt(i)^2 + 20.4*P_crt(i) + 93.9); %critical speed of sound
   m_2(i) = rho_crt(i)*A*c_crt(i);
 %%
   %%5 main pump exit
   h_5s(i) = (((4.392*sin(0.05246*P_5(i)+3.43)) + (2.754*sin(0.06772*P_5(i)+6.18)))*s_3(i)^4) + (((-5.762e-05*P_5(i)^2) + (0.01099*P_5(i)) + 4.157)*s_3(i)^3) + (((-5.714e-05*P_5(i)^2) + (0.01786*P_5(i)) + 95.72)*s_3(i)^2) + (((2.222e-05*P_5(i)^3) + (-0.00181*P_5(i)^2) + (0.07706*P_5(i)) + 383.4)*s_3(i)) + ((-9.524e-06*P_5(i)^2) + (0.1284*P_5(i)) + (-0.1313));
   FC(i) = m_2(i)/(rho_3(i)*((pi*(d_5^2))/4)*2*pi*N_5(i)*D_5);%ratio of discharge throat velocity to impeller tip speed (vel = massflow/density*area)
   eff_5(i) = ((-0.4827*FC(i)^2) + (0.5111*FC(i)) - 0.003077)/((FC(i)^4) + (-2.328*FC(i)^3) + (1.914*FC(i)^2) + (-1.199*FC(i)) + 0.7444);
   h_5(i) = ((h_5s(i) - h_3(i))/eff_5(i))+h_3(i);
   T_5(i) = (1.193e-10*P_5(i) + 1.982e-07)*h_5(i)^3 + (6.286e-08*P_5(i) - 0.0002328)*h_5(i)^2 + (9.452e-05*P_5(i) + 0.4994)*h_5(i) + (-0.03357*P_5(i) + 110.7);
```

```
    rho_5(i) = (((-6.643e-09)*P_5(i)^2) + ((3.238e-06)*P_5(i)) - 0.0005393)*T_5(i)^2 + (((1.905e-07)*P_5(i)^2) + ((0.0002543)*P_5(i)) - 0.8933)*T_5(i) + (((6.237e-16)*P_5(i)^2) + ((0.07048)*P_5(i)) + 884.7);
    cp_5(i) = (((3.524e-13)*P_5(i)^2 + (-8.562e-11)*P_5(i) + (-1.095e-08))*T_5(i)^3) + (((-2.476e-11)*P_5(i)^2 + (2.681e-09)*P_5(i) + (5.564e-06))*T_5(i)^2) + (((2.381e-09)*P_5(i)^2 + (-1.298e-06)*P_5(i) + 0.002944)*T_5(i)) + 1.623;
    %T5Eng(i) = T_5(i);
%%
    %%7 evaporator exit
    h_7(i) = (-2.845e-07*P_7(i)^4 + 2.715e-05*P_7(i)^3 - 0.0009716*P_7(i)^2 + 0.01498*P_7(i) - 0.08302)*T_7(i)^2 + (0.0001952*P_7(i)^4 - 0.01857*P_7(i)^3 + 0.6636*P_7(i)^2 - 10.21*P_7(i) + 58.72)*T_7(i) + (-0.03354*P_7(i)^4 + 3.183*P_7(i)^3 - 113.5*P_7(i)^2 + 1742*P_7(i) - 9601)-((0.002593*P_7(i)^3) + (0.01825*P_7(i)^2) + (-0.2989*P_7(i)) + 6.905);
    s_7(i) = (-1.928e-10*P_7(i)^4 + 1.846e-08*P_7(i)^3 - 6.729e-07*P_7(i)^2 + 1.045e-05*P_7(i) - 6.069e-05)*T_7(i)^2 + (1.315e-07*P_7(i)^4 - 1.253e-05*P_7(i)^3 + 0.0004555*P_7(i)^2 - 0.00705*P_7(i) + 0.04441)*T_7(i) + (-2.249e-05*P_7(i)^4 + 0.002129*P_7(i)^3 - 0.07706*P_7(i)^2 + 1.179*P_7(i) - 6.411)+((1.852e-06*P_7(i)^3) + (-7.063e-05*P_7(i)^2) + (0.001593*P_7(i)) - 0.009048);
    rho_7(i) = (((8.366e-05*exp(0.1511*P_7(i))) + (1.164e-10*exp(0.4674*P_7(i))))*T_7(i)^2) + (((-0.0539*exp(0.1561*P_7(i))) + (-4.009e-17*exp(0.9954*P_7(i))))*T_7(i)) + ((13.8*exp(0.1468*P_7(i))) + (1.032e-14*exp(0.9877*P_7(i))))+((7.702*sin(0.4607*P_7(i)+0.3832)) + (4.895*sin(0.2124*P_7(i)+2.78)));
%%
    %%8 turbine exit
    P_8(i) = P_1(i) + Pdrop_c + Pdrop_Rh;
    h_8s(i) = (1.571*P_8(i) + 2.692)*s_7(i)^3 + (-3.571*P_8(i)^2 - 2.214*P_8(i) + 121.3)*s_7(i)^2 + (275*P_8(i)^3 - 419.6*P_8(i)^2 + 266.4*P_8(i) + 69.62)*s_7(i) + (89.63*P_8(i)^3 - 140.1*P_8(i)^2 + 87.81*P_8(i) + 84.51);
    h_8(i) = h_7(i) - ((PtG(i)+(m_1(i)*(h_5(i)-h_3(i)))+5)/(0.8*m_2(i)));
    T_8(i) = ((-0.01*P_8(i)^2 - 0.017*P_8(i) + 0.3628)*h_8(i)^2 + (-583.3*P_8(i)^5 + 1000*P_8(i)^4 - 620.8*P_8(i)^3 + 200*P_8(i)^2 + 47.27*P_8(i) + 223.5)*h_8(i) + (6.667e+04*P_8(i)^5 - 1.125e+05*P_8(i)^4 + 6.75e+04*P_8(i)^3 - 2.238e+04*P_8(i)^2 - 8532*P_8(i) - 6.919e+04)) / (h_8(i) + (333.3*P_8(i)^5 - 541.7*P_8(i)^4 + 341.7*P_8(i)^3 - 64.58*P_8(i)^2 + 105.5*P_8(i) + 183.8));
    cp_8(i) = (((-2.527e-09)*P_8(i)^2 + (-5.138e-09)*P_8(i) + (-1.169e-09))*T_8(i)^3) + (((1.61e-06)*P_8(i)^2 + (3.8e-06)*P_8(i) + (-2.184e-06))*T_8(i)^2) + (((-0.0003589)*P_8(i)^2 + (-0.001018)*P_8(i) + 0.004238)*T_8(i)) + ((0.01852)*P_8(i)^3 + (0.005556)*P_8(i)^2 + (0.1161)*P_8(i) + 1.015);
    rho_8(i) = (((-2.495e-08*P_8(i)^2) + (-2.669e-08*P_8(i)) - 1.438e-10)*T_8(i)^3) + (((1.755e-05*P_8(i)^2) + (2.649e-05*P_8(i)) + 8.82e-08)*T_8(i)^2) + (((-0.004443*P_8(i)^2) + (-0.01232*P_8(i)) - 1.9e-05)*T_8(i)) + ((0.4377*P_8(i)^2) + (3.956*P_8(i)) + 0.00187);
    eff_8(i) = (h_7(i)-h_8(i))/(h_7(i)-h_8s(i));
    %T8Eng(i) = T_8(i);
%%
    %%Recuperator heat balance
    Q_max(i) = cp_8(i)*m_2(i)*((T_8(i)+273)-(T_5(i)+273));
    T_6(i) = ((T_5(i)+273)+(Recup_eff*Q_max(i)/(m_2(i)*cp_5(i))))-273;
    T_9(i) = ((T_8(i)+273)-(Recup_eff*Q_max(i)/(m_2(i)*cp_8(i))))-273;
    %T9Eng(i) = T_9(i);
 %%
    %%6 recuperator cold exit
    %P_6 = P_7 + Pdrop_E
    h_6(i) = (1.678e-10*P_6(i)^2 - 3.219e-08*P_6(i) + 2.029e-06)*T_6(i)^3 + (-5.452e-08*P_6(i)^2 + 9.451e-06*P_6(i) + 0.001189)*T_6(i)^2 + (7.619e-06*P_6(i)^2 - 0.001267*P_6(i) + 1.666)*T_6(i) + (-0.0003571*P_6(i)^2 + 0.1315*P_6(i) - 201.7);
    rho_6(i) = (((1.502e-07*P_6(i)) - 1.381e-05)*T_6(i)^3) + (((-7.677e-09*P_6(i)^3) + (1.454e-06*P_6(i)^2) + (-0.0001234*P_6(i)) + 0.005212)*T_6(i)^2) + (((1.071e-06*P_6(i)^3) + (-0.0002013*P_6(i)^2) + (0.01719*P_6(i)) - 1.614)*T_6(i)) + ((-3.636e-05*P_6(i)^3) + (0.007784*P_6(i)^2) + (-0.6337*P_6(i)) + 914.7);
%%
    %%9 recuperator hot exit
    P_9(i) = P_1(i) + Pdrop_c;
    h_9(i) = (7.919e-07*P_9(i) - 8.451e-07)*T_9(i)^3 + (-0.0004771*P_9(i) + 0.002133)*T_9(i)^2 + (3.472*P_9(i)^3 - 1.518*P_9(i)^2 + 0.3325*P_9(i) + 1.005)*T_9(i) + (463*P_9(i)^3 - 208.3*P_9(i)^2 + 18.03*P_9(i) + 226.9);
    rho_9(i) = (((-5.774e-08*P_9(i)) + 1.067e-09)*T_9(i)^3) + (((4.246e-05*P_9(i)) - 6.001e-07)*T_9(i)^2) + (((-0.006027*P_9(i)^2) + (-0.01342*P_9(i)) - 5.571e-06)*T_9(i)) + ((0.5*P_9(i)^2) + (4.015*P_9(i)) + 0.0005);
%%
    %%10 condenser exit
    P_10(i) = P_1(i);
    T_10(i) = T_1(i);
```

```
    h_10(i) = ((2.719e-09*T_10(i)^2) + (-8.269e-08*T_10(i)) + 9.318e-06)*P_10(i)^2 + ((-4.444e-09*T_10(i)^3) + (-1.714e-07*T_10(i)^2) + (-8.703e-05*T_10(i)) + 0.08099)*P_10(i) + ((1.111e-05*T_10(i)^3) + (-0.0004048*T_10(i)^2) + (1.746*T_10(i)) - 202.4);
%%
    %%Lubrication mass flow
    m_lub(i) = m_1(i) - m_2(i);
    %Work and heat balance
    Evap_heat(i) = m_2(i)*(h_7(i)-h_6(i));
    Turbine_work(i) = m_2(i)*(h_7(i)-h_8(i));
    cond_heat(i) = m_2(i)*(h_9(i)-h_10(i));
    MP_power(i) = m_1(i)*(h_5(i)-h_3(i));
    PFP_power(i) = m_1(i)*(h_3(i)-h_1(i));
%%
    %%System evaluation
    Heat_bal(i) = Evap_heat(i)-Turbine_work(i)-cond_heat(i)+MP_power(i)+PFP_power(i);%Energy balance not heat balance
    eta_therm(i) = (1 - (cond_heat(i)/Evap_heat(i)))*100;
    cyc_eff(i) = ((Turbine_work(i) - MP_power(i) - PFP_power(i))*100)/Evap_heat(i); %net cycle efficiency def as net work in divided by gross heat in

%%
    %%Sensor data analysis
    h1Eng(i) = ((2.719e-09*T1Eng(i)^2) + (-8.269e-08*T1Eng(i)) + 9.318e-06)*P1Eng(i)^2 + ((-4.444e-09*T1Eng(i)^3) + (-1.714e-07*T1Eng(i)^2) + (-8.703e-05*T1Eng(i)) + 0.08099)*P1Eng(i) + ((1.111e-05*T1Eng(i)^3) + (-0.0004048*T1Eng(i)^2) + (1.746*T1Eng(i)) - 202.4);
    s1Eng(i) = ((-4.9e-07*T1Eng(i)) - 0.00011)*P1Eng(i) + ((-2.952e-06*T1Eng(i)^2) + (0.005814*T1Eng(i)) - 0.6077);
    h3sEng(i) = (-0.0003106*P3Eng(i)^2 + 0.006695*P3Eng(i) - 1.735)*s1Eng(i)^4 + (-0.0003447*P3Eng(i)^2 + 0.01245*P3Eng(i) + 4.172)*s1Eng(i)^3 + (-0.0002273*P3Eng(i)^2 + 0.01789*P3Eng(i) + 95.73)*s1Eng(i)^2 + (-0.001136*P3Eng(i)^2 + 0.04523*P3Eng(i) + 383.7)*s1Eng(i) + (-2.108e-05*P3Eng(i)^2 + 0.1285*P3Eng(i) - 0.1304);
    %h3Eng(i) = (2.325e-09*T3Eng(i)^2 - 3.455e-08*T3Eng(i) + 7.634e-06)*P3Eng(i)^2 + (-3.333e-09*T3Eng(i)^3 - 4e-07*T3Eng(i)^2 - 7.167e-05*T3Eng(i) + 0.08065)*P3Eng(i) + (3.333e-06*T3Eng(i)^3 + 0.0011*T3Eng(i)^2 + 1.651*T3Eng(i) - 200.4);
    %%
    %%Mass flows
    rho1Eng(i) = ((((-1.017e-08)*T1Eng(i)^2) + (3.735e-07*T1Eng(i)) - (4.348e-05))*P1Eng(i)^2) + ((((3.105e-06)*T1Eng(i)^2) + ((0.0002845)*T1Eng(i)) + 0.07088)*P1Eng(i)) + (((-0.0004762)*T1Eng(i)^2) - (0.9038*T1Eng(i)) + 885.1);
    deltaP3Eng(i) = (P3Eng(i)-P1Eng(i));
    H3Eng(i) = (deltaP3Eng(i)*100000)/(rho1Eng(i)*g); %head in meters
    V3Eng(i) = ((((-0.00936*exp(-0.0069*N_3)) + ((-0.0001897)*exp(-0.002966*N_3)))*H3Eng(i)^3) + (((0.0158*exp(-0.004869*N_3)) + (0.001029*exp(-0.001683*N_3)))*H3Eng(i)^2) + (((-0.55*exp(-0.00238*N_3)) + (-0.178*exp(-0.0003959*N_3)))*H3Eng(i)) + ((0.009919*N_3) + (-0.001277)))/3600; %vol flow rate in m3/s
    m1Eng(i) = V3Eng(i)*rho1Eng(i);
    %
    G_nozEng = 1.09; %Gamma(cp/cv)
    PcrtEng(i) = P7Eng(i)*((2/(G_nozEng+1))^(G_nozEng/(G_nozEng-1))); %critical pressure
    TcrtEng(i) = T7Eng(i)*(2/(G_nozEng+1)); %Critical Temperature
    rhocrtEng(i) = (-1.288e-09*PcrtEng(i)^4 + 5.937e-08*PcrtEng(i)^3 - 1.012e-06*PcrtEng(i)^2 + 6.994e-06*PcrtEng(i) - 1.659e-05)*TcrtEng(i)^3 + (1.28e-06*PcrtEng(i)^4 - 5.887e-05*PcrtEng(i)^3 + 0.001003*PcrtEng(i)^2 - 0.00693*PcrtEng(i) + 0.01644)*TcrtEng(i)^2 + (-0.0004242*PcrtEng(i)^4 + 0.01945*PcrtEng(i)^3 - 0.3316*PcrtEng(i)^2 + 2.285*PcrtEng(i) - 5.43)*TcrtEng(i) + (0.04682*PcrtEng(i)^4 - 2.138*PcrtEng(i)^3 + 36.49*PcrtEng(i)^2 - 248.4*PcrtEng(i) + 596.6)+(0.001067*PcrtEng(i)^3 + 0.01*PcrtEng(i)^2 + 0.1033*PcrtEng(i) - 0.52); %critical density
    ccrtEng(i) = (-5.59e-08*PcrtEng(i)^4 + 2.435e-06*PcrtEng(i)^3 - 4.237e-05*PcrtEng(i)^2 + 0.0002169*PcrtEng(i) - 0.0007415)*TcrtEng(i)^2 + (3.699e-05*PcrtEng(i)^4 - 0.001604*PcrtEng(i)^3 + 0.02826*PcrtEng(i)^2 - 0.1372*PcrtEng(i) + 0.678)*TcrtEng(i) + (-0.006168*PcrtEng(i)^4 + 0.2671*PcrtEng(i)^3 - 4.786*PcrtEng(i)^2 + 20.4*PcrtEng(i) + 93.9); %critical speed of sound
    m2Eng(i) = rhocrtEng(i)*A*ccrtEng(i);
    %
    mlubEng(i) = m1Eng(i)-m2Eng(i);
    %
    Pow3Eng(i) = (0.001884*(V3Eng(i)*3600)^3) + (((-2.45e-05*N_3) + (1.17e-06))*(V3Eng(i)*3600)^2) + (((-5.918e-08*N_3^2) + (-9.25e-09*N_3)+ 7.336e-07)*(V3Eng(i)*3600)) + ((7.846e-06*N_3^2) + (-0.01139*N_3) + 5.333); %shaft power of pre-feed pump
    h3Eng(i) = h1Eng(i)+(Pow3Eng(i)/m1Eng(i));
```

```
    T3Eng(i) = (-1.515e-09*P3Eng(i)^2 + 1.021e-07*P3Eng(i) - 0.0002849)*h3Eng(i)^2 + (2.652e-06*P3Eng(i)^2 + 8.356e-05*P3Eng(i) + 0.4949)*h3Eng(i) + (-0.0007576*P3Eng(i)^2 - 0.02197*P3Eng(i) + 110.5);
    %%
    s3Eng(i) = (6.09e-12*T3Eng(i)^2 - 5.262e-12*T3Eng(i) + 4.163e-08)*P3Eng(i)^2 + (-2.476e-09*T3Eng(i)^2 - 1.681e-07*T3Eng(i) - 0.0001203)*P3Eng(i) + (-2.952e-06*T3Eng(i)^2 + 0.005814*T3Eng(i) - 0.6077);
    h5sEng(i) = (((4.392*sin(0.05246*P5Eng(i)+3.43)) + (2.754*sin(0.06772*P5Eng(i)+6.18)))*s3Eng(i)^4) + (((-5.762e-05*P5Eng(i)^2) + (0.01099*P5Eng(i)) + 4.157)*s3Eng(i)^3) + (((-5.714e-05*P5Eng(i)^2) + (0.01786*P5Eng(i)) + 95.72)*s3Eng(i)^2) + (((2.222e-05*P5Eng(i)^3) + (-0.00181*P5Eng(i)^2) + (0.07706*P5Eng(i)) + 383.4)*s3Eng(i)) + ((-9.524e-06*P5Eng(i)^2) + (0.1284*P5Eng(i)) + (-0.1313));
    h5Eng(i) = (-3.729e-09*P5Eng(i) + 1.128e-06)*T5Eng(i)^3 + (-1.714e-07*P5Eng(i) + 0.001542)*T5Eng(i)^2 + (-8.333e-05*P5Eng(i) + 1.621)*T5Eng(i) + (0.08*P5Eng(i) - 199.7);
    s7Eng(i) = (-1.928e-10*P7Eng(i)^4 + 1.846e-08*P7Eng(i)^3 - 6.729e-07*P7Eng(i)^2 + 1.045e-05*P7Eng(i) - 6.069e-05)*T7Eng(i)^2 + (1.315e-07*P7Eng(i)^4 - 1.253e-05*P7Eng(i)^3 + 0.0004555*P7Eng(i)^2 - 0.00705*P7Eng(i) + 0.04441)*T7Eng(i) + (-2.249e-05*P7Eng(i)^4 + 0.002129*P7Eng(i)^3 - 0.07706*P7Eng(i)^2 + 1.179*P7Eng(i) - 6.411)+((1.852e-06*P7Eng(i)^3) + (-7.063e-05*P7Eng(i)^2) + (0.001593*P7Eng(i)) - 0.009048);
    h7Eng(i) = (-2.845e-07*P7Eng(i)^4 + 2.715e-05*P7Eng(i)^3 - 0.0009716*P7Eng(i)^2 + 0.01498*P7Eng(i) - 0.08302)*T7Eng(i)^2 + (0.0001952*P7Eng(i)^4 - 0.01857*P7Eng(i)^3 + 0.6636*P7Eng(i)^2 - 10.21*P7Eng(i) + 58.72)*T7Eng(i) + (-0.03354*P7Eng(i)^4 + 3.183*P7Eng(i)^3 - 113.5*P7Eng(i)^2 + 1742*P7Eng(i) - 9601)-((0.002593*P7Eng(i)^3) + (0.01825*P7Eng(i)^2) + (-0.2989*P7Eng(i)) + 6.905);
    h8sEng(i) = (1.571*P8Eng(i) + 2.692)*s7Eng(i)^3 + (-3.571*P8Eng(i)^2 - 2.214*P8Eng(i) + 121.3)*s7Eng(i)^2 + (275*P8Eng(i)^3 - 419.6*P8Eng(i)^2 + 266.4*P8Eng(i) + 69.62)*s7Eng(i) + (89.63*P8Eng(i)^3 - 140.1*P8Eng(i)^2 + 87.81*P8Eng(i) + 84.51);
    h8Eng(i) = (4.225e-07*P8Eng(i) - 9.441e-07)*T8Eng(i)^3 + (-5e-05*P8Eng(i)^2 - 0.000285*P8Eng(i) + 0.002174)*T8Eng(i)^2 + (0.025*P8Eng(i)^2 + 0.07479*P8Eng(i) + 1.011)*T8Eng(i) + (-1.852*P8Eng(i)^3 + 1.23*P8Eng(i)^2 - 11.86*P8Eng(i) + 228.8);
%%
    %%PERFORANCE PARAMETERS
    %%Pre-feed pump
    PFPetaEng(i) = (h3sEng(i)-h1Eng(i))/(h3Eng(i)-h1Eng(i));
    PFPPREng(i) = P3Eng(i)/P1Eng(i);
    PFPPR(i) = P_3(i)/P_1(i);
    %%Main pump
    MPetaEng(i) = (h5sEng(i)-h3Eng(i))/(h5Eng(i)-h3Eng(i));
    MPeta(i) = (h_5s(i)-h_3(i))/(h_5(i)-h_3(i));
    MPPREng(i) = P5Eng(i)/P3Eng(i);
    MPPR(i) = P_5(i)/P_3(i);
    %%Turbine
    TetaEng(i) = (h7Eng(i)-h8Eng(i))/(h7Eng(i)-h8sEng(i));
    Teta(i) = eff_8(i);
    TPREng(i) = P8Eng(i)/P7Eng(i);
    TPR(i) = P_8(i)/P_7(i);
    %%Recuperator
    REffecEng(i) = (T8Eng(i)-T9Eng(i))/(T8Eng(i)-T5Eng(i));
    REffec(i) = (T_8(i)-T_9(i))/(T_8(i)-T_5(i));
    RHsPREng(i) = P9Eng(i)/P8Eng(i);
    RHsPR(i) = P_9(i)/P_8(i);
    %%Evaporator
    EPREng(i) = P7Eng(i)/P5Eng(i);
    EPR(i) = P_7(i)/P_5(i);
    EEffecEng(i) = (TFIEng(i)-TFOEng(i))/(TFIEng(i)-T6Eng(i));
    EEffec(i) = (TFI(i)-TFO(i))/(TFI(i)-T_6(i));
    %%Condenser
    CPREng(i) = P1Eng(i)/P9Eng(i);
    CPR(i) = P_1(i)/P_9(i);
    CEffecEng(i) = (T9Eng(i)-T1Eng(i))/(T9Eng(i)-TCIEng(i));
    CEffec(i) = (T_9(i)-T_1(i))/(T_9(i)-TCI(i));

    %%Deviation INDEX
    D_PR_pfp(i) = (PFPPREng(i) - PFPPR(i))*100/PFPPR(i);
    D_eta_pfp(i) = (PFPetaEng(i)- PF_pump_eff(i))*100/PF_pump_eff(i);
    D_V3(i) = (V3Eng(i)-V_3(i))*100/V_3(i);
    D_eta_mp(i) = (MPetaEng(i) - MPeta(i))*100/MPeta(i);
    D_PR_mp(i) = (MPPREng(i) - MPPR(i))*100/MPPR(i);
```

```
    D_eta_T(i) = (TetaEng(i) - Teta(i))*100/Teta(i);
    D_PR_T(i) = (TPREng(i) - TPR(i))*100/TPR(i);
    D_eff_R(i) = (REffecEng(i) - REffec(i))*100/REffec(i);
    D_PR_R(i) = (RHsPREng(i) - RHsPR(i))*100/RHsPR(i);
    D_PR_E(i) = (EPREng(i) - EPR(i))*100/EPR(i);
    D_Effec_E(i) = (EEffecEng(i) - EEffec(i))*100/EEffec(i);
    D_PR_C(i) = (CPREng(i) - CPR(i))*100/CPR(i);
    D_eff_C(i) = (CEffecEng(i) - CEffec(i))*100/CEffec(i);

end

figure(1)
subplot(2,1,1)
plot(1:length(Teta), Teta)
hold on
plot(1:length(TetaEng),TetaEng)
legend('Model','Active Engine')
xlabel('t [s]')
ylabel('\eta_8 [-]')
title('Transient behaviour of Turbine isentropic efficiency')
subplot(2,1,2)
plot(1:length(TPR),TPR)
hold on
plot(1:length(TPREng), TPREng)
legend('Model','Active Engine')
xlabel('t [s]')
ylabel('PR_8 [-]')
title('Transient behaviour of Turbine Pressure ratio')

figure(2)
subplot(2,1,1)
plot(1:length(MPeta), MPeta)
hold on
plot(1:length(MPetaEng),MPetaEng)
legend('Model','Active Engine')
xlabel('t [s]')
ylabel('\eta_5 [-]')
title('Transient behaviour of Main pump isentropic efficiency')
subplot(2,1,2)
plot(1:length(MPPR), MPPR)
hold on
plot(1:length(MPPREng),MPPREng)
legend('Model','Active Engine')
xlabel('t [s]')
ylabel('PR_5 [-]')
title('Transient behaviour of Main pump Pressure ratio')

figure(3)
subplot(2,1,1)
plot(1:length(PF_pump_eff), PF_pump_eff)
hold on
plot(1:length(PFPetaEng),PFPetaEng)
legend('Model','Active Engine')
xlabel('t [s]')
ylabel('\eta_3 [-]')
title('Transient behaviour of Pre-feed pump isentropic efficiency')
subplot(2,1,2)
plot(1:length(PFPPR), PFPPR)
hold on
plot(1:length(PFPPREng),PFPPREng)
legend('Model','Active Engine')
xlabel('t [s]')
```

```
ylabel('PR_3 [-]')
title('Transient behaviour of Pre-feed pump Pressure ratio')

figure(4)
subplot(3,1,1)
plot(1:length(m_1), m_1)
hold on
plot(1:length(m1Eng),m1Eng)
legend('Model','Active Engine')
xlabel('t [s]')
ylabel('m_1 [kgs^{-1}]')
title('Transient behaviour of total mass flow')
subplot(3,1,2)
plot(1:length(m_2), m_2)
hold on
plot(1:length(m2Eng),m2Eng)
legend('Model','Active Engine')
xlabel('t [s]')
ylabel('m_2 [kgs^{-1}]')
title('Transient behaviour of main mass flow')
subplot(3,1,3)
plot(1:length(m_lub), m_lub)
hold on
plot(1:length(mlubEng),mlubEng)
legend('Model','Active Engine')
xlabel('t [s]')
ylabel('m_{lub} [kgs^{-1}]')
title('Transient behaviour of lubrication mass flow')

figure(5)
subplot(2,1,1)
plot(1:length(REffec), REffec)
hold on
plot(1:length(REffecEng),REffecEng)
legend('Model','Active Engine')
xlabel('t [s]')
ylabel('\epsilon_R [-]')
title('Transient behaviour of Recuperator effectiveness')
subplot(2,1,2)
plot(1:length(RHsPR),RHsPR)
hold on
plot(1:length(RHsPREng), RHsPREng)
legend('Model','Active Engine')
xlabel('t [s]')
ylabel('PR_9 [-]')
title('Transient behaviour of Recuperator(Hot) Pressure ratio')

figure(6)
subplot(2,1,1)
plot(1:length(EEffec), EEffec)
hold on
plot(1:length(EEffecEng),EEffecEng)
legend('Model','Active Engine')
xlabel('t [s]')
ylabel('\epsilon_E [-]')
title('Transient behaviour of Evaporator effectiveness')
subplot(2,1,2)
plot(1:length(EPR),EPR)
hold on
plot(1:length(EPREng), EPREng)
legend('Model','Active Engine')
xlabel('t [s]')
```

```
ylabel('PR_7 [-]')
title('Transient behaviour of Evaporator Pressure ratio')

figure(7)
subplot(2,1,1)
plot(1:length(CEffec), CEffec)
hold on
plot(1:length(CEffecEng),CEffecEng)
legend('Model','Active Engine')
xlabel('t [s]')
ylabel('\epsilon_C [-]')
title('Transient behaviour of Condenser effectiveness')
subplot(2,1,2)
plot(1:length(CPR),CPR)
hold on
plot(1:length(CPREng), CPREng)
legend('Model','Active Engine')
xlabel('t [s]')
ylabel('PR_{10} [-]')
title('Transient behaviour of Condenser Pressure ratio')

figure(8)
indices = [D_PR_pfp(end) D_eta_pfp(end) D_V3(end) D_eta_mp(end) D_PR_mp(end) D_eta_T(end) D_PR_T(end)
D_eff_R(end) D_PR_R(end) D_PR_E(end) D_Effec_E(end) D_PR_C(end) D_eff_C(end)];
bar(indices)
set(gca, 'XTickLabel',
{'\DeltaPR_3','\Delta\eta_3','\Delta\eta_{V3}','\Delta\eta_5','\DeltaPR_5','\Delta\eta_8','\DeltaPR_8','\Delta\epsilon_9','\DeltaPR_
9','\DeltaPR_7','\Delta\epsilon_7','\DeltaPR_{10}','\Delta\epsilon_{10}'});
ylabel('%\Delta')
title('Component health indices')

%%
%Thermophysical properties
figure(9)
%subplot(2,1,1)
plot(1:length(P_3),P_3)
hold on
plot(1:length(P3Eng),P3Eng)
legend('Model','Active Engine')
xlabel('t [s]')
ylabel('P_3 [bar]')
title('Transient behaviour of Pre-feed pump exit pressure')
%subplot(2,1,2)
% plot(1:length(Pow_3),Pow_3)
% hold on
% plot(1:length(Pow3Eng),Pow3Eng)
% legend('Model','Active Engine')
% xlabel('t [s]')
% ylabel('P [KW]')
% title('Transient behaviour of Pre-feed pump power')

figure(10)
plot(1:length(P_5),P_5)
hold on
plot(1:length(P5Eng),P5Eng)
legend('Model','Active Engine')
xlabel('t [s]')
ylabel('P_5 [bar]')
title('Transient behaviour of Main pump exit pressure')

figure(11)
plot(1:length(P_8),P_8)
```

```
hold on
plot(1:length(P8Eng),P8Eng)
legend('Model','Active Engine')
xlabel('t [s]')
ylabel('P_8 [bar]')
title('Transient behaviour of Turbine exit pressure')

figure(12)
plot(1:length(P_9),P_9)
hold on
plot(1:length(P9Eng),P9Eng)
legend('Model','Active Engine')
xlabel('t [s]')
ylabel('P_9 [bar]')
title('Transient behaviour of Rhs exit pressure')

figure(13)
plot(1:length(T_5),T_5)
hold on
plot(1:length(T5Eng),T5Eng)
legend('Model','Active Engine')
xlabel('t [s]')
ylabel('T_5 [^{\circ}C]')
title('Transient behaviour of Main pump exit temperature')

figure(14)
plot(1:length(T_6),T_6)
hold on
plot(1:length(T6Eng),T6Eng)
legend('Model','Active Engine')
xlabel('t [s]')
ylabel('T_6 [^{\circ}C]')
title('Transient behaviour of Rcs exit temperature')

figure(15)
plot(1:length(T_8),T_8)
hold on
plot(1:length(T8Eng),T8Eng)
legend('Model','Active Engine')
xlabel('t [s]')
ylabel('T_8 [^{\circ}C]')
title('Transient behaviour of Turbine exit temperature')

figure(16)
plot(1:length(T_9),T_9)
hold on
plot(1:length(T9Eng),T9Eng)
legend('Model','Active Engine')
xlabel('t [s]')
ylabel('T_9 [^{\circ}C]')
title('Transient behaviour of Rhs exit temperature')

figure(17)
plot(1:length(REffec),REffec)
hold on
plot(1:length(REffecEng),REffecEng)
legend('Model','Active Engine')
xlabel('t [s]')
ylabel('\epsilon_R [-]')
title('Transient behaviour of Recuperator effectiveness')

toc
```